

The Effect of Solving the Energy Equation on Combustion Simulation using Automatically Generated Chemical Reactor Networks

Master Thesis Project

M.D. de Wit

Technische Universiteit Delft

THE EFFECT OF SOLVING THE ENERGY EQUATION ON COMBUSTION SIMULATION USING AUTOMATICALLY GENERATED CHEMICAL REACTOR NETWORKS

MASTER THESIS PROJECT

by

M.D. de Wit

in partial fulfillment of the requirements for the degree of

Master of Science
in Aerospace Engineering

at the Delft University of Technology
to be defended publicly on 28 Nov 2019

Supervisors: Dr. A. Gangoli Rao
A.A.V. Perpignan MSc
R. Sampat MSc
Thesis committee: Dr. A. Gangoli Rao
Dr. D.J.E.M Roekaerts
Dr. B.V.S Jyoti
A.A.V. Perpignan MSc

An electronic version of this thesis is available at <http://repository.tudelft.nl/>

ABSTRACT

In the field of combustion systems, methods and tools are under development to fulfill the need for fast and accurate prediction of emissions such as NO and CO. CFD-CRN is a hybrid approach that utilizes a combination of computational fluid dynamics (CFD) and a chemical reactor network (CRN) to simulate the flow field and chemical kinetics of a combustion system in detail. This thesis describes the research into the effect of applying the energy equation to update the temperature whilst solving the CRN. The objective is to quantify the effect of the common assumption that the temperature generated by CFD is sufficiently accurate and can be kept fixed to reduce the non-linearity of the system of equations to be solved in the CRN.

This research uses and modifies the computational tool AGNES, that was developed at the Delft University of Technology and is able to automatically cluster, solve and visualise the results of a CRN based on results from CFD. The test cases used are the Sandia Flame D, which is a piloted methane-air jet flame with a Reynolds number of 22400 [1], and the Verissimo et al. test case, which is a flameless combustion burner [2]. The CRN was clustered with the zones and tolerances set by Monaghan et al. [3]. The results were validated using experimental data of temperature and species mass fractions and the sensitivity of the clustering method was studied.

The results of CFD-CRN simulations were used to evaluate the effect of updating the temperature using the energy equation. The results show that solving the energy equation leads to a progressive overprediction of temperature in the far field of the computational domain, which consequently results in the overprediction of NO and CO concentrations. A potential cause for the overprediction is identified as the heat transfer in the form of conduction and radiation not being accounted for in the solving of the CRN. Unless the diffusion of heat is accurately modeled, the application of the energy equation is not recommended.

PREFACE

This thesis forms the conclusion of my career as a university student. Although I never intend to stop learning new things in my future career, this feels like the close of an important chapter in my life.

Presenting my thesis research in this form makes me really proud and I hope that at some point it will be of use to another student interested in this subject.

With this work, I would like to shed some light on the extremely vast field of combustion simulation and provide my take on it.

During my thesis project, I learned that a research topic and approach don't have to be overly complicated to be useful and that simple topics and approaches can still be quite challenging.

In the end, this result would not have been here without the help of my two daily supervisors, André A.V. Perignan and Rishikesh Sampat. Therefore, I would like to thank them in this preface, although they definitely deserve more acknowledgement. Furthermore, I would like to thank Dr. Arvind G. Rao for introducing me to this subject and providing me with critical questions and insights that kept me sharp.

Aside from my supervisors, I would like to acknowledge Romano van Genderen, who was willing to sacrifice his time to help with my simulations and Jacob van Hengst for his patience in listening to my endless ramblings.

It took me nine months to get to this thesis you are reading now and if I did my job right, you should be able to read what you are looking for in significantly less time.

*M.D. de Wit
Delft, November 2019*

CONTENTS

Abstract	iii
Preface	v
List of Figures	ix
List of Tables	xv
Nomenclature	xvii
1 Introduction	1
1.1 Background	1
1.2 Developments in CFD-CRN	4
1.3 Research Possibilities in AGNES	8
1.4 Temperature Prediction in CFD-CRN	12
1.5 Research Outline	14
2 Theory	15
2.1 Combustion Thermodynamics	15
2.2 Chemical Kinetics	15
2.3 Reaction Mechanisms	17
2.4 Transport Processes	17
2.5 Turbulent Transport and Modeling	19
2.6 Chemical Source Term Modeling	21
2.7 Flameless Combustion	22
3 Method	25
3.1 Research Question Resolvment	25
3.2 General Research Approach	26
3.3 Simulation Test Case	26
3.4 CFD Method and Set-up	29
3.5 CRN Method and Set-up	29
3.6 Result Visualisation	31
3.7 Simulation Time Reduction	32
3.8 Global Solver Energy Conservation	33
4 Results and Discussion	37
4.1 Turbulent Diffusion Modeling	37
4.2 Zoning Method Sensitivity and Effects	39
4.3 Grid Independence Study SFD	50
4.4 Comparison CFD and CRN	53
4.5 Effect of Energy Equation	60
4.6 CRN Solving Time	67
5 Conclusion	69
5.1 Research Conclusions	69
5.2 Method and Test Case Concluding Remarks	70

6 Recommendations	71
6.1 Recommended Improvements of AGNES	71
6.2 User Recommendations for AGNES.	72
6.3 Suggested Research with AGNES	72
Bibliography	75
A CFD Set-up	79
B CRN Set-up	83
C Changelog AGNES	85

LIST OF FIGURES

1.1	Timescales in turbulent reacting flow [4].	2
1.2	AGNES algorithm	9
1.3	Timescales in turbulent reacting flows [4].	10
2.1	Relationship between enthalpies of formation and reaction. Based on Winterbone [5]	15
2.2	Reaction flow analysis of stoichiometric premixed Methane-air flame at atmospheric condition. Based on Warnatz [4].	17
2.3	Schematic representation of the energy cascade of eddies in turbulent flow.	19
2.4	Schematic representation of the DNS, LES and RANS modeling and resolvment ranges of eddies in turbulent flow.	20
2.5	Schematic representation of local temperature time evolution computed with DNS, RANS and LES.	20
2.6	Improved combustion regime diagram proposed by Rao and Levy [6]	22
3.1	Close-up of the SFD pilot.	26
3.2	Sandia Flame dimensions [7].	27
3.3	Inlet and combustion chamber dimensions of the Verissimo et al. test case [2].	28
3.4	Surface integration method comparison	32
3.5	Jacobian sample structure accounting for reactor inter-connectivity (J_s) with nr as the number of reactors and i as the amount of variables to be solved for each reactor.	34
3.6	Jacobian sample structure accounting for reactions within the reactors (J_w) with nr as the number of reactors and i as the amount of variables to be solved for each reactor.	34
4.1	Experimental (●), CFD PVI $C\epsilon_1 = 1.53$ (●) and CFD-CRN predicted profiles (left) and volume integral averages (right) of Mass fraction of CO₂ in the radial direction at axial location D75 ($x/d_{jet} = 75$) for CRNs with 973 PSRs with static temperature clustering without (●) and with Peclet turbulent diffusion modeling (●).	37
4.2	Experimental (●), CFD PVI $C\epsilon_1 = 1.53$ (●) and CFD-CRN predicted profiles (left) and volume integral averages (right) of Mass fraction of CO in the radial direction at axial location D75 ($x/d_{jet} = 75$) for CRNs with 973 PSRs with static temperature clustering without (●) and with Peclet turbulent diffusion modeling (●).	38
4.3	Experimental (●), CFD PVI $C\epsilon_1 = 1.53$ (●) and CFD-CRN predicted profiles (left) and volume integral averages (right) of Mass fraction of NO in the radial direction at axial location D75 ($x/d_{jet} = 75$) for CRNs with 973 PSRs with static temperature clustering without (●) and with Peclet turbulent diffusion modeling (●).	38
4.4	Experimental (●), CFD PVI $C\epsilon_1 = 1.53$ (●) and CFD-CRN predicted profiles (left) and volume integral averages (right) of Mass fraction of CO in the radial direction at axial location D15 ($x/d_{jet} = 15$) for CRNs with 249 PSRs in the original Monaghan clustering (●) and 249 PSRs in Monaghan clustering with $\Delta f = 0.02K$ substituted for $\Delta f = 0.01$ (●).	40
4.5	Experimental (●), CFD PVI $C\epsilon_1 = 1.53$ (●) and CFD-CRN predicted profiles (left) and volume integral averages (right) of Static Temperature in the radial direction at axial location D45 ($x/d_{jet} = 45$) for CRNs with 249 PSRs in the original Monaghan clustering (●) and 252 PSRs in Monaghan clustering with $\Delta T = 16K$ substituted for $\Delta T = 2K$ (●).	41

- 4.6 Experimental (●), CFD PVI $C_{\epsilon_1} = 1.53$ (●) and CFD-CRN predicted profiles (left) and volume integral averages (right) of **Mass fraction of CH₄** in the radial direction at axial location **D45** ($x/d_{jet} = 45$) for CRNs with **249 PSRs** in the **original Monaghan clustering** (●) and **252 PSRs in Monaghan clustering with $\Delta T = 16K$ substituted for $\Delta T = 2K$** (●). 41
- 4.7 Experimental (●), CFD PVI $C_{\epsilon_1} = 1.53$ (●) and CFD-CRN predicted profiles (left) and volume integral averages (right) of **Mass fraction of CO** in the radial direction at axial location **D45** ($x/d_{jet} = 45$) for CRNs with **249 PSRs** in the **original Monaghan clustering** (●) and **252 PSRs in Monaghan clustering with $\Delta T = 16K$ substituted for $\Delta T = 2K$** (●). 42
- 4.8 Experimental (●), CFD PVI $C_{\epsilon_1} = 1.53$ (●) and CFD-CRN predicted profiles (left) and volume integral averages (right) of **Mass fraction of NO** in the radial direction at axial location **D75** ($x/d_{jet} = 75$) for CRNs with **249 PSRs** in the **original Monaghan clustering** (●) and **252 PSRs in Monaghan clustering with $\Delta T = 16K$ substituted for $\Delta T = 2K$** (●). 42
- 4.9 Experimental (●) and CFD-CRN predicted profiles of **Mass fraction of CO₂** at the centreline **DCL** ($r/d_{jet} = 0$) for CRNs with **249 PSRs** in the **original Monaghan clustering** (●), **251 PSRs in Monaghan clustering with $\Delta T = 16K$ substituted for $\Delta T = 2K$** (●) and **248 PSRs in Monaghan clustering with $\Delta T = 75K$ substituted for $\Delta T = 50K$** (●). 43
- 4.10 Experimental (●), CFD PVI $C_{\epsilon_1} = 1.53$ (●) and CFD-CRN predicted profiles (left) and volume integral averages (right) of **Mass fraction of CH₄** in the radial direction at axial location **D15** ($x/d_{jet} = 15$) for CRNs with **1559 PSRs** in the **original Monaghan clustering** (●), **5496 PSRs in Monaghan zoning with tolerance 0.06** (●) and **1581 PSRs in Temperature, Axial Coordinate and Mean Mixture Fraction clustering with tolerance 0.03** (●). 44
- 4.11 Experimental (●), CFD PVI $C_{\epsilon_1} = 1.53$ (●) and CFD-CRN predicted profiles (left) and volume integral averages (right) of **Mass fraction of H₂O** in the radial direction at axial location **D15** ($x/d_{jet} = 15$) for CRNs with **1559 PSRs** in the **original Monaghan clustering** (●), **5496 PSRs in Monaghan zoning with tolerance 0.06** (●) and **1581 PSRs in Temperature, Axial Coordinate and Mean Mixture Fraction clustering with tolerance 0.03** (●). 44
- 4.12 Experimental (●), CFD PVI $C_{\epsilon_1} = 1.53$ (●) and CFD-CRN predicted profiles (left) and volume integral averages (right) of **Mass fraction of CH₄** in the radial direction at axial location **D60** ($x/d_{jet} = 60$) for CRNs with **1559 PSRs** in the **original Monaghan clustering** (●), **5496 PSRs in Monaghan zoning with tolerance 0.06** (●) and **1581 PSRs in Temperature, Axial Coordinate and Mean Mixture Fraction clustering with tolerance 0.03** (●). 45
- 4.13 Experimental (●), CFD PVI $C_{\epsilon_1} = 1.53$ (●) and CFD-CRN predicted profiles (left) and volume integral averages (right) of **Mass fraction of H₂O** in the radial direction at axial location **D60** ($x/d_{jet} = 60$) for CRNs with **1559 PSRs** in the **original Monaghan clustering** (●), **5496 PSRs in Monaghan zoning with tolerance 0.06** (●) and **1581 PSRs in Temperature, Axial Coordinate and Mean Mixture Fraction clustering with tolerance 0.03** (●). 45
- 4.14 Experimental (●) and CFD-CRN predicted profiles of **Static Temperature** at the centreline **DCL** ($r/d_{jet} = 0$) for CRNs with **249 PSRs** in the **original Monaghan clustering** (●) and **249 PSRs in scaled tolerance clustering** (●). 46

4.15	Experimental (●), CFD PVI $C\epsilon_1 = 1.53$ (●) and CFD-CRN predicted profiles (left) and volume integral averages (right) of Mass fraction of CH₄ in the radial direction at axial location D45 ($x/d_{jet} = 45$) for CRNs with 249 PSRs in the original Monaghan clustering (●) and 249 PSRs in scaled tolerance clustering (●).	47
4.16	Experimental (●), CFD PVI $C\epsilon_1 = 1.53$ (●) and CFD-CRN predicted profiles (left) and volume integral averages (right) of Mass fraction of O₂ in the radial direction at axial location D60 ($x/d_{jet} = 60$) for CRNs with 249 PSRs in the original Monaghan clustering (●) and 249 PSRs in scaled tolerance clustering (●).	47
4.17	CFD-CRN predicted parallel contour of Static Temperature [K] for a CRN with 3137 PSRs in the constant tolerance clustering .	48
4.18	CFD-CRN predicted parallel contour of Static Temperature [K] for a CRN with 3210 PSRs in the Monaghan clustering .	48
4.19	Experimental (●), CFD (●) and CFD-CRN predicted profiles of Mass fraction of CO₂ in the radial direction at axial location 113 ($z = 113mm$) for CRNs with 3137 PSRs in the constant tolerance clustering (●) and 3210 PSRs in Monaghan clustering (●).	49
4.20	Experimental (●), CFD (●) and CFD-CRN predicted profiles of Mass fraction of CO in the radial direction at axial location 113 ($z = 113mm$) for CRNs with 3137 PSRs in the constant tolerance clustering (●) and 3210 PSRs in Monaghan clustering (●).	49
4.21	Experimental (●), CFD (●) and CFD-CRN predicted profiles of Mass fraction of CO in the radial direction at axial location 310 ($z = 310mm$) for CRNs with 3137 PSRs in the constant tolerance clustering (●) and 3210 PSRs in Monaghan clustering (●).	49
4.22	Experimental (●) and CFD-CRN predicted profiles of Mass fraction of NO_x in the radial direction at axial location 310 ($z = 310mm$) for CRNs with 3137 PSRs in the constant tolerance clustering (●) and 3210 PSRs in Monaghan clustering (●).	49
4.23	Experimental (●), CFD PVI $C\epsilon_1 = 1.53$ (●) and CFD-CRN predicted profiles (left) and volume integral averages (right) of Mass fraction of O₂ in the radial direction at axial location D75 ($x/d_{jet} = 75$) for CRNs with 249 (●), 493 (●) and 1035 (●) PSRs in the original Monaghan clustering .	50
4.24	Experimental (●), CFD PVI $C\epsilon_1 = 1.53$ (●) and CFD-CRN predicted profiles (left) and volume integral averages (right) of Mass fraction of CO in the radial direction at axial location D75 ($x/d_{jet} = 75$) for CRNs with 249 (●), 493 (●) and 1035 (●) PSRs in the original Monaghan clustering .	51
4.25	Experimental (●), CFD PVI $C\epsilon_1 = 1.53$ (●) and CFD-CRN predicted profiles (left) and volume integral averages (right) of Mass fraction of NO in the radial direction at axial location D75 ($x/d_{jet} = 75$) for CRNs with 249 (●), 493 (●) and 1035 (●) PSRs in the original Monaghan clustering .	51
4.26	Experimental (●), CFD PV2 $C\epsilon_1 = 1.60$ (●) and CFD-CRN predicted profiles (left) and volume integral averages (right) of Mass fraction of O₂ in the radial direction at axial location D75 ($x/d_{jet} = 75$) for CRNs with 249 (●), 493 (●) and 1035 (●) PSRs in the original Monaghan clustering .	52
4.27	Experimental (●), CFD PV2 $C\epsilon_1 = 1.60$ (●) and CFD-CRN predicted profiles (left) and volume integral averages (right) of Mass fraction of CO in the radial direction at axial location D75 ($x/d_{jet} = 75$) for CRNs with 249 (●), 493 (●) and 1035 (●) PSRs in the original Monaghan clustering .	52
4.28	Experimental (●), CFD PV2 $C\epsilon_1 = 1.60$ (●) and CFD-CRN predicted profiles (left) and volume integral averages (right) of Mass fraction of NO in the radial direction at axial location D75 ($x/d_{jet} = 75$) for CRNs with 249 (●), 493 (●) and 1035 (●) PSRs in the original Monaghan clustering .	53
4.29	CFD PV2 $C\epsilon_1 = 1.6$ predicted parallel contour of Static Temperature .	54

4.30	CFD-CRN predicted parallel contour of Static Temperature in for a CRN with 1006 PSRs in the Monaghan clustering based on CFD PV2 $C\epsilon_1 = 1.6$. (The white lines show the axial location of the radial experimental data.)	54
4.31	Experimental (●), CFD PVI $C\epsilon_1 = 1.53$ (●) and CFD-CRN predicted profiles (left) and volume integral averages (right) of Mass fraction of CH4 in the radial direction at axial location D15 ($x/d_{jet} = 15$) for a CRN with 1035 PSRs in the Monaghan clustering (●).	54
4.32	Experimental (●), CFD PVI $C\epsilon_1 = 1.53$ (●) and CFD-CRN predicted profiles (left) and volume integral averages (right) of Mass fraction of CH4 in the radial direction at axial location D60 ($x/d_{jet} = 60$) for a CRN with 1035 PSRs in the Monaghan clustering (●).	55
4.33	Experimental (●), CFD PV2 $C\epsilon_1 = 1.6$ (●) and CFD-CRN predicted profiles (left) and volume integral averages (right) of Mass fraction of CO in the radial direction at axial location D15 ($x/d_{jet} = 15$) for a CRN with 1006 PSRs in the Monaghan clustering (●).	56
4.34	Experimental (●), CFD PV2 $C\epsilon_1 = 1.6$ (●) and CFD-CRN predicted profiles (left) and volume integral averages (right) of Mass fraction of CO in the radial direction at axial location D60 ($x/d_{jet} = 60$) for a CRN with 1006 PSRs in the Monaghan clustering (●).	56
4.35	Experimental (●), CFD PVI $C\epsilon_1 = 1.53$ (●) and CFD-CRN predicted profiles (left) and volume integral averages (right) of Mass fraction of CH4 in the radial direction at axial location D30 ($x/d_{jet} = 30$) for a CRN with 1035 PSRs in the Monaghan clustering (●).	57
4.36	Experimental (●), CFD PVI $C\epsilon_1 = 1.53$ (●) and CFD-CRN predicted profiles (left) and volume integral averages (right) of Mass fraction of O2 in the radial direction at axial location D45 ($x/d_{jet} = 45$) for a CRN with 1035 PSRs in the Monaghan clustering (●).	57
4.37	CFD predicted parallel contour of Static Temperature [K]	58
4.38	CFD-CRN predicted parallel contour of Static Temperature [K] for a CRN with 3137 PSRs in the constant tolerance clustering	58
4.39	Experimental (●), CFD (●) and CFD-CRN predicted profiles of Static Temperature [K] in the radial direction at axial location 113 ($z = 113mm$) for CRNs with 3137 PSRs in the constant tolerance clustering (●) and 3210 PSRs in Monaghan clustering (●).	59
4.40	Experimental (●), CFD (●) and CFD-CRN predicted profiles of Mass fraction of O2 in the radial direction at axial location 133 ($z = 133mm$) for CRNs with 3137 PSRs in the constant tolerance clustering (●) and 3210 PSRs in Monaghan clustering (●).	59
4.41	Experimental (●), CFD (●) and CFD-CRN predicted profiles of Mass fraction of CO in the radial direction at axial location 310 ($z = 310mm$) for CRNs with 3137 PSRs in the constant tolerance clustering (●) and 3210 PSRs in Monaghan clustering (●).	59
4.42	Experimental (●), CFD (●) and CFD-CRN predicted profiles of Mass fraction of CO2 in the radial direction at axial location 310 ($z = 310mm$) for CRNs with 3137 PSRs in the constant tolerance clustering (●) and 3210 PSRs in Monaghan clustering (●).	59
4.43	Experimental (●), CFD PVI $C\epsilon_1 = 1.53$ (●) and CFD-CRN predicted profiles (left) and volume integral averages (right) of Static Temperature in the radial direction at axial location D03 ($x/d_{jet} = 3$) for CRNs with 1035 PSRs in the Monaghan clustering without (●) and with updating temperature (●).	60
4.44	Experimental (●) and CFD-CRN predicted profiles of Static Temperature at the centreline DCL ($r/d_{jet} = 0$) for CRNs with 1035 PSRs in the Monaghan clustering without (●) and with updating temperature (●).	61
4.45	CFD-CRN predicted parallel contour of Static Temperature [K] for a CRN with 1035 PSRs in the Monaghan clustering based on CFD PVI $C\epsilon_1 = 1.53$ using the energy equation .*	61
4.46	CFD-CRN predicted parallel contour of Static Temperature [K] for a CRN with 1035 PSRs in the Monaghan clustering based on CFD PVI $C\epsilon_1 = 1.53$ notusing the energy equation .*	61

4.47	CFD-CRN predicted parallel contour of Density for a CRN with 1035 PSRs in the Monaghan clustering based on CFD PV1 $C_{\epsilon_1} = 1.53$ using the energy equation .*	62
4.48	CFD-CRN predicted parallel contour of Density for a CRN with 1035 PSRs in the Monaghan clustering based on CFD PV1 $C_{\epsilon_1} = 1.53$ not using the energy equation .*	62
4.49	Experimental (●) and CFD-CRN predicted profiles of Mass fraction of NO at the centreline DCL ($r/d_{jet} = 0$) for CRNs with 1035 PSRs in the Monaghan clustering without (●) and with updating temperature (●).	63
4.50	Experimental (●), CFD PV2 $C_{\epsilon_1} = 1.6$ (●) and CFD-CRN predicted profiles (left) and volume integral averages (right) of Mass fraction of CO in the radial direction at axial location D02 ($x/d_{jet} = 2$) for CRNs with 1006 PSRs in the Monaghan clustering without (●) and with updating temperature (●).	63
4.51	Experimental (●), CFD PV2 $C_{\epsilon_1} = 1.6$ (●) and CFD-CRN predicted profiles (left) and volume integral averages (right) of Mass fraction of CO in the radial direction at axial location D75 ($x/d_{jet} = 75$) for CRNs with 1006 PSRs in the Monaghan clustering without (●) and with updating temperature (●).	64
4.52	Experimental (●) and CFD-CRN predicted profiles of Mass fraction of CH4 at the centreline DCL ($r/d_{jet} = 0$) for CRNs with 1035 PSRs in the Monaghan clustering without (●) and with updating temperature (●).	64
4.53	CFD PV2 $C_{\epsilon_1} = 1.6$ (CFD) and CFD-CRN predicted cross-sectional contours of Mass fraction of H2O at axial location D45 ($x/d_{jet} = 45$) for CRNs with 1006 PSRs in the Monaghan clustering without (1006 Mon) and with updating temperature (1006 Mon E).	65
4.54	CFD PV2 $C_{\epsilon_1} = 1.6$ (CFD) and CFD-CRN predicted cross-sectional contours of Mass fraction of H2O at axial location D75 ($x/d_{jet} = 75$) for CRNs with 1006 PSRs in the Monaghan clustering without (1006 Mon) and with updating temperature (1006 Mon E).	65
4.55	CFD-CRN predicted parallel contour of Static Temperature [K] for a CRN with 3137 PSRs in the constant tolerance clustering .	65
4.56	CFD-CRN predicted parallel contour of Static Temperature [K] for a CRN with 3137 PSRs in the constant tolerance clustering whilst updating the temperature .	65
4.57	CFD-CRN predicted parallel contour of Static Temperature [K] for a CRN with 3210 PSRs in the Monaghan clustering whilst updating the temperature .	66
4.58	Experimental (●), CFD (●) and CFD-CRN predicted profiles of Mass fraction of CO in the radial direction at axial location 310 ($z = 310mm$) for CRNs with 3137 PSRs in the constant tolerance clustering without (●) and with updating the temperature (●).	66
4.59	Experimental (●) and CFD-CRN predicted profiles of Mass fraction of NOx in the radial direction at axial location 310 ($z = 310mm$) for CRNs with 3137 PSRs in the constant tolerance clustering without (●) and with updating the temperature (●), and 3210 PSRs in Monaghan clustering with updating the temperature (●).	66
4.60	Experimental (●), CFD (●) and CFD-CRN predicted profiles of Mass fraction of CO2 in the radial direction at axial location 113 ($z = 113mm$) for CRNs with 3137 PSRs in the constant tolerance clustering without (●) and with updating the temperature (●).	67
4.61	Experimental (●), CFD (●) and CFD-CRN predicted profiles of Mass fraction of O2 in the radial direction at axial location 113 ($z = 113mm$) for CRNs with 3137 PSRs in the constant tolerance clustering without (●) and with updating the temperature (●).	67
4.62	CRN solving time. (CFD1: PV1 $C_{\epsilon_1} = 1.53$, CFD2: PV2 $C_{\epsilon_1} = 1.6$)	68

LIST OF TABLES

1.1	Overview of described developments in the field of CFD-CRN.	7
3.1	Bulk velocities of Sandia Flames C to F [7].	27
3.2	Test conditions of the Verissimo et al. test case that were utilised [2].	28
3.3	Axial and radial coordinates of experimental data measurement result Verissimo et al. test case.	31
3.4	Relative axial location and respective relative radial range of experimental results Sandia Flame D (d=0.0072)	31
4.1	Zone limits and reactor criteria as specified by Monaghan et al. [3].	39
4.2	Scaling tolerance ranges and function for each clustering criteria.	46
4.3	CRN solving times	68

NOMENCLATURE

ADEF	-	Approximate Deconvolution and Explicit Filtering
AGNES	-	Automatic Generation of Networks for Emission Simulation
BDF	-	Backward Differentiation Formula
BFS	-	Breadth First Search
CDC	-	Colourless Distributed Combustion
CFD	-	Computational Fluid Dynamics
CKM	-	Chemical Kinetic Mechanism
CMC	-	Conditional Moment Closure
CPU	-	Central Processing Unit
CRN	-	Chemical Reactor Network
Da	-	Damköhler number
Div.	-	Diversion
DNS	-	Direct Numerical Simulation
DO	-	Discrete Ordinates
EDC	-	Eddy Dissipation Concept
EXP	-	Experimental
FGM	-	Flamelet Generated Manifold
FLOX	-	Flameless Oxidation
HiCOT	-	High Temperature Combustion Technology
HiTAC	-	High Temperature Air Combustion
KPP	-	Kinetic Post-Processor
LES	-	Large Eddy Simulation
LIF	-	laser Induced Fluorescence
MILD	-	Moderate or Intense Low Oxygen Dilution
Mon	-	Monaghan
Man	-	Manuscript
PaSR	-	Partially Stirred Reactor
PCA	-	Principle Component Analysis
PDF	-	Probability Density Function
Pe	-	Peclet number
PFR	-	Plug-Flow Reactor
ppm	-	part per million
Pr	-	Prandtl number
PSR	-	Perfectly Stirred Reactor
px	-	pixels
RANS	-	Reynolds Average Navier Stokes
Re	-	Reynolds number
RSM	-	Reynolds Stress equation Model
S-A	-	Spalart-Allmaras
Sc	-	Schmidh number
SFD	-	Sandia Flame D
SFIRN	-	Simplified Fluid dynamics by Ideal Reactor Networks
SIMPLE	-	Semi-Implicit Method for Pressure-Linked Equations
SST	-	Shear Stress Transport
SUNDIALS	-	SUite of Non-linear Differential ALgebraic equations Solver
TDR	-	Turbulent Dissipation Rate
TKE	-	Turbulent Kinetic Energy
w.r.t.	-	with respect to

1. INTRODUCTION

The energy and transport sector are still largely dependent on combustion systems. To create a more sustainable environment and reduce global warming, the emissions from combustion systems have to be reduced.

The research topic described in this master thesis is related to emission prediction in combustion systems. The purpose of this master thesis is to show the procedure and insights from this research, which mainly focuses on the effect of using the energy equation to update the temperature in a automatically generated chemical reactor network, that is constructed from results obtained with computational fluid dynamics.

To explain this topic, Section 1.1 provides some background information on combustion systems, the issues inherent to the prediction of emissions and the main approaches for simulating the formation of emissions in a combustion system. In Section 1.2, the main developments in the most promising combustion simulation approach are presented. Section 1.3 describes the analysis of the field of CFD-CRN in relation to a computational tool, called AGNES, made by the Delft University of Technology, to determine, which scientific knowledge is still lacking and can be explored whilst improving AGNES to arrive at the current best-practices. The scientific gap with the highest priority is then further discussed in Section 1.4. Finally, the introduction is concluded with the outline of the research project that is the subject of this thesis.

1.1. BACKGROUND

Combustion systems are an energy dense power source that is an important generator of power in many industries [8]. Inherent to this type of power source is the production of emissions. In case of a combustion systems that uses hydrocarbon fuels, carbon dioxide (CO_2) and water (H_2O) are produced. These two species together with nitrogen (N_2) and oxygen (O_2) form the major species present in the product of the combustion. However, there are far more species present in the combustion product. These minor species are present in significantly smaller quantities than the major species mentioned, but are known to be harmful to human health and the environment. Examples of minor species are nitrogen oxides (NO_x) and carbon monoxide (CO). To reduce the harmful effect of these minor species on the environment and human health, legislation was put into place that limits the mass percentage of specific pollutants inside the emissions. These regulations have become stricter by lowering the allowable percentage and are expected to become more stringent in the future [9] [10]. This has sparked the need for fast and accurate prediction of both the major and minor species to ensure the combustion system will meet the target set by legislation [11][12][10].

Accurate prediction of the major and minor species in the emissions requires detailed solving for both the flow and the chemical kinetics present in the combustion system. This will cause the system of equations to be very large. The problem with this is that the chemical time scales for different reactions within combustion can vary between nanoseconds and seconds. This broad range of time scales is much broader than that of the flow timescales, as can be seen in Figure 1.1. This causes the large system of equations to become stiff, because small time steps are necessary to solve the fast reactions and a long total duration is necessary to solve the slow reactions.

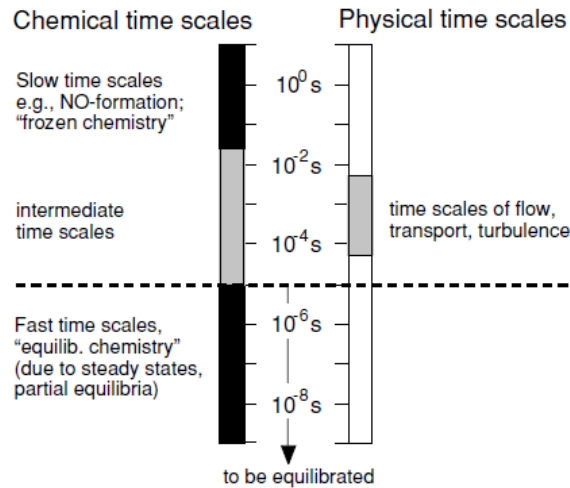


Figure 1.1: Timescales in turbulent reacting flow [4].

The amount of CPU power that is required to simultaneously model the flow and chemical kinetics in detail is currently still too high for computers to handle due to the stiffness of the system [10][13][11][12]. This has led to three main approaches to simulate the formation of emissions in a combustion system that were all described by Yousefian et al. [10].

The first approach is correlation-based modeling and uses measurement data of existing combustion systems to arrive at a prediction for the emissions of the combustion system being designed. The empirical data from ideally multiple very similar combustion systems are compared and based on the differences between the combustion systems and their emission data, estimations are made for the new combustion system. Examples of this type of prediction tool are the models made by Lipfert (1972) [14], Hung (1975) [15] and Touchton (1984) [16], that used correlations to estimate NO_x emissions of gas turbines.

The second approach is high-fidelity physics-based. This approach is limited in detail by the amount of CPU power, as mentioned before. This means that part of the model has to be simplified. This simplification can be exerted either on the level of detail of the simulation of the flow or on that of the chemical kinetics of the combustion system. It is often chosen to prioritize one over the other, which means that one is modeled in great detail, while the other is simplified till the CPU power required is acceptable. Most often the focus is placed on the detailed modeling of the flow and thus a reduced chemical kinetic mechanism is used to make the CPU power required manageable. This chemical kinetic mechanism reduction consists of reducing the number of species taken into account and can also entail the exclusive use of elementary reactions and the assumption of fast-chemistry. These simplifications reduce the stiffness and size of the system of equations. Examples of high-fidelity physics-based tools with computational fluid dynamics (CFD) are described by Fuller and Smith (1993) [17], Lai (1997) [18] and Crocker et al. (1999) [19], who all used a chemical model inside CFD to estimate temperature profiles, wall liner temperatures, flame patterns and other flow conditions inside a combustion chamber.

In the other option, the flow is simplified and a detailed kinetic mechanism is employed. The simplification of the flow can be achieved in multiple ways. The computational grid can be made coarser, which means that larger parts of the flow field are represented by one computational cell. This means that the chemical kinetics has to be solved for fewer points, which reduces the CPU power required although the system remains stiff. This type of approach is not used in industry, since the

simplified flow results are not very accurate and are not deemed suitable to be used to estimate other quantities of importance. It is also possible to decrease the level at which turbulence is solved for in the flow by e.g. using RANS instead of LES or only solving for larger scales in LES. Furthermore, a chemical reactor network (CRN) can be constructed manually based on CFD data without using the actual grid data.

The last approach is the hybrid approach. This approach splits the flow and chemistry of the combustion system. The first step of this approach is to model the flow field. The flow is modeled by either using computational fluid dynamics (CFD) or by component modeling from experimental data and uses highly simplified chemistry with only a few species. The results obtained from the first step contain many computational cells, which would cause the CPU power to become too high if a detailed kinetic mechanism (DKM) was applied. Therefore, as a next step in the hybrid-approach, the computational cells are clustered based on similarities. Common criteria for this clustering are temperature, local stoichiometry and velocity vectors, but any results from the flow simulation can be used as clustering criteria [20][10]. For these clustering criteria, intervals are set that determine whether neighbouring computational cells can be clustered together [20]. This clustering can be done manually or using an automatic clustering algorithm. After the clusters are formed, each cluster is modeled as a type of reactor. This reactor can be perfectly stirred (PSR), plug-flow (PFR) or partially stirred (PaSR). This network of reactors is then solved for using a detailed kinetic model to determine the emissions of the combustion system [10].

All three main approaches have their strengths and weaknesses regarding computational speed and prediction accuracy [10]. Because it is just a matter of changing input variables, the correlation based prediction is relatively fast, once the correlations have been established. However, these correlations can only be applied to cases that are close to the original experimental data set from which they were derived. If the new combustion system is not similar enough to this data set, the predictions of the correlation based tool will not be valid. This limitation is so strict that for the same combustion system with different operating conditions the predictions from a correlation based tool might already diverge too much from the actual results to be helpful.

The high-fidelity physics-based approach can be applied to any combustion system. The problem, however, is that the necessary simplifications to arrive at an allowable CPU power lower the accuracy of the emission prediction. In case the kinetic model is simplified, species that are not included in the reduced model will cause over-prediction of other species. Furthermore assumptions like fast-chemistry are not valid for e.g. the reaction rates in NO_x, which leads to flaws in the prediction [20]. If on the other hand the flow model is simplified, a lot of the smaller fluctuations in, for instance, the temperature of the flow are lost, which will affect the kinetic model results and make them differ from empirical results. Although the available CPU power is increasing continuously, which allows for more detail in the simplified model, it is still a problem [10].

The hybrid approach provides detail in the simulation of both the flow and the chemical kinetics because they are split into two separate parts [10]. This split creates a slight decrease in accuracy as it is assumed that the flow is not affected by changes in the minor species concentrations, which are not captured by the reduced kinetic model used when the flow is modeled. However, because the concentrations of minor species are relatively low with respect to the major species which are modeled, this assumption does not decrease the accuracy more than the simplifications applied in high-fidelity physics-based approach [13][11][21]. This makes the hybrid approach currently the most promising approach for accurate emission prediction for combustion systems.

Researchers at the Delft University of Technology are working on a computational tool for predicting emissions in combustion systems according to the hybrid approach. The tool is called Automatic Generation of Networks for Emission Simulation (AGNES) and automatically clusters and solves a chemical reactor network (CRN) based on results from CFD to obtain a prediction of the emissions of the combustion system. AGNES is under development and might still be improved.

1.2. DEVELOPMENTS IN CFD-CRN

As explained in Section 1.1, the CFD-CRN method is defined as a hybrid method that splits the detailed solving of the flow field and the chemistry in a combustion system. As the name suggests the flow field is solved with the use of computational fluid dynamics and the chemistry is solved with a chemical reactor network, which is based on the results from CFD [10]. The CRN mainly increases the accuracy of the prediction of minor species present in the emissions of the combustion system. The major species predictions are already modeled in the CFD computation, because these species significantly influence the flow field. To reduce the required CPU power for including a detailed kinetic model, it is assumed that the effect of the minor species on the flow is not significant, which allows for the split in the hybrid method [13][11][21][10].

The first account of the use of a CRN in the post-processing of CFD results was by Erhardt et al. (1998) [22]. Erhardt et al. focused mainly on the prediction of NO_x. In their work, the proposed method was demonstrated on a simple 2D geometry by creating a simplified network of PFR from a CFD analysis with $k-\epsilon$ turbulence model. Their zone model found a fairly good result for NO_x emissions with relatively few reactors [10]. However, the method was not applicable for more complex geometries, flows with recycling zones or any upstream diffusion that is not much smaller than the downstream convection [10][12].

Faravelli et al. (2001) [11] build on this method with the Simplified Fluid dynamics by Ideal Reactor Networks (SFIRN). SFIRN was used to determine NO_x emissions from the furnace of utility boilers. SFIRN was an improvement with respect to the Erhardt et al. method regarding the application to more complex kinetic schemes, the modeling of re-circulation and the inclusion of liquid fuels [10][12]. It was shown by Faravelli et al., that although of simplifications made, the tool provided practical results that were useful in furnace design [10].

In 2002, Falcitelli et al. [23] suggested the use of a general algorithm to construct CRNs. This algorithm consisted of six steps. Step 1: Compute flow field properties, like temperature and major species concentrations, with CFD on a fine mesh. Also determine local stoichiometry possibly with a post-processing tool. Step 2: Cluster the cells into homogeneous zones defined by intervals of temperature and stoichiometry, that will be represented by an ideal reactor. Step 3: Determine the operating parameters for each reactor by adding the volumes and computing the temperature with an enthalpy conservation expression. Step 4: Assign a PSR or PFR based on the velocity vector distribution in the respective cluster. Step 5: Compute mass exchange between reactors by adding mass flows between cell faces forming the cluster boundaries. Step 6: Carry out kinetic computation on CRN with a detailed kinetic model for species present in the combustion. Using this algorithm Falcitelli et al. showed that with a limited amount of reactors (400) a very good agreement could be found with experimental data for industrial applications [10].

The algorithm proposed by Falcitelli et al. was used by Mancini (2007) [24] on flameless combustion. Falcitelli et al. later adjusted this algorithm by clustering the cells based on unmixedness as the temperature and stoichiometry clustering yielded a too large number of zones with the set intervals [10].

Skjoth-Rasmussen et al. (2004) [25] stepped away from the clustering and modeled all the cells in the computational domain as PaSR. In their work, each cell was split in a reactive and inert part to account for turbulent fluctuations and grid resolutions between 1500 and 30000 were tried [10][12][25].

In 2005, Frassoldati et al. [26] used a similar approach as Falcitelli to predict NO_x production. As clustering criteria temperature and composition were used to generate the clusters that were all assigned a PSR with operating conditions as defined by the SFIRN method from Faravelli et al. Frassoldati et al. analysed the minimum number of reactors required to precisely predict the NO_x emissions.

Novoselov and Malte (2006) [27] used a slightly different approach following the eight step method of the University of Washington to arrive at the CRN to predict NO_x and CO emissions with the GRI-Mech 3.0 chemical kinetic mechanism.

Using the kinetic post-processor (KPP), Cuoci et al. (2007) [28] modeled turbulent combustion in diffusion flames. To account for the effect that turbulent fluctuations have on the temperature, the kinetic equivalent temperature was introduced by Cuoci et al. This kinetic equivalent temperature was based on the temperature variance as found by the CFD computation. Furthermore, improvements were made regarding the convergence by alterations made to the numerical procedure, which reduced the computational time required to reach the solution.

Fichet et al. (2010) [29] using a similar technique payed great attention to the splitting criteria to ensure a minimal amount of reactors to predict NO_x emissions. This clustering was based on the temperature, mixture fraction and normalized progress variable as well as the streamlines and fluid age. Moreover, Fichet et al. did not keep the temperature for each reactor fixed based on the CFD results. Most researchers have assumed that the influence of the minor species on temperature is so minimal due to their small quantities and low heat release, that it can be neglected [13][11][21][10]. In the work of Fichet et al. this assumption was not made, because it was argued that for the prediction of NO_x minor temperature changes are important and therefore the energy equation had to be solved to determine the temperature in each reactor [29].

To study NO_x and the pathways of formation of NO_x, Monaghan et al. (2012) [3] divided the Sandia D diffusion flame [1] into multiple zones based on temperature, mixture fraction and axial position. For each zone appropriate criteria were selected to generate the clusters, which were each modeled by a PSR. The results were successfully validated.

In 2013, Cuoci et al. [12] developed a method that allowed for the handling of very large networks and showed that turbulent fluctuations have a large impact on the prediction accuracy. Furthermore, Cuoci et al. suggested to further investigate the use of different clustering criteria to arrive at a minimum number of reactors with the most accurate results. Moreover, it was suggested to work on parallelization of the solving process of the network to reduce the computational time.

This is exactly what Stagni et al. [21] did in 2013 by developing KPPSMOKE as an improvement on the KPP method. This fully coupled and parallelized code increased the flexibility and allowed the solving of very large networks, due to the distribution of CPU-power over multiple processors at the same time. KPPSMOKE was compared to the Ansys Fluent NO_x processor and the Fluent unsteady flamelet model and was found to be closer to the experimental results in both cases. Monaghan et al. [30] used KPPSMOKE to predict CO and NO_x emissions and study the pollutant pathways.

To study different approaches for clustering, Nilsson (2014) [31] developed a tool for CRN construction. Two approaches were analysed with the Sandia Flame D: principal component analysis (PCA) based and cluster growth based [31]. Both methods constructed a mesh by dividing the computational domain into zones that comply with the selected criteria intervals. It was found that the cluster growth method required less reactors to comply with the given criteria, as the PCA based method generated a larger number of small zones due to its procedure.

Finally, in 2018, Sampat [20] developed AGNES to investigate the choice of clustering criteria as was suggested by Cuoci et al in 2013 [12]. The exact current set up of AGNES will be further discussed in Section 1.3. It is the aim of the Delft University of Technology to further improve AGNES by making sure that it is up to date with the latest developments within CFD-CRN as described in this section and performing further research in the field of CFD-CRN.

An overview of the developments described in this section is provided in Table 1.1. It was found by analyzing the developments within CFD-CRN, that although there are some outliers most researchers have approached CFD-CRN in a similar way. Flow field properties are computed with CFD and often some post-processing is applied to determine certain quantities that have a pronounced influence on the production of the species at the focus of the respective research.

Usually, the computational domain is then simplified by grouping grid cells based on their resemblance regarding the selected clustering criteria. Temperature was used the most as a clustering criteria and was often combined with the local stoichiometry. However, depending on the test case and the emission under research another combination of clustering criteria might yield a lower number of reactors required, whilst maintaining the accuracy of the prediction [12][20]. Furthermore, the method of cluster growth for constructing the network was recently found by Nilsson [31] to achieve a network with fewer reactors for the same intervals.

Operating conditions for the different clusters are obtained in similar fashion and each cluster is assigned a reactor. In the beginning of CFD-CRN, researchers used a combination of PSR, PFR and PaSR. This was possible, due to the test cases used and the number of reactors. More recently, most researchers have used only PSR, because the use of a single reactor type is less straining in terms of CPU in larger networks and was found to still achieve the required accuracy.

There are still some differences in how the turbulent fluctuations, the numerical procedure and reactor temperature are addressed to solve the CRN and there is still some unclarity on what is the best approach in these cases.

Author	Species	Research goal	Clustering method	Reactors	Test case
Erhardt et al. (1998)	NOx	Reduction of NOx due to reburning	Manual, subdivision based on streamlines and some axial coordinates	1 000 PFR	Natural gas
Faravelli et al. (2001)	NOx	NOx formation in industrial boilers	SFIRN: manual zoning, clustering based on temperature and stoichiometry, PFR or PSR based on flow characteristics	7 PSR, 6 PFR	Industrial boiler
Falcitelli et al. (2002)	O2, CO, H2, CO2 and H2O	General algorithm for minor species prediction	Temperature and stoichiometry intervals and geometrical connection based	400 PSR + PFR	Opposite wall fired steam generator
Skjoth-Rasmussen et al. (2004)	CO	General method for combining CFD and detailed kinetic mechanism	Each cell is separate reactor	15,500 PaSR	Laboratory swirl burner (Harwell furnace)
Frassoldati et al. (2005)	NOx	NOx emission in strong swirling confined flames	SFIRN	0-300 PSR + PFR	High swirled confined natural gas diffusion flames
Novoselov and Malte (2006)	NOx and CO	Predicting exhaust gas with CFD-CRN	University of Washington eight-step global method	31 PSR + PFR	Dry low emissions (DLE) industrial gas turbine combustor
Cuoci et al. (2007)	NOx	Prediction of flame structures and NOx formation in syngas burners	KPP: automatic, temperature, composition and dynamic fields based, aimed at specific number of reactors	8000 PSR	Syngas turbulent jet flames
Fichet et al. (2010)	NOx	Prediction of NOx emission in gas turbine	Automatic, equivalence ratio and temperature and streamlines based, mathematical algorithm	236 PSR	Gas turbine flame tube with natural gas
Monaghan et al. (2012)	NOx	Study of NOx formation pathways	KPP	1 114 PSR	Methane diffusion flame (Sandia Flame D)
Cuoci et al. (2013)	NOx	Prediction of NOx formation in turbulent flames	KPP	200-15000 PSR	Three turbulent jet flames
Stagni et al. (2013)	H2O, CO2, CO, CH2O, OH, O, NO and HCN	Code for emission prediction in turbulent combustion	KPPSMOKE: coupled and parallelized KPP	2360 PSR	Lab-scale burner and combustor for aircrafts
Nilsson (2014)	NOx	Emission simulation method for gas turbines	Cluster growth and PCA method: automatic, temperature and mixture fraction based	148 PSR	Sandia Flame D and gas turbine rig
Sampat (2018)	NOx, HCN, O2, CO and N2O	Effect of clustering criteria on emission prediction	AGNES: automatic (see Section 1.3)	1000, 5000 PSR	Flameless regime combustor

Table 1.1: Overview of described developments in the field of CFD-CRN.

1.3. RESEARCH POSSIBILITIES IN AGNES

As mentioned before, the Automatic Generation of Networks for Emission Simulation tool (AGNES) is a computational tool that was developed at the Delft University of Technology by Sampat in 2018. AGNES can be used to automatically construct and solve a CRN from CFD results of a combustion system and thereby generate emission predictions according to the hybrid CFD-CRN method. The initial purpose of AGNES was to support Sampat in his research regarding the choice of clustering criteria in CFD-CRN. Currently, AGNES can be used by the Delft University of Technology for further investigation into the field of CFD-CRN, but AGNES is not optimal yet and based on the developments in the field there are some improvements possible. Therefore the Delft University of Technology wants to further improve AGNES till it is up to date with the latest developments and use it to perform further research in the field of CFD-CRN.

AGNES was written in Python with the use of the CRN-solver Cantera and a detailed kinetic mechanism [20]. The choice for Python was based on the fact that it is a relatively easy, robust, flexible, open source programming language that is currently increasingly more used in industry. Cantera, as CRN-solver, is also open source and was chosen for its flexibility, compatibility with many programming languages including Python and because of its reliable chemistry bookkeeping layer [20]. The detailed kinetic mechanism can be any kinetic mechanism available. The GRI-Mech 3.0 kinetic mechanism is the kinetic mechanism used most often in industry and was used by Sampat [20]. More detailed kinetic mechanisms for natural gas combustion exist, but due to the lower solution time, robustness and stability inherent to a kinetic mechanism of the size of GRI-Mech 3.0, it is likely still preferred [10].

AGNES consists of several python files that have to be run consecutively to, respectively, construct the CRN, solve the system and visualize the results. Figure 1.2 shows the algorithm of AGNES in the form of a flow diagram. The first files of AGNES, represented by the 'Output processor'-box in Figure 1.2, are aimed at processing the output from the CFD computation of the combustion system test case. This processing consists of making a graph, that represents the computational cells and their inter-linkage, out of the different grid points and connecting those to the results, which is necessary for the clustering procedure. The graphs created by this part are only specific to the CFD results and can be re-used for different cluster set ups.

The next part of AGNES generates the clusters, as shown in Figure 1.2. AGNES was built to investigate the effect of clustering criteria on the emission prediction by CFD-CRN [20]. Therefore AGNES allows the use of any of the outputs of the CFD computation of the combustion system to be used as clustering criteria [20]. The clustering procedure makes use of a tolerance, which is applied to all the clustering criteria. Following the Breadth-First Search algorithm [32] the clusters are formed by performing a fitness check for each cell. This fitness check establishes whether the chosen criteria are within the tolerance and whether the cell is connected to the cluster. Based on the fitness check cells are added to the cluster or a new cluster is started until all cells have been evaluated from the queue. Finally, it is checked whether the number of reactors is below the specified number. Otherwise the tolerance is increased.

Next the operating conditions are determined in the 'OC computer'-box (Figure 1.2). Quantities like the cell volumes and species mass are added, quantities such as pressure are mass averaged and the total temperature and specific heat at constant pressure are averaged by keeping the total enthalpy constant [20]. The mass flows entering and leaving at the boundaries of the clusters are also determined and added. There is, however, a mass balance correction required due to the accumulation of errors present in the CFD results [20]. This correction entails determining the relative quantities

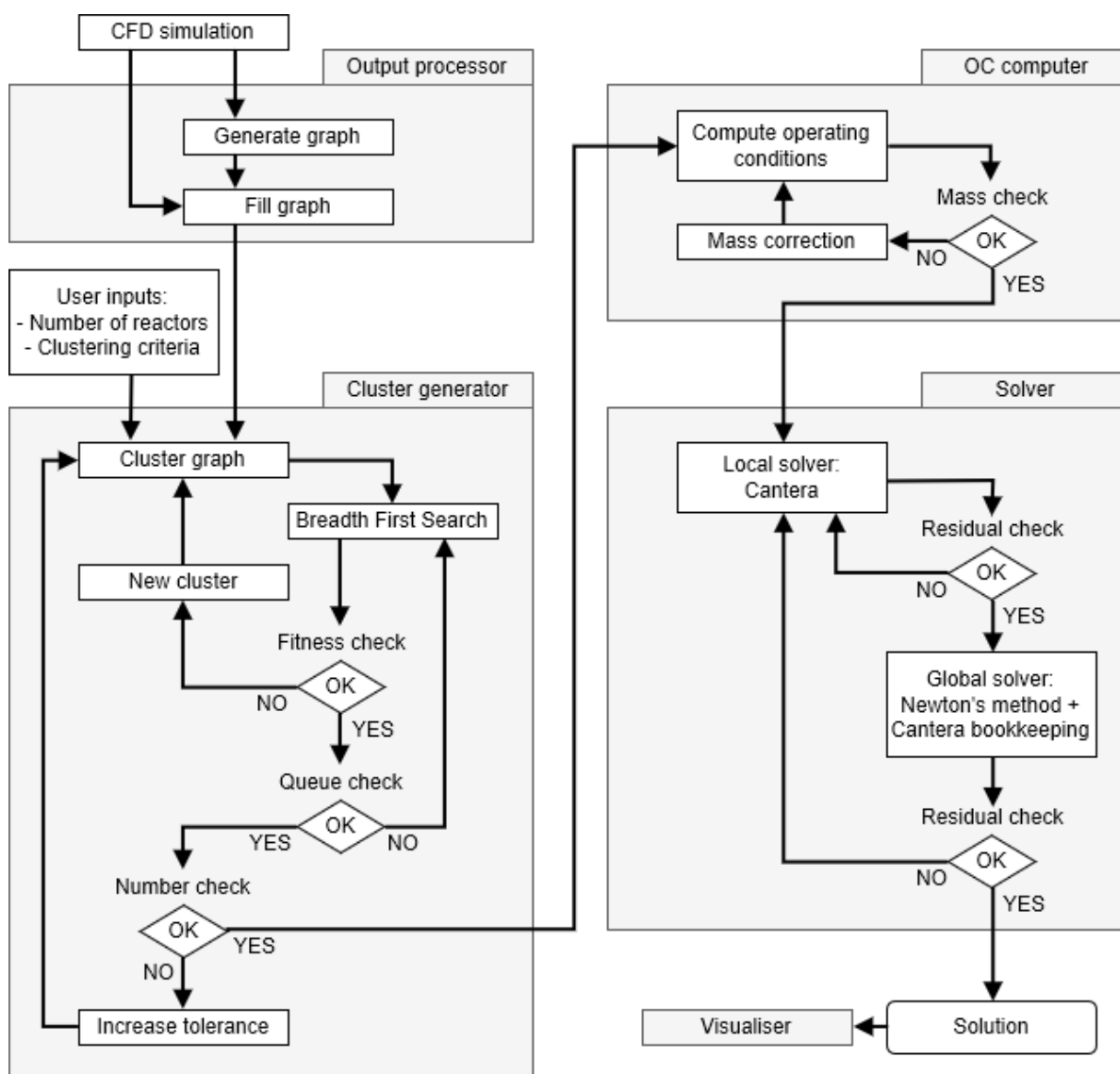


Figure 1.2: AGNES algorithm

of mass leaving to the adjacent clusters and then solving for those with the total inflow supplied [20]. In the pre-research version of AGNES, the temperature was kept fixed to the value computed by CFD under the assumption mentioned before that the influence of the minor species on the temperature is not significant. The option to use the energy equation to redetermine the temperature was partially present.

With the operating conditions set for the created clusters, the non-linear stiff system of ordinary differential equations (ODEs) that represents the chemical reactor network of PSR can now be solved using Cantera following the algorithm in the 'Solver'-box (see Figure 1.2). The Cantera solver makes use of a numerical solver, called SUNDIALS, for ODE integration with time [20]. This numerical solver is used in AGNES as a local solver. This means that one-by-one the reactors are integrated in time by Cantera with the Backward Differentiation Formulation (BDF) for each time step until convergence is reached. Equation 1.1 shows the general formulation of the BDF

$$\sum_{k=0}^s \alpha_k y_{n+k} = \frac{t_n - t_0}{n} \beta f(t_{n+s}, y_{n+s}) \quad (1.1)$$

Because the different reactions taking place in combustion vary significantly with respect to their timescales, the system of ODEs is very stiff [20]. As shown in Figure 1.3 the variation in chemical timescales can range from nanoseconds to seconds.

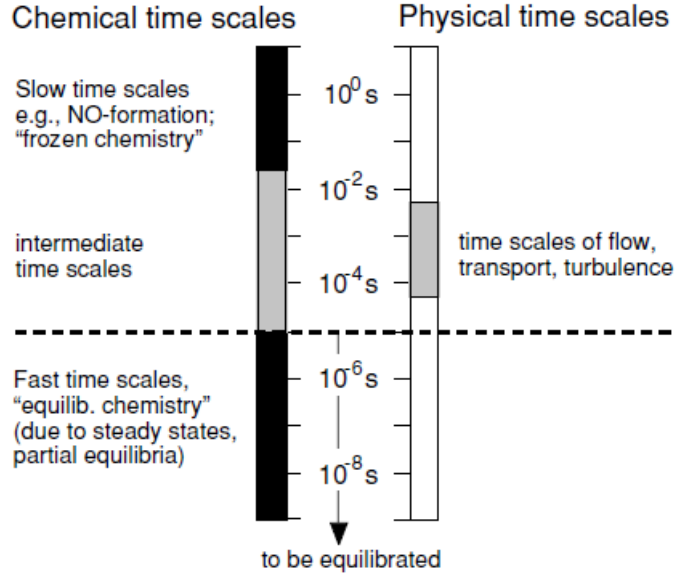


Figure 1.3: Timescales in turbulent reacting flows [4].

This means that a small time step is required to capture the faster reaction, whilst a large absolute time has to be modelled to converge the slower reactions. This means that if only a local time stepping method is used, many iterations have to be performed to reach the solution.

Global time stepping methods are used to solve for all the reactors simultaneously and are aimed at reaching convergence faster. AGNES uses a global Newton solver for this. The Newton method is a root-finding algorithm, which through Equation 1.2 finds the value for y that yields $f(y) = 0$.

$$y_{i+1} = y_i - \frac{f_i}{f'_i} \quad (1.2)$$

The governing equations of the system can be represented by Equation 1.3. In this equation ω , f , $R(\omega)$ and $g(\omega)$ are all vectors representing all the mass fractions in all the reactors, mass flows from the external environment, production inside each reactors and the net rate of species mass production, respectively. The only term left is C , which is a sparse matrix that accounts for all the convective terms.

$$g(\omega) = -C\omega + f + R(\omega) \quad (1.3)$$

By applying the Newton method to Equation 1.3, the mass fractions (ω) can be determined for which the net rate of production is 0 ($g(\omega) = 0$), as shown in Equation 1.4. In this equation J_i is the Jacobian matrix that replaces the derivative in Equation 1.2.

$$J_i \Delta\omega = -g \quad (1.4)$$

However, it is preferred to use a time-integrating global time stepping method, because these are more stable than the Newton method alone [20].

Based on the pre-research version of AGNES and the developments in the field of CFD-CRN described in section 1.2, five recommendations were made to improve upon for next versions of AGNES.

Turbulence: Currently temperature fluctuations due to turbulence present in the PSR is not modeled in AGNES [20]. However, the effect of turbulence on temperature fluctuations was found to be important by Cuoci et al. (2013), who saw a significant improvement in the results when temperature fluctuations due to turbulence were accounted for in the model [12]. It is recommended to further study the effect that the modeling of these temperatures fluctuations has on the accuracy of the emission predictions for different test cases to determine when modeling these fluctuations is useful.

Liquid Fuels: AGNES has only been used for gaseous fuels [20]. To allow research of test cases with liquid fuels, like gasoline and kerosene, some adjustments will have to be made. To ensure proper modeling of the liquid fuel spray a simulation for spray combustion of ANSYS Fluent can be used [20]. This would require some changes to the processing of the CFD results to ensure the simulation results are read correctly. For the chemistry modeling it is possible to neglect the liquid phase chemistry and just consider the gas phase. This method is based on the assumption that CFD correctly predicts droplet evaporation of the liquid fuel and the associated changes in heat release and temperature [20]. This method would require the gases formed by the droplet evaporation to enter the respective reactor as boundary inlet mass flow by including it in the source term [20].

An expected issue for running simulations for liquid fuels is the increased computational power and time associated with the larger kinetic mechanism required to model liquid fuels, like gasoline and kerosene [20]. Therefore it might be useful to also focus on the computational efficiency of AGNES to reduce the computational time for dealing with liquid fuels.

Complex geometries: AGNES was not tried on complex geometries yet [20]. The program has some hard coded zone IDs incorporated that have to be adjusted for the respective simulation [20]. Furthermore, AGNES is currently only able to handle one Fluent fluid zone [20]. In the future, it might be useful to enable multiple zones to allow the modeling of combustion systems with more complex geometries.

Global time stepping: A global Newton solver is used to solve for all the reactors once the residuals of the local solver have reached low enough values. It was found that the global Newton solver becomes unstable quickly, when the simulation is not close enough to reaching the solution [20]. This means that although the use of the global Newton solver reduces the computational time already, AGNES often has to switch back to the local solver immediately after starting the global solver. By using time-integration global time stepping it is expected that this instability is not as high and that the computational time will be reduced significantly [20]. This will enable more runs to be performed on the same test case or more complex test cases to be tackled in the same time frame.

Temperature update: In runs performed by AGNES the temperature as determined by CFD has been kept fixed under the assumption that the minor species are too low in quantity to significantly influence the temperature in the combustion system with their low heat release [20]. It is possible to update the temperature provided by CFD by solving the energy equation as done by Fichet et al. in 2010 [29]. However, Fichet et al. never compared results for keeping the temperature fixed and updating with the use of the energy equation. Therefore it is unclear what the gain is in accuracy

of solving the energy equation and whether that gain is significant. Furthermore, it would be interesting to compare the stability and solution time of both cases, since the non-linearity is increased with the energy equation.

From these five recommended research topics, the topic of updating the temperature is considered most promising, as the lack of scientific results supporting this common assumption is seen as a research gap, that can be filled whilst improving AGNES simultaneously.

In the case of modeling temperature fluctuations from turbulence, the comparison between using and not using it has already been made by Cuoci et al. [12], who determined that the modeling of turbulence has a significant effect on the accuracy of prediction. Therefore the scientific gap, in this case, is smaller than in the case of the temperature update.

Enabling the modeling of liquid fuels and complex geometries is useful for specific cases of future research with AGNES on these types of combustion systems. The method of modeling would require extensive validation of each specific test case to ensure proper modeling of the fuel and/or geometry in CFD and in the subsequent CRN. To allow proper evaluation of the modeling method for liquid fuels or multiple fluids zones, it is first essential that the use of AGNES for gaseous fuels and simple geometries is validated further.

The implementation of time-integrated global time stepping will be beneficial for any future run with AGNES, as the computational time is expected to decrease, which allows for more (complex) runs to be performed. However, the scientific value is limited to numerical procedure and global time stepping was applied for many more test cases in the field of CFD-CRN than the solving of the energy equation.

Because updating the temperature is deemed most promising compared to the other topics it is the scientific gap focused on by the research described in Section 1.4. It is expected that the increase in non-linearity of the system due to solving of the energy equation will increase the computational time required to solve it. To allow for thorough exploration of the scientific gap it is desirable to run as many simulations as possible. Therefore to allow more runs to be performed the implementation of time-integrated global time stepping will be done as a means to end improvement. This will be further discussed in Section 3.7.

1.4. TEMPERATURE PREDICTION IN CFD-CRN

In Section 1.3, it was concluded that updating the temperature with the energy equation is an interesting research gap in the field of CFD-CRN. The computational tool, called AGNES, can be improved by adjusting the program so that it can use the energy equation to update the temperature with respect to the results of the CFD computation. This temperature was previously kept fixed at the values obtained from CFD. It has been assumed by many researchers in the field of CFD-CRN that keeping the temperature fixed has no significant effect on the emission prediction [13][11][21][10].

As explained before, this assumption is based on the fact that the CFD computation already takes into account the reduced chemical kinetic mechanism containing the major species being formed for the prediction of the temperature. The use of the CRN in the hybrid method is mainly aimed at accurately determining the quantities in which the minor species are present. These minor species are present in the combustion system in much smaller quantities compared to the major species, which are considered by the CFD computation. Based on this difference in order and the relatively low heat release associated with these minor species, researchers have assumed that the contribution of these minor species to the temperature is negligible.

The adoption of a reduced chemical kinetics model increases the uncertainty of the temperature

computed by CFD. These temperatures are already subjected to uncertainties due to the necessary turbulence modelling assumptions, the parameter uncertainties related to numerical models and the inherent uncertainties of e.g. chemically reacting gases [10].

These uncertainties might not be an issue for the flow field that is not extremely sensitive to the small local differences in temperature that could be caused by the minor species [20]. This makes it possible for CFD to compute flow properties accurately when only a reduced kinetic mechanism is employed. However, for the formation rate of e.g. NO_x the sensitivity towards slight changes in temperature is very high due to the exponential dependency [20][29]. This dependency is shown by the Arrhenius equation (Equation 1.5) where the reaction rate (k) equals the temperature dependent pre-exponential factor (A) times the exponent of the activation energy (E_A) over the universal gas constant (R) times the temperature (T).

$$k = Ae^{-\frac{E_A}{RT}} \quad (1.5)$$

Furthermore, because the minor species are only present in small concentrations the impact of a local change in formation rate can easily have a large impact on the total amount of the species present. This means that if the changes in temperature due to the formation of minor species are modeled in the CRN this might significantly increase the accuracy of the prediction of these species.

By keeping the temperature fixed in the CRN, the energy equation does not have to be solved to obtain the new temperature for each PSR for each time step. This makes the system of ODEs more linear than when the energy equation has to be solved. Non-linearity combined with the stiffness of the system is associated with higher computational power and simulation time. This forms the main reason why researchers were interested in assuming the temperature could remain fixed.

In 2010, Fichet et al. researched the prediction of NO_x emission in gas turbines [29]. As mentioned it is expected that small discrepancies in temperature have a large effect on the prediction of NO_x. With temperatures above 1600K, for example, a temperature increase of 10K will cause the formation rate of NO to increase with approximately 10% [33]. Therefore Fichet et al. chose not to assume the temperature to be fixed, but solved the energy equation (Equation 1.6) instead [29]. Equation 1.6 is the energy balance for a PSR which uses the mass in the reactor (m), specific heat at constant volume (C_v), the change in temperature with time ($\frac{dT}{dt}$), the heat loss through the reactor walls (\dot{Q}), the mass flow (\dot{m}) in and out, the enthalpy (h) of the inlet and outlet stream, the reactor volume (V), the production rate of species k ($\dot{\omega}_k$) the molecular weight of species k (MW_k) and the specific internal energy of species k (u_k) [20]. Fichet et al. found a good agreement between the results from the CFD-CRN and the measurement data in terms of levels and trends [29].

$$mC_v \frac{dT}{dt} = -\dot{Q} + \sum_{in} \dot{m}_{in} h_{in} - \sum_{out} \dot{m}_{out} h_{out} - \sum_k V \dot{\omega}_k MW_k u_k \quad (1.6)$$

However, Fichet et al. did not research what the result would have been, if the energy equation had not been solved, which means there is still no quantification of the impact the assumption of fixed temperature has on the prediction results. This is a research gap that will be filled by adjusting AGNES for the option of solving the energy equation and then comparing the results of the emission predictions of a test case for different run settings. The main research question for this research is therefore:

How are the results and run performance affected by applying the energy equation to recompute the temperature in a CRN for the CFD-CRN method?

The goal of this research is to determine the impact of the assumption to keep the temperature fixed on the prediction of different emissions and how this impact is affected by different run settings for a specific test case. It was hypothesized that applying the energy equation would increase the accuracy of the emission prediction and increase the simulation time. It is expected that the extent of this increase in both is dependent on the test case and run settings analyzed, but that it would always be present.

1.5. RESEARCH OUTLINE

In the field of combustion systems, methods and tools were developed for the prediction of emissions produced by these systems. The main motivation for the development of these tools and methods is the strict legislation surrounding these emissions. It was found that amongst the approaches in literature for emission prediction in combustion systems, the hybrid approach is currently the most promising. The hybrid approach splits up the emission prediction problem by first computing the flow field using CFD with reduced chemical kinetics and then solving for detailed chemistry via a chemical reactor network (CRN) that is constructed with the results from the CFD computation.

At the Delft University of Technology the computational tool AGNES was developed that can be used to automatically cluster and solve a CRN based on results from CFD to obtain a prediction of the emissions of the combustion system. AGNES is still under development and it was recommended based on developments in the field of CFD-CRN to look into turbulence, liquid fuels, complex geometries, global time stepping and temperature updating [20].

From these five recommended research topics, the topic of updating the temperature is considered most interesting. In literature, it was found that most researchers have assumed that the temperature determined by CFD can be kept fixed. This assumption is based on the reasoning that the reduced chemistry including the major species is sufficiently accurate, because the concentrations of minor species computed with the CRN are present in too small quantities to significantly influence the temperature with their low heat release. There was a lack of scientific results supporting this common assumption.

It was argued by Fichet et al. that this assumption might not be valid for the prediction of e.g. NO_x because the formation rates are very sensitive to minor temperature changes [29]. Fichet et al. therefore used the energy equation to update the temperatures while solving the CRN [29]. There had not been any comparison between fixing the temperature or using the energy equation, which would allow the analysis of the impact of this common assumption. This was seen as a research gap, that could be filled whilst improving AGNES simultaneously.

The following research question was opted with the goal to determine the impact of the assumption to keep the temperature fixed on the prediction of minor species and what influences this impact:

How are the results and run performance affected by applying the energy equation to recompute the temperature in a CRN for the CFD-CRN method?

It was hypothesized that applying the energy equation would increase the accuracy of the emission prediction and increase the simulation time. It was expected that the extent of this increase in both is dependent on the test case and run settings analyzed, but that it would always be present. In this research, AGNES was adjusted to create the option of updating the temperature in the CRN with the energy equation as was done by Fichet et al. [29] and multiple runs were performed for different settings to determine differences between the two options to test the hypothesis.

2. THEORY

When simulating a combustion system, there are many options in terms of modeling the different physical phenomena that take place in such a process. In this chapter, the important options in simulating a combustion system are explained concisely to provide a general theoretical background for the research method described in Chapter 3.

2.1. COMBUSTION THERMODYNAMICS

A chemical reaction can be exothermic or endothermic. Exothermic reactions release energy from the reactants during the formation of the products. In case of an endothermic reaction, energy is absorbed by the reactants to form the products. Both a exothermic and endothermic reactions can be spontaneous depending on the change in Gibbs free energy. Equation (2.1) shows how the change in Gibbs free energy (ΔG) of a reaction is calculated. ΔH is the enthalpy of reaction as shown in Figure 2.1. $T\Delta S$ is the temperature times the change in entropy of the reaction.

$$\Delta G = \Delta H - T\Delta S \quad (2.1)$$

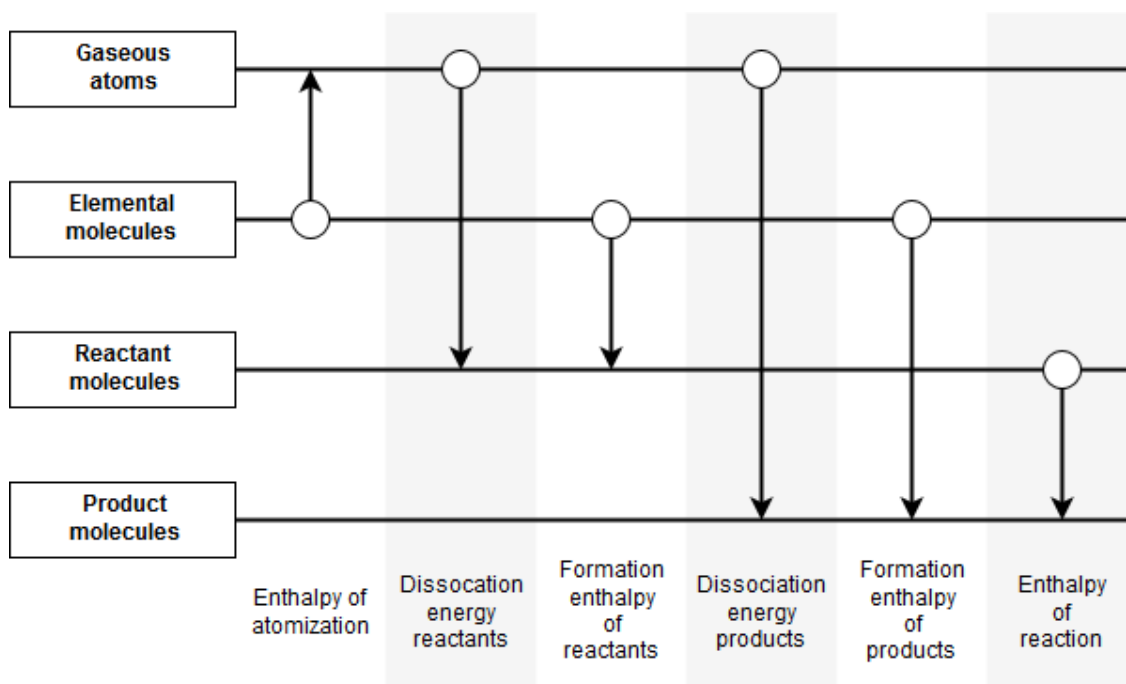
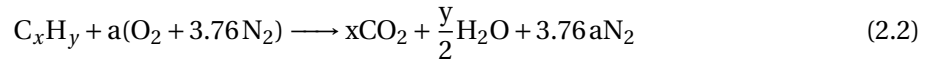


Figure 2.1: Relationship between enthalpies of formation and reaction. Based on Winterbone [5]

In case $\Delta G < 0$, the reaction is spontaneous, which is also called exergonic and when $\Delta G = 0$ then the reaction is in chemical equilibrium. Combustion is an overall exergonic exothermic set of reactions, which causes the temperature to increase due to net heat release from the fuel and oxidizer reacting. This increased temperature can in turn be used to generate power in a combustion system.

2.2. CHEMICAL KINETICS

The combustion process using a hydrocarbon fuel and air is often simplified by using the representation shown by Equation (2.2).



Equation (2.2) assumes a reaction under stoichiometric conditions, which means that precisely enough air is supplied to have all the fuel react completely with the oxygen molecules. It can be seen, that this reaction is expected to only yield carbondioxide (CO₂) and water (H₂O) as products from the reaction and the nitrogen (N₂) remains inert.

However in an actual combustion system, there are more products aside from those mentioned by Equation (2.2). The reason for this is that the reaction shown actually requires multiple steps in the form of elementary reactions to convert the reactants into the expected products. These elementary reactions have a finite rate and are mainly dependent on collisions between molecules, the orientation of the colliding molecules and the activation energy of the reaction.

There are three types of elementary reactions:

1. $A \longrightarrow \text{products}$ **Unimolecular reactions** consist of one molecule that turns into products. The most common forms of this type of reaction are the rearrangement and dissociation of the molecule, which means the molecule should consist of multiple atoms.
2. $A + A \longrightarrow \text{products}$
 $A + B \longrightarrow \text{products}$ **Bimolecular reactions** consist of two molecules, which can be the same or different and can consist of one or more atoms that react to form products.
3. $A + A + A \longrightarrow \text{products}$
 $A + A + B \longrightarrow \text{products}$
 $A + B + C \longrightarrow \text{products}$ **Termolecular reactions** involves three molecules. In this type of reaction, the third molecule absorbs the internal energy from the newly formed products and thereby avoids dissociation of the products.

These elementary reactions each have their own reaction rate and reaction order. The reaction rate determines how quickly a reaction is going in a certain direction and the reaction order tells you how dependent the reaction rate is on the amount of reactants available.

Equation (2.3) shows a generic reaction, which can take place both ways. The reaction of species A with species B has a reaction rate equal to k_1 and the reverse reaction has rate k_2 .



The change in concentration of species A ($[A]$) in Equation (2.4) can be determined by the reaction rate times the concentrations of the reactant species to the power of the relative amount necessary for the reaction.

$$\frac{d[A]}{dt} = -k_1[A]^a[B]^b = k_2[C]^c[D]^d \quad (2.4)$$

The reaction rate (k) is determined by Equation (2.5) and is computed with the temperature dependent pre-exponential factor (A'), the activation energy (E_a), the gas constant (R) and the temperature (T). This equation is also called the Arrhenius equation.

$$k = A' e^{\frac{E_a}{RT}} \quad (2.5)$$

2.3. REACTION MECHANISMS

Elementary reactions are very circumstantial. In the case of combustion of hydrocarbon fuels, the reactants in any intermediate stage of the reaction can, by chance, start to divert from the path and generate a product that is different from the expected carbon dioxide and water. To represent the array of options in reaction paths a reaction mechanism is used. Figure 2.2 shows an example of such a reaction mechanism.

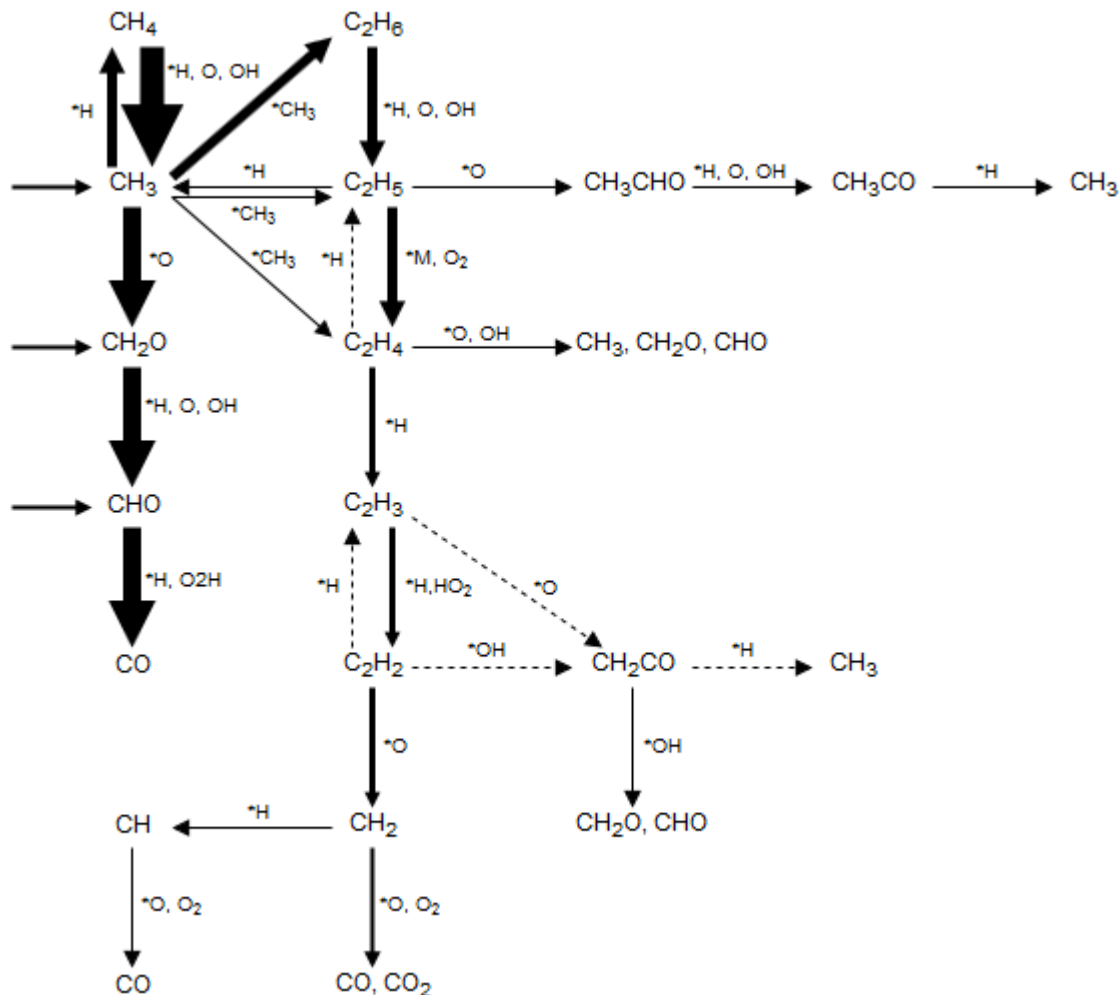


Figure 2.2: Reaction flow analysis of stoichiometric premixed Methane-air flame at atmospheric condition. Based on Warnatz [4].

As can be seen in Figure 2.2, in combustion processes using methane (CH_4) and air, the carbon atom (C) is likely to not only result in carbon dioxide (CO_2), but also carbon monoxide (CO) and other species that still include some of the hydrogen atoms (H) that are originally in the methane molecule. Reaction mechanism can range from including many species and pathways to very few to reduce the computational cost. Based on the accuracy and application the choice is made for a suitable reaction mechanism.

2.4. TRANSPORT PROCESSES

For elementary reactions of the Bi- or Termolecular type to take place a collision between reactants is required. Therefore, it is important to know where certain species are in the combustion system to determine at least the likelihood of a specific collision taking place. On top of that, the temperature

and energy at the location of that collision are important to determine the reaction rate.

The transport equations describe how a scalar quantity is transported in a space. This scalar quantity can e.g. be species mass, momentum in one direction and energy. Equation (2.6) is the transport equation of species mass. In Equation (2.6) to (2.11), t is time, ρ is the density, \vec{v} is the mixture velocity vector, \vec{V} is the diffusion velocity vector, M is the molar mass and ω is the production rate. The subscript i denotes that that quantity is specific to a certain species i .

$$\frac{\partial}{\partial t} \rho_i + \underbrace{\vec{\nabla} \cdot \rho_i \vec{v}}_{\text{mixture flux convection}} = - \underbrace{\vec{\nabla} \cdot \rho_i \vec{V}_i}_{\text{diffusion flux convection}} + \underbrace{M_i \omega_i}_{\text{mass production rate}} \quad (2.6)$$

Equation (2.7) contains the transport equation of momentum, which is also the Navier-Stokes equation. The symbols in this equation are consistent with those of Equation (2.6). There are some additional variables. $\vec{\sigma}$ is the stress tensor, which has matrix entries that correspond to Equation (2.8), \vec{g} is the gravitational acceleration vector, p from Equation (2.8) is the pressure, δ_{ij} is the Kronecker delta, μ is the dynamic viscosity, and v and x are a velocity and location vector component, respectively. In this case, i , j and k stand for the three coordinates in the Cartesian coordinate system.

$$\frac{\partial}{\partial t} \rho \vec{v} + \underbrace{\vec{\nabla} \cdot \rho \vec{v} \otimes \vec{v}}_{\text{convection}} = - \underbrace{\vec{\nabla} \cdot \vec{\sigma}}_{\text{stress divergence 2.8}} + \underbrace{\rho \vec{g}}_{\text{body forces}} \quad (2.7)$$

$$\sigma_{ij} = -p \delta_{ij} + 2\mu \left(\frac{1}{2} \left(\frac{\partial v_i}{\partial x_j} + \frac{\partial v_j}{\partial x_i} \right) - \frac{1}{6} \left(\frac{\partial v_k}{\partial x_k} + \frac{\partial v_k}{\partial x_k} \right) \delta_{ij} \right) \quad (2.8)$$

Equation (2.9) shows the transport equation for specific enthalpy. In addition to the variables specified previously, Equation (2.9) to (2.11) also contain h which is the enthalpy, \vec{j}_q which is the diffusion vector and s_e which is the source/sink term. The source/sink term can exist in Equation (2.9), even though energy is conserved, due to interchange of energy with the radiation field.

$$\frac{\partial}{\partial t} \rho h + \underbrace{\vec{\nabla} \cdot \rho h \vec{v}}_{\text{convection}} = - \underbrace{\vec{\nabla} \cdot \vec{j}_q}_{\text{diffusion}} + \underbrace{\Phi_{viscous}}_{\text{viscous dissipation 2.10}} + \underbrace{\frac{Dp}{Dt}}_{\text{pressure change 2.11}} + \underbrace{s_e}_{\text{source/sink}} \tag{2.9}$$

$$\Phi_{viscous} = \tau_{ij} \frac{\partial v_i}{\partial x_j} = \left(-\frac{2}{3} \mu \frac{\partial v_k}{\partial x_k} \delta_{ij} + \mu \left(\frac{\partial v_i}{\partial x_j} + \frac{\partial v_j}{\partial x_i} \right) \right) \frac{\partial v_i}{\partial x_j} \tag{2.10}$$

$$\frac{Dp}{Dt} \equiv \left(\frac{\partial}{\partial t} + \vec{v} \cdot \vec{\nabla} \right) p \tag{2.11}$$

2.5. TURBULENT TRANSPORT AND MODELING

Turbulent motion significantly increases the mixing of flows and is present in most combustion systems, due to the high Reynolds number. Turbulent motion is characterized by chaotic changes in pressure and flow velocity.

This behaviour can be described using eddies, which are the swirls and reverse currents created in a flow, due to turbulence. Turbulence produces eddies of the integral length scale or in energy size range with the kinetic energy of the flow. This energy is then transferred to continuously smaller and smaller scales in the inertial subrange until the dissipation range is reached. In the dissipation range the eddies are dissipated into heat by the viscous forces. The smallest eddies present in the flow are of the Kolmogorov scale. This energy cascade is also shown in Figure 2.3.

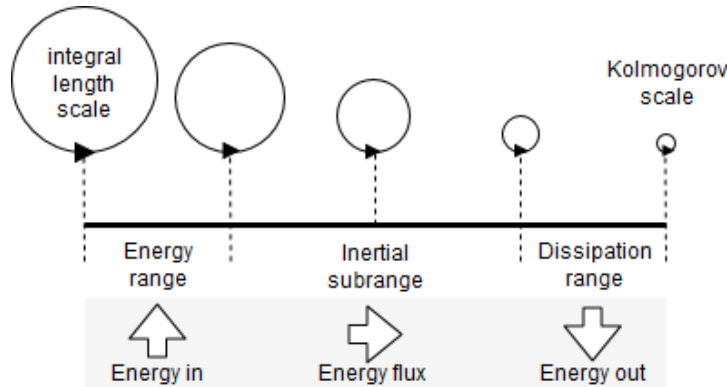


Figure 2.3: Schematic representation of the energy cascade of eddies in turbulent flow.

To simulate the turbulent flow, the grid resolution has to be smaller than the Kolmogorov scale to ensure the smallest eddies are still captured. In this way, no additional modeling is required. This type of computation is called Direct Numerical Simulation (DNS).

To allow for a coarser grid resolution and reduce the computational power required a mathematical model can be adopted to serve as a statistical approach for the turbulence. The statistical approach can use Reynolds Averaged Navier-Stokes (RANS) equations or Large Eddy Simulation (LES)

equations. Figure 2.4 shows the difference between these computational approaches in terms of resolution.

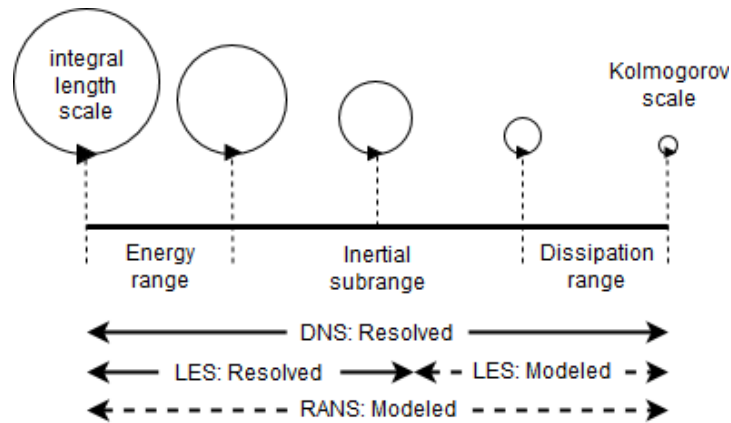


Figure 2.4: Schematic representation of the DNS, LES and RANS modeling and resolution ranges of eddies in turbulent flow.

In RANS, a closed model for mean values is constructed, which means the entire range of eddies is modeled instead of directly computed, which it would be with DNS. Therefore, when the grid resolution is sufficient to model the essential mean flow phenomena, refining the mesh will have no benefit for the results. This generally allows for a relatively coarse grid and RANS can also be applied to a 2D mesh, because the mean value is used.

In LES, a closed model for filtered values is constructed. This means that the larger scale eddies are computed and the smaller scale eddies are modeled. The dividing scale of eddies between being computed and being modeled is dependent on the grid resolution. A coarser mesh will have a larger part of the size range modeled than a finer mesh. The bounds of LES grid resolution are therefore the integral length scale and the Kolmogorov length scale, because out of these bounds the simulation would turn into RANS or DNS, respectively.

Figure 2.5 schematically shows the difference in results expected from RANS, LES and DNS

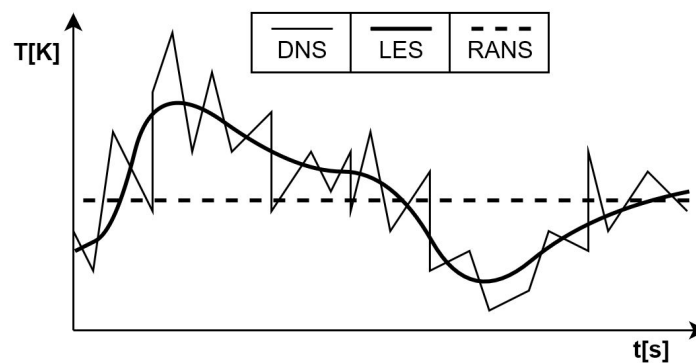


Figure 2.5: Schematic representation of local temperature time evolution computed with DNS, RANS and LES.

Equation (2.12) contains the mean transport equations for modeling by RANS and subgrid LES. The mean transport equations have three unclosed terms, that require a closure model. These are the 'Reynolds stress', 'mean source term' and 'turbulent scalar flux' for RANS and the 'subgrid stress', 'filtered source term' and 'subgrid scalar flux' for LES, which are \bar{R}_{ij} , \bar{S}_k and \bar{F}_{ki} in Equation (2.12).

$$\begin{aligned}
\frac{\partial}{\partial t}(\bar{\rho}) + \frac{\partial}{\partial x_i}(\bar{\rho} \bar{v}_i) &= 0 \\
\frac{\partial}{\partial t}(\bar{\rho} \bar{v}_j) + \frac{\partial}{\partial x_i}(\bar{\rho} \bar{v}_i \bar{v}_j) &= \left[-\frac{\partial \bar{p}}{\partial x_j} + \frac{\partial \bar{\tau}_{ij}}{\partial x_i} + \bar{\rho} g_j \right] - \frac{\partial}{\partial x_i}(\bar{\rho} \tilde{R}_{ij}) \leftarrow \text{Reynolds/Subgrid stress} \\
\frac{\partial}{\partial t}(\bar{\rho} \bar{\phi}_k) + \frac{\partial}{\partial x_i}(\bar{\rho} \bar{\phi}_k \bar{v}_i) &= \left[-\frac{\partial}{\partial x_i}(\bar{J}_i^k) + \bar{\rho} \bar{S}_k \right] - \frac{\partial}{\partial x_i}(\bar{\rho} \tilde{F}_{ki}) \\
&\quad \uparrow \qquad \qquad \qquad \uparrow \\
&\quad \text{Mean/Filtered source term} \qquad \text{Turbulent/Subgrid scalar flux}
\end{aligned} \tag{2.12}$$

Common models for closing the Reynolds/Subgrid stress (\tilde{R}_{ij}) are Spalart-Allmaras (S-A), k-epsilon ($k - \epsilon$), k-omega ($k - \omega$), Shear Stress Transport (SST) and Reynolds stress equation model (RSM). Except for RSM, all the common models use the eddy viscosity concept, which relates turbulent stresses to the mean flow to close the system of equations. Models using the eddy viscosity concept are less accurate for flow with high anisotropy, significant streamline curvature, flow separation, recirculation or those influenced by rotational effects.

The Turbulent/Subgrid scalar flux can be closed using the gradient diffusion assumption and adopting a gradient diffusion model for turbulent diffusion. However, premixed turbulent flames can showcase a flux in the opposite direction from the one predicted using this method. Therefore an additional transport equation has to be solved in some cases.

2.6. CHEMICAL SOURCE TERM MODELING

The last unclosed term is the Mean/Filtered source term. This chemical source term of a species is determined by the rate of change in concentration of that species. Equation (2.13) shows this dependency. In Equation (2.13), species i has the chemical source term S_i , the mass fraction Y_i , the molar mass M_i and the concentration C_i .

$$\rho S_i = \rho \frac{dY_i}{dt} = M_i \frac{dC_i}{dt} \tag{2.13}$$

As explained in Section 2.2 the rate of change in concentration is computed using the reaction rate, which in turn is computed with the Arrhenius equation. To close the chemical source term the mean reaction rate has to be determined. However, as can be seen in Equation (2.14), the mean reaction rate not only depends on the mean temperature (\bar{T}), but also on the temperature fluctuations ($\overline{T'^2}$, ...).

$$\bar{k} = A \exp\left(-\frac{E_a}{RT}\right) = A \exp\left(-\frac{E_a}{R\bar{T}}\right) \left(1 + \left(\frac{E_a}{2R\bar{T}} - 1\right) \frac{\overline{ET'^2}}{R\bar{T}^3} + \dots\right) \tag{2.14}$$

There are three types of methods for determining the temperature fluctuations necessary for closing the chemical source term. The first type uses a fixed flame structure, the second type models the unresolved scalar mixing and the third is specialized for LES turbulent combustion modeling.

The first type assumes that the local structure of a premixed turbulent flame is the same as that of a freely propagating laminar premixed flame. The location of the flame front is defined by the progress variable which is zero in the unburnt gas and one in the burnt gas. The flame front of these flames is dependent on laminar burning velocity, stoichiometry and fuel composition. The combinations of these variables can be tabulated and utilized to create a manifold that models the premixed, semi-premixed or non-premixed turbulent flame.

The second type includes use of the Eddy Dissipation Concept (EDC) models, Probability Density Function (PDF) models and Conditional Moment Closure (CMC).

The third type might use thickened reaction zones or direct solving of chemistry and transport with Approximate Deconvolution and Explicit Filtering (ADEF).

2.7. FLAMELESS COMBUSTION

Flameless combustion is one of the terms used to describe a combustion regime that is associated with high combustion efficiency, low combustion instability, low acoustic oscillations, low levels of soot particle emissions and extremely low levels of nitrogen oxides emissions [34] [20]. These properties make flameless combustion worth exploring as an alternative combustion concept. Flameless combustion is characterised by its well-distributed reactions, which causes its flames to not emit radiation in the visible spectrum and to decrease temperature peaks. This type of combustion can be achieved using an inlet temperature that is above auto-ignition temperature and an environment that is oxygen vitiated.

There is no general consensus on the definition of the regime boundaries or features that characterise it. Other names that refer to or overlap with the flameless combustion regime are Moderate or Intense Low Oxygen Dilution (MILD), Colourless Distributed Combustion (CDC), High Temperature Air Combustion (HiTAC), High Temperature Combustion Technology (HiCOT) and Flameless Oxidation (FLOX).

The most used definition, which was proposed by Cavaliere and De Joannon [35], is that the reactant mixture is above auto-ignition temperature at the inlet and the temperature increase with respect to the inlet temperature cannot exceed the auto-ignition temperature ($T_{in} > T_{ai} > \Delta T$).

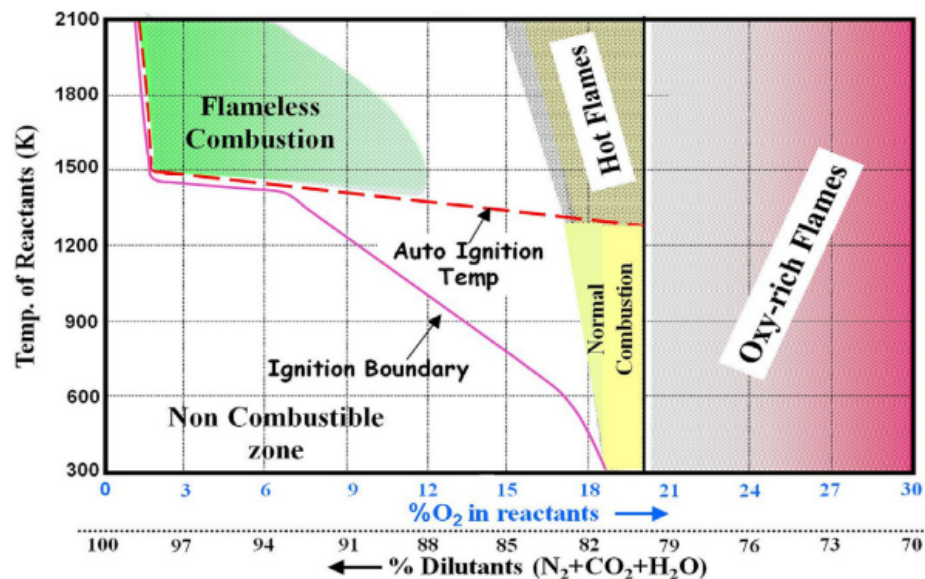


Figure 2.6: Improved combustion regime diagram proposed by Rao and Levy [6]

Regarding gas turbines, the definition of Rao and Levy [6] is most comprehensive. The improved proposed diagram in Figure 2.6 shows the influence of reactant temperatures, oxygen concentration and the recirculation ratio on the combustion regime. The diagram was generated for methane fuel using one Perfectly Stirred Reactor in Chemkin.

Flameless combustion regime was shown to have a strong interaction between turbulence and chemistry [34]. The Damköhler number (Da), which is defined as the flow (turbulence) time-scales over the chemical time-scales, is close to one. Therefore the Damköhler number can be a good indicator for flameless combustion.

3. METHOD

In this chapter, the method used for dealing with the research question is described in Section 3.1. The general steps undertaken in this research can be found in Section 3.2. The simulation test cases used to test the hypothesis is described in Section 3.3. Section 3.4 and 3.5 detail the set-up and method applied for CFD and CRN, respectively. Section 3.6 described visualisation used for the results. Section 3.7 and 3.8 mention the adjustments made to the global solver of AGNES to reduce the simulation time and solve the energy equation.

3.1. RESEARCH QUESTION RESOLVEMENT

In this section, the research question and objectives of the proposed research are described as well as how they were dealt with. The main research question was formulated as follows:

How are the results and run performance affected by applying the energy equation to re-compute the temperature in a CRN for the CFD-CRN method?

The main objective of this research is to quantify the effect of the common assumption that the temperature can be kept fixed at the value obtained from CFD. This quantification will support future research in the field of CFD-CRN by providing researchers with information relevant for judging whether this assumption can be made.

To determine the effect of applying the energy equation on the run performance, the criteria that are used to judge the run performance were established. The performance criteria that were chosen are the solver run time, the species mass fractions and the temperature.

The solver run time is automatically saved by the TU Delft computational tool, called AGNES. The run time is important to determine the expected increase of solver time associated with applying the energy equation.

The species mass fractions and temperature results from the CRN can be compared with CFD results, experimental data of the test case and with CRN results with different run settings. These comparisons can be based on absolute values, general trends and the integral below the data curve.

AGNES can use any combination of data quantities that are output by CFD as criteria to form clusters for the CRN. These clustering criteria combined with the tolerance determine which cells of the CFD mesh will be grouped and averaged. This has a significant impact on the results generated by the CRN, as it determines what data from the CFD results is lost.

The Sandia Flame D was chosen as the first test case for this research. The Sandia Flame has an axisymmetric geometry. This means that the case can be modeled as a 2D slice of the flame with an axial and radial vector from the origin, that is located at the centre of the jet.

This simplification can be applied, because the main interest in emission prediction are the species mass fractions. The mass fraction is determined by the mass of a certain species over the total mass. Therefore the exact location and timing is less important as long as the likelihood of certain reactions taking place is accurate. This allows for the use of RANS and a 2D mesh.

To determine the usefulness of applying the energy equation, thresholds were set to determine when one of the performance criteria is so low that it is not considered an option to apply the energy equation to the CFD-CRN method. Once the run settings for which applying the energy equation

does not work were ruled out the performance criteria were weighted to quantify the performance improvement or reduction and draw general conclusions.

3.2. GENERAL RESEARCH APPROACH

The main approach for answering the research question mentioned in Section 3.1 is to generate CFD results of the selected test cases and then to automatically generate and solve the CRN both with and without using the energy equation to update the temperature when solving the CRN for different set ups.

The general method for verification and validation in this research was to check for any unexpected behaviours in the results. If such a behaviour was found, convergence and boundary conditions were reevaluated. Unexpected behaviour was identified based on experimental data for CFD and based on both experimental data and CFD results for the CRN.

3.3. SIMULATION TEST CASE

There are three factors that limit the choice for a suitable test case:

- The geometry cannot be too complex. This limitation not only has to do with the fact that AGNES is currently not equipped to handle more than one Fluent fluid zone and that the zone IDs have to be assigned manually, but also with the fact that if the geometry becomes very complex the CPU time is also larger which will reduce the number of runs that can be performed.
- The fuel has to be gaseous. AGNES currently does not allow the use of liquid fuels and would require adjustments for this. Furthermore, the relatively large kinetic mechanisms associated with liquid fuels would also increase the CPU time and limit the number of runs that can be done.
- To validate the prediction data from AGNES, it is necessary that the test case has measurement data available for at least the species and temperatures inside the system. Furthermore, it might be interesting to use a test case that has been used for other research related to CFD-CRN, so that the results of AGNES can be compared to other tools to identify other possible improvements for the future.



Figure 3.1: Close-up of the SFD pilot.

An example of test cases that satisfy these considerations are the Sandia Flames. The Sandia Flames are labeled A to F and are piloted methane-air jet flames [7]. The main jet and pilot velocity increase over the range of these six flames. The associated increased probability of localized extinction is the highest in the Sandia Flame F. Sandia Flames C to F are turbulent flames, whilst Flame A is laminar and Flame B is transitional. Of this set, the measurement data of the Sandia Flame D, shown in Figure 3.1 was released one year before the others in 1998.

The measurement data includes temperature and mixture fractions of N_2 , O_2 , CH_4 , CO_2 , H_2O , H_2 , CO , OH , and NO . CO is measured by Raman scattering and more accurately by LIF [7] [1], [36]. There are also axial and radial profiles available for the flames and measurements were performed for the temperature and velocity mean and fluctuating component fields [7] [36].

The jet fluid is a mixture consisting of one part CH_4 and three parts of air by volume [7]. This mixture improves the accuracy of the scalar measurements by reducing the fluorescence interference from soot precursors significantly. The partial premixing with air reduces the flame length and increases the robustness of the flame compared to pure CH_4 . This partial premixing also allows flame operation at reasonably high Reynolds number with modest pilot and hardly any extinction. The Sandia Flames burn with high enough mixing rates that they burn as diffusion flames with a single reaction zone near stoichiometric mixture fraction and no indication of significant premixed reaction in the fuel-rich CH_4 -air mixture.

The flow rates of Sandia Flames C to F are scaled in a way that the pilot is approximately 6% of the main jet [7]. Figure 3.2 shows the dimensions of the Sandia flame set up. The bulk velocity of the Flames C to F are listed in Table 3.1.

Flame label	Bulk velocity
C	29.7 m/s
D	49.6 m/s
E	74.4 m/s
F	99.2 m/s

Table 3.1: Bulk velocities of Sandia Flames C to F [7].

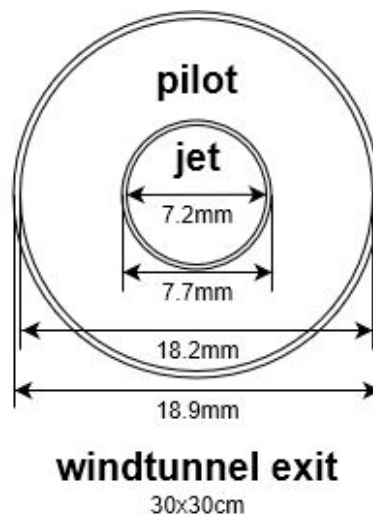


Figure 3.2: Sandia Flame dimensions [7].

The Sandia Flame D is often used as a validation test case for non-premixed combustion in the flamelet regime [36]. The reason for this is the high Reynolds number of 22400, which is desirable for model validation and the small degree of local extinction, which allows for comparison with models not including extinction [7].

Monaghan et al. (2012) [3], Monaghan et al. (2013) [30] and Nilsson (2014) [31] used the Sandia Flame D for research into pollutant formation, emission prediction and CRN construction respectively with the use of the CFD-CRN method and the extensive research of CFD simulation of the Sandia Flame D [36].

Another example of a test case that satisfies the considerations is the flameless combustion test case by Verissimo et al. [2]. The test case set up consists of a cylindrical quartz glass combustion chamber with a burner at the top and an exhaust at the bottom. The burner includes a central hole for inflowing air and 16 surrounding fuel injectors. Figure 3.3 shows the dimensions of the inlet and combustion chamber. The exhaust has a converging nozzle with a 15 degree angle and a length of 150mm.

chamber is also available. The temperature was measured with fine wire ($\varnothing 76 \mu\text{m}$) platinum/platinum 13% rhodium thermocouples. The concentration measurements were obtained using a probe ($\varnothing 1.3 \text{ mm}$) combined with a magnetic pressure analyzer, a non-dispersive infrared gas analyzer, a flame ionization detector and a chemiluminescent analyzer. The availability of the data together with the fact that this test case was already simulated with AGNES [20] and flameless combustion is an interesting alternative combustion concept [34], makes this test case stand out.

3.4. CFD METHOD AND SET-UP

The CFD results are a starting point for the CRN computation. Therefore the results of the CRN are dependent on the quality of the CFD results. If the starting point is of low quality, the CRN will never be able to generate accurate emission predictions.

The CFD simulations were done in ANSYS-Fluent and the set-up for the Sandia Flame D was adopted similar to the set-up from the research of Habibi et al. [37] and Merci et al. [38]. To arrive at the final CFD simulation set-up, multiple simulations were run with variations in the mesh spacing, viscous modeling constants ($C_{\epsilon,1}$) for the Reynolds Stress turbulence model, use of the Discrete Ordinates model for radiation and the progress variable. These simulations were performed by A.A.V. Perpignan MSc.

The CFD results for the Verissimo et al. test case were adopted from previous research performed on this test case at the Delft University of Technology [39]. The model used a $k-\epsilon$ turbulence model and Discrete Ordinates for radiation.

The selection of the CFD set-up is based on the convergence achieved with the simulation and the resemblance found between the CFD results and the experimental data of the test case. This method resulted in two CFD set-ups for the Sandia Flame D and six run cases for the Verissimo et al. test case, that were usable for AGNES. The reason not only one set-up was selected for the Sandia Flame D, was that the fit of the results varied with the axial location. Therefore the decision was made to have one set-up that was a better fit near the inlet and one that was a better fit in the far field of the Sandia Flame. For the Verissimo et al. test case, the CFD results from run case 2 were used for further simulation using AGNES, because of the experimental data available.

Both set-ups used the FGM approach to model the turbulence-chemistry interaction. The laminar flamelets for this approach were tabulated using mixture fraction, progress variable and enthalpy using the method of van Oijen and de Goey [40]. Further information on the exact set-up of the CFD of both test cases is described in Appendix A.

3.5. CRN METHOD AND SET-UP

The CRN simulation is performed using the computational tool developed by the Delft University of Technology, which is called AGNES. A few minor adjustments were made to AGNES to allow for axis-symmetric 2D cases and to centralize the hardcoded inputs required to the main run file.

The Sandia Flame D is a turbulent flame without recirculation. This means that turbulent diffusion has a significant contribution to species mixing. Turbulent diffusive mass flow rates for 2D meshes were added to AGNES using the Peclet number. The Peclet number for turbulent mass transfer ($Pe_{m,t}$) relates the advective mass flow (\dot{m}_{adv}) to the turbulent diffusive mass flow ($\dot{m}_{diff,t}$) using the velocity (u), the turbulent mass diffusivity ($D_{m,t}$) and the characteristic cell length (l_{cell}), which is assumed to be the cube root of the reactor volume, as shown in Equation (3.1). The turbulent mass diffusivity is dependent on the turbulent viscosity (μ_t), the density (ρ) and the turbulent Schmidt number (Sc_t), which is assumed to be constant at 0.7 for Equation (3.2) [3]. Combined these yields

Equation (3.3) for turbulent diffusive mass flow, in which A is the cross sectional area of the cell face.

$$Pe_{m,t} = \frac{\dot{m}_{adv}}{\dot{m}_{diff,t}} = \frac{ul_{cell}}{D_{m,t}} \quad (3.1) \quad D_{m,t} = \frac{\mu_t}{\rho Sc_t} \quad (3.2) \quad \dot{m}_{diff,t} = \frac{A\mu_t}{l_{cell}Sc_t} \quad (3.3)$$

Diffusion is not a bulk movement, therefore equal and opposite turbulent diffusive mass flow is applied at each face between PSRs to allow for turbulent species exchange [3].

The clustering algorithm of the pre-research version of AGNES uses a tolerance that is equal for all clustering criteria. The tolerance determines the range wherein the cells can be clustered for each criteria. When the cells are within all the ranges they can be clustered.

The tolerance and criteria are the same for the entire domain. However, certain parts of the domain are less interesting. This can in part be manipulated by choosing certain criteria that have a larger gradient in regions of interest. For the Sandia Flame D, this proved not to be enough, therefore optional zoning was added to AGNES to allow for different criteria and tolerances for different zones in the domain.

The CRN was computed for the two selected CFD cases of the Sandia Flame D, that are described in Section 3.4. AGNES was run for both cases with varying number of reactors to perform a grid independence study. This study is usually used to determine the minimum amount of reactors required to obtain an accurate enough solution. For accuracy, it is important to have sufficient resolution of the CRN in the regions with more chemical activity. The distribution and resolution of reactors is dependent on the clustering criteria and the tolerance.

During the grid independence study, several combinations of criteria and tolerances were tried to obtain the most suitable combination and show grid independence. Unfortunately, it was found that the required resolution was not reached in the essential areas, whilst the total number of reactors and the solve time was already high. Therefore the computational domain was split into zones with each their own tolerances according to the method by Monaghan et al. [3], which uses the static temperature, mean mixture fraction and axial coordinate to increase grid resolution in e.g. higher temperature regions. To validate this approach, a sensitivity study was performed as well as a comparative study of results with and without zoning, and with and without changing tolerances.

The CRN results of the Verissimo et al. test case were validated by reproducing the results of a previous study of this test case by researchers at the Delft University of Technology for run case 2 [39]. Only one run case was evaluated due to time constraints and run case 2 was selected, because it had more experimental data.

The Verissimo et al. test case was also simulated using the Monaghan et al. method, that proved to be effective for the Sandia Flame D, to see what the effect of this method is on another test case.

In the pre-research version of AGNES, the heat flux at the burner wall was taken from CFD and kept constant. However, it was found that when the solver is updating the temperature using the energy equation this constant heat flux lead to diverging issues. Therefore the heat flux (\dot{Q}_{wall}) was made temperature dependent by calculating it using the heat transfer coefficient (UA) with the heat flux and temperature near (T) and outside the wall (T_{env}) from CFD following Equation (3.4). The heat transfer coefficient was calculated using the heat flux and temperatures from CFD.

$$\dot{Q}_{wall} = UA(T - T_{env}) \quad (3.4)$$

To verify the results of the CRN in general, the total and individual mass flows of species going in and out of the system is checked. The mass flow in and out of the system should be equal, because

the problem is simulated as steady. Furthermore, the ratio of atoms of the in and out flow cannot change either. Convergence was verified by checking if all changes in species concentrations and temperature, have a relative error value below $1e-6$.

To validate the results of the Sandia Flame D, the CRN results were averaged by taking the volume integral of that variable over the cross sectional volume corresponding to the experimental data available of the test case. The same is done for the CFD and experimental results. These volume integral averaged results are compared between the CRN, CFD and experimental results. For the Verissimo et al. test case profile plots coinciding with the experimental data available were compared for validation.

The exact set-up of the CRN for both test cases is described in Appendix B and details of the changes to AGNES were logged in the changelog included in Appendix C.

3.6. RESULT VISUALISATION

The aim of result visualisation is to allow for a fair comparison between results. In this research, the results of the CFD and CRN run cases are compared with each other and the experimental data provided on the test case. The experimental data for the Sandia Flame D and Verissimo et al. test case is only available at specific axial locations for a radial profile. In case of the Verissimo et al. test case the data points are in the form of a rectangular grid (see Table 3.3) from the centre over one of the sixteen fuel inlets. The Sandia Flame D has a varying range dependent on the axial location as can be seen in Table 3.4.

z(mm)	11	45	79	113	147	181	215	250	280	310
r(mm)	0	5	10	15	20	25	35	40	45	

Table 3.3: Axial and radial coordinates of experimental data measurement result Verissimo et al. test case.

x/d	1	2	3	15	30	45	60	75
r/d	1.9	1.9	2.18	3.06	5.83	7.78	9.72	11.11

Table 3.4: Relative axial location and respective relative radial range of experimental results Sandia Flame D ($d=0.0072$)

One way of visualising the data is making plots at each axial location over the radial ranges mentioned in Table 3.4. These plots can be used to compare the curve fitting of the results of CFD and CRN.

In addition to this, the volume integral average for each of these axial locations can be calculated. By using the volume integral averaged value, the proximity of the result can be evaluated based on the quantities irrespective of the curve fitting.

Equation (3.5) shows how this average can be obtained for this case. x and r are the axial and radial locations. Y is the mass fraction of a species, but can be replaced by any other output parameter and V is the volume.

$$\langle Y(x) \rangle = \frac{\int_0^V Y(x,r) dV}{\int_0^V dV} \quad (3.5)$$

The volume integral can be approximated using a sum of the cells corresponding to the axial location. In Equation (3.6), the volume is approximated by the area of the cell parallel to the axial and radial coordinate ($A(x,r)_i$) times the circumference associated with the radial location of the cell ($2\pi r_i$).

$$\langle Y(x) \rangle = \frac{\sum_{i=0}^n 2\pi r_i \cdot A(x, r)_i \cdot Y(x, r)_i}{\sum_{i=0}^n 2\pi r_i \cdot A(x, r)_i} \quad (3.6)$$

The cell area can be described as the radial and axial distances within the cell ($dr_i dx_i$). The axial distance is constant for cells of the same axial location. Therefore, some values can be canceled from the sums. This is shown in Equation (3.7) and leaves the simplified calculation to determine the mass average.

$$\langle Y(x) \rangle = \frac{\sum_{i=0}^n 2\pi r_i \cdot dr_i dx_i \cdot Y(x, r)_i}{\sum_{i=0}^n 2\pi r_i \cdot dr_i dx_i} \quad (3.7)$$

Equation (3.7) assumes the output value remains constant over the entire width of the cell, irrespective of the values in adjacent cells. To reduce the error created by local over and underprediction of this constant value, the trapezoidal rule is applied. This difference is demonstrated with Figure 3.4.

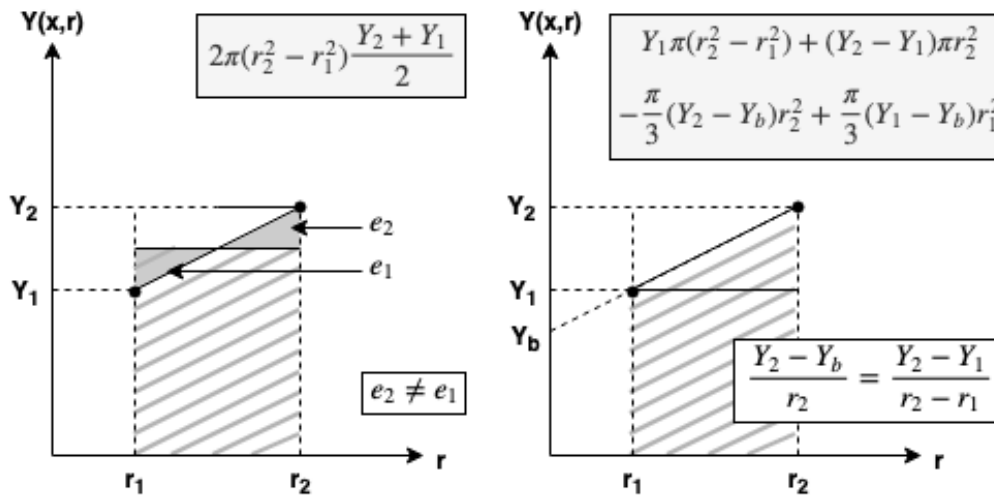


Figure 3.4: Surface integration method comparison

3.7. SIMULATION TIME REDUCTION

As explained in Section 1.4, to properly research the effect the fixed temperature assumption has on the CFD-CRN method, it is important that many runs for different settings are performed. The amount of runs that can be performed is highly dependent on the time it takes to perform one run. This simulation time is dependent on the complexity of the run case performed and the efficiency of the solver. The run case complexity consists of the complexity of the test case, the amount of detail of the kinetic mechanism, the amount of reactors and the type and amount of clustering criteria used by AGNES [20].

The test case complexity is related to the geometrical complexity, the fuel composition and the amount of recirculation and local extinction. By choosing a test case like e.g. the Sandia Flame D, the complexity of the test case is kept low. As discussed in Section 1.4, the Sandia Flame D has a simple geometry with a gaseous fuel. Furthermore, it has little to no recirculation nor local extinction [36].

Because a gaseous fuel will be used, the kinetic mechanism is relatively small. By using the GRI-Mech 3.0 kinetic mechanism in AGNES the level of detail is deemed sufficient and the amount of CPU power and the stability are kept at an acceptable level as well [20][10].

By reducing the number of reactors used the computational time of AGNES is reduced as well. Therefore it is optimal when runs are performed with the minimum number of reactors that can still accurately represent the computational domain. To determine this minimum number of reactors a grid independence study will have to be performed for the chosen test case [20].

AGNES allows the use of any combination of the results from the CFD simulation as clustering criteria [20]. Optimization of the number of reactors is possible by choosing clustering criteria that highly influence the emission production. The number of clustering criteria is indirectly limited by the tolerance, because relaxation of the tolerance is required to achieve the desired number of reactors when the clustering process is highly constraint [20]. Therefore tests were performed to determine the most critical combination of criteria [20].

As previously stated, the computational time of AGNES is also dependent on the efficiency of the solver. This solver efficiency is largely determined by the time stepping of the system. In Section 1.3 it was explained that the global time stepping of AGNES can still be improved. AGNES uses a global Newton method when the residuals of the local time stepping method drop below a set limit. Unfortunately, the global Newton method is prone to instability when the solution is not sufficiently close [20]. This meant that without global time integration AGNES often has to switch back to the local solver after just one iteration of the global Newton method [20].

The local solver uses the SUNDIALS [41] package, called CVODE, through the time integration function provided within Cantera [20]. This function cannot be utilized for the global solver, because Cantera handles the input as a dense matrix. The matrix containing all reactor is too large for this type of handling. Therefore the SUite of Nonlinear and Differential/Algebraic equation Solvers (SUNDIALS) package is employed using the `scipy.integrate.BDF` [42] python wrapper function that can handle large sparse systems.

The global time integration is implemented in such a way, that it is only used when the Newton solver is diverging. This change reduced the simulation time.

3.8. GLOBAL SOLVER ENERGY CONSERVATION

The global solver in AGNES is custom written, because the matrix including all the reactors is too large for Cantera to handle. Part of this global solver is calculating a Jacobian matrix at each time step. Figure 3.5 and Figure 3.6 show general structure of the two Jacobian matrices that together form the Jacobian matrix for the entire reactor network. The Jacobian is a square matrix with a size equal to the number of reactors times the number of variables to be solved.

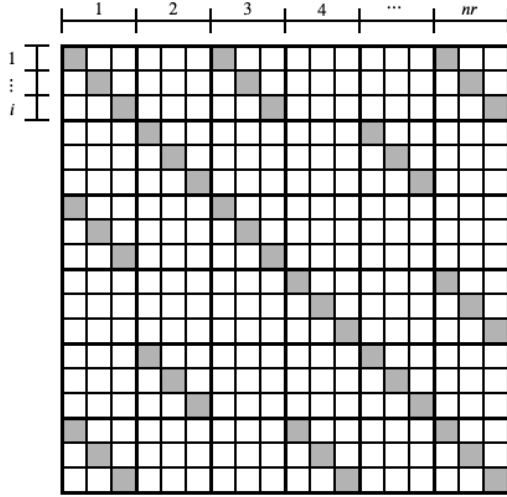


Figure 3.5: Jacobian sample structure accounting for reactor inter-connectivity (J_s) with nr as the number of reactors and i as the amount of variables to be solved for each reactor.

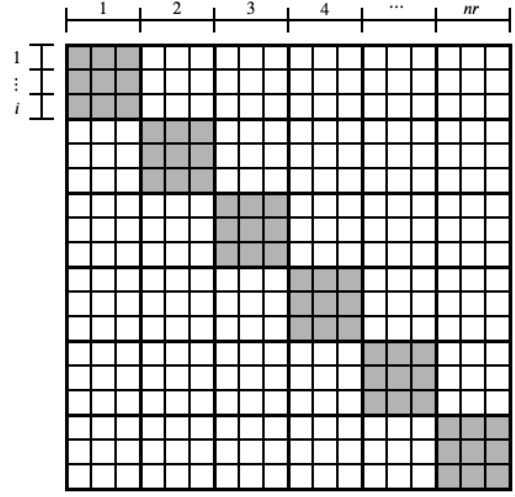


Figure 3.6: Jacobian sample structure accounting for reactions within the reactors (J_w) with nr as the number of reactors and i as the amount of variables to be solved for each reactor.

Jacobian J_s (Figure 3.5) contains the terms in the conservation equations related to the connections between reactors. J_s is a sparse matrix because each reactor is only connected to a few surrounding reactors. Jacobian J_w (Figure 3.6) contains the terms in the conservation equations related to the reactions taking place in the reactor itself. This causes the matrix to be sparse and terms to be close to the diagonal, since only variables within the reactor have an effect.

The pre-research version of AGNES did not solve the energy equation to update the temperature provided by CFD. This means that for each reactor the vector to be solved is the list of species. When the energy equation is taken into account, the temperature has to be added as a row and column in J_s and J_w for each reactor.

Equation (3.8) is the equation for energy conservation, which is also described in Section 1.4. This equation can be expanded in the form of Equation (3.9) to show that h_{in} , u_k and $\dot{\omega}_k$ and \dot{Q}_{wall} are all functions of temperature (T). \dot{Q}_{wall} only applies for reactors at the combustor wall.

$$mC_v \frac{dT}{dt} = \sum_{in} \dot{m}_{in} h_{in} - \sum_{out} \dot{m}_{out} h_{out} - \dot{Q}_{wall} - \sum_k V \dot{\omega}_k MW_k u_k \quad (3.8)$$

$$mC_v \frac{dT}{dt} = \sum_{in} \dot{m}_{in} C_{p,in} T_{in} - \sum_{out} \dot{m}_{out} C_p T \quad (3.9a)$$

$$- UA_{wall} (T - T_{env}) - \sum_k V \dot{\omega}_k (T) MW_k C_{v,k} T \quad (3.9b)$$

$$(3.9c)$$

For J_s the terms in the temperature rows and columns are the energies exchanged between reactors, which is calculated by differentiating the left-handside of Equation (3.9a) with respect to temperature. Equation (3.10) shows the resulting equation for temperature in J_s .

$$J_s = \sum_{in} \dot{m}_{in} C_{p,in} - \sum_{out} \dot{m}_{out} C_p \quad (3.10)$$

The terms in the temperature rows and columns of J_w relate the change in species production rates to the change in temperature. This is obtained by differentiating Equation (3.9b). This differentiation uses the product rule as the term contains a multiplication of two functions of T . The function of the net rate of production ($\dot{\omega}$) is the sum of the stoichiometric coefficients (ν) and the net rate of progress of reactions (r) for all the reactions (Nr), as shown in Equation (3.11).

$$\dot{\omega}_k = \sum_m^{Nr} \nu_{mk} r_m \quad (3.11)$$

The net rate of reaction progress equals the forward minus the reverse rates of reaction progress, which are a function of the respective reaction rate coefficients (k), the species concentration (C) and the stoichiometric coefficients (ν), as is formulated by Equation (3.12).

$$r = r_f - r_r = k_f \prod_{i=1}^{n1} c_i^{\nu_{f,i}} - k_r \prod_{j=1}^{n2} c_j^{\nu_{r,j}} \quad (3.12)$$

Equation (3.12) can be escalated into Equation (3.13) to show its dependency on temperature through the Arrhenius equation and the equilibrium rate constant (K_{eq}).

$$r = AT^\beta \exp\left(-\frac{E_a}{RT}\right) \prod_{i=1}^{n1} c_i^{\nu_{f,i}} - \frac{A}{K_{eq}} T^\beta \exp\left(-\frac{E_a}{RT}\right) \prod_{j=1}^{n2} c_j^{\nu_{r,j}} \quad (3.13)$$

When taking the temperature derivative of the net rate of progress of reaction Equation (3.14) is obtained, which is used to compute the temperature related terms in J_w with Equation (3.15).

$$\frac{\partial \dot{\omega}_k}{\partial T} = \sum_m^{Nr} \nu_{mk} \left(\frac{\beta}{T} + \frac{E_a}{RT^2} \right) r_m \quad (3.14)$$

$$J_w = -UA_{wall} - \sum_k VMW_k \left(\dot{\omega}_k(T) C_{v,k} + C_{v,k} T \sum_m^{Nr} \nu_{mk} \left(\frac{\beta}{T} + \frac{E_a}{RT^2} \right) r_m \right) \quad (3.15)$$

4. RESULTS AND DISCUSSION

Using the method described in Chapter 3 results were obtained that are shown in this chapter. The effect of the turbulent diffusion modeling on the Sandia Flame D is shown in Section 4.1. The sensitivity of the zoning method used by Monaghan et al. [3] for the Sandia Flame D is explored in Section 4.2, as well as the effect of this type of clustering on the Verissimo et al. test case. Section 4.3 shows the results of the grid independence study performed for the Sandia Flame D. The comparison between the CFD results and the results from the CRN is provided for the Sandia Flame D and Verissimo et al. test case in Section 4.4. Section 4.5 and Section 4.6 shows the results regarding the research question posed in this thesis.

4.1. TURBULENT DIFFUSION MODELING

To improve the results from AGNES with respect to the species diffusivity, a turbulent diffusion model was added for the Sandia Flame D. This section shows the type of effect the diffusion model described in Section 3.5 has.

Figure 4.1 to 4.3 show the effect the turbulent diffusion model using the Peclet number has on the species mass fractions for the same CRN cluster at the axial location, which is furthest from the inlet. At this axial location the effect of the diffusion was the largest. This is probably due to the increased size of the clusters, which causes the species exchanged due to diffusion to travel larger distances, because the reactors are perfectly stirred.

On the major species the diffusion model has a small effect, which is shown in Figure 4.1. The mass fraction near the center decreases more than it does radially outward. This suggests the species are traveling more in the radial direction.

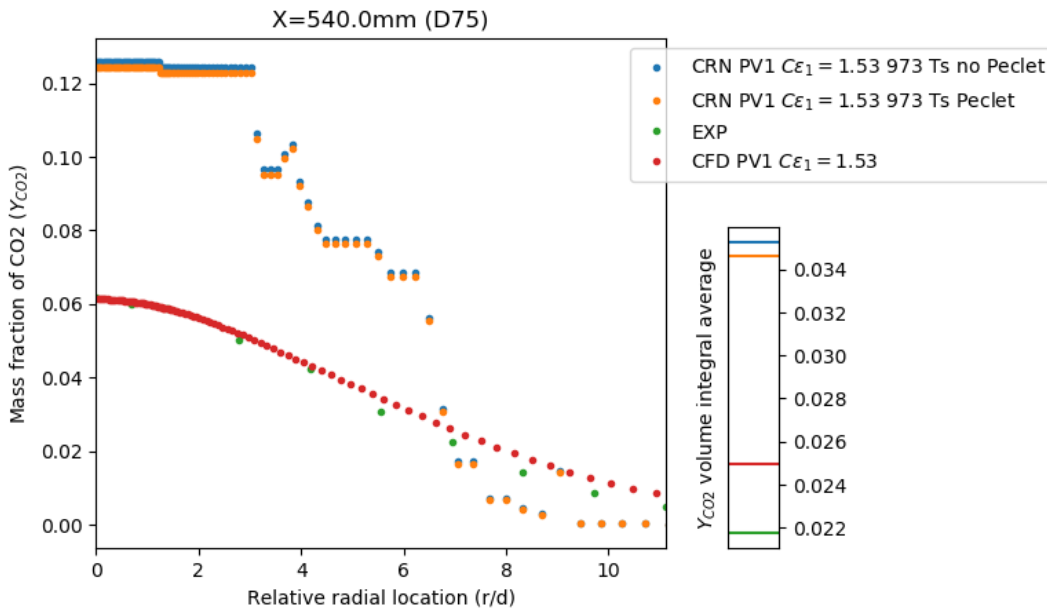


Figure 4.1: Experimental (●), CFD PV1 $C\epsilon_1 = 1.53$ (●) and CFD-CRN predicted profiles (left) and volume integral averages (right) of **Mass fraction of CO2** in the radial direction at axial location **D75** ($x/d_{jet} = 75$) for CRNs with **973** PSRs with static temperature clustering **without** (●) and **with Peclet turbulent diffusion modeling** (●).

In general, there is a small decrease in species mass fraction, which is also shown by the volume

integral average. The same trend is seen for H_2O and the inverse for O_2 . At the same axial coordinate, the mass fraction of CH_4 is near zero, which means more minor species from dissociation reactions are formed, which is closer to the experimental data. This increased amount of dissociation is most likely caused by the methane diffusing more into the hot pilot stream.

For the minor species the effect is relatively larger. For the mass fraction of CO , the same trend is found as with CO_2 , but the off-set between the results near the center is larger. This can be seen in Figure 4.2. In case of NO (Figure 4.3), the effect is again more pronounced near the inlet, but instead the mass fraction is increased by using the turbulent diffusion model.

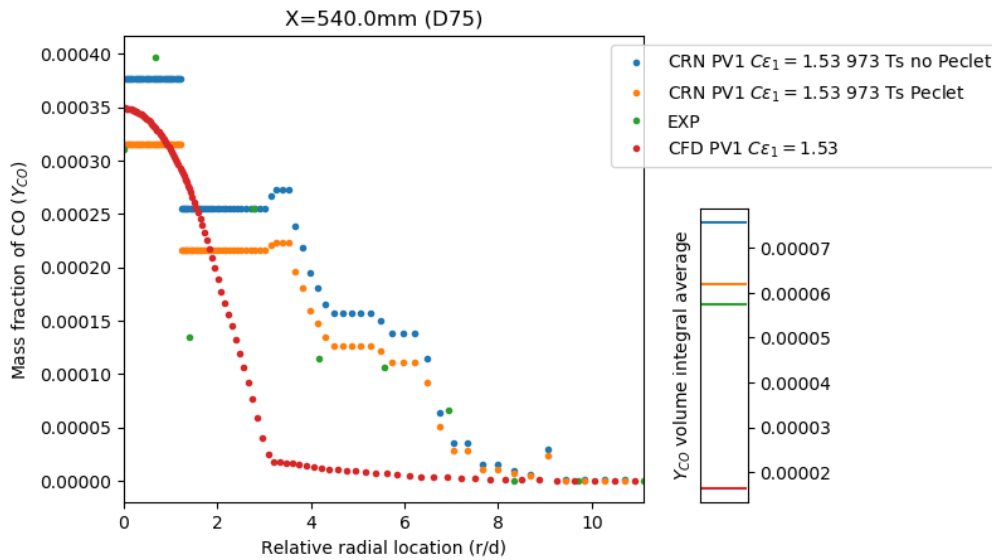


Figure 4.2: Experimental (\bullet), CFD PV1 $C\epsilon_1 = 1.53$ (\bullet) and CFD-CRN predicted profiles (left) and volume integral averages (right) of **Mass fraction of CO** in the radial direction at axial location **D75** ($x/d_{jet} = 75$) for CRNs with **973** PSRs with static temperature clustering **without** (\bullet) and **with Peclet turbulent diffusion modeling** (\bullet).

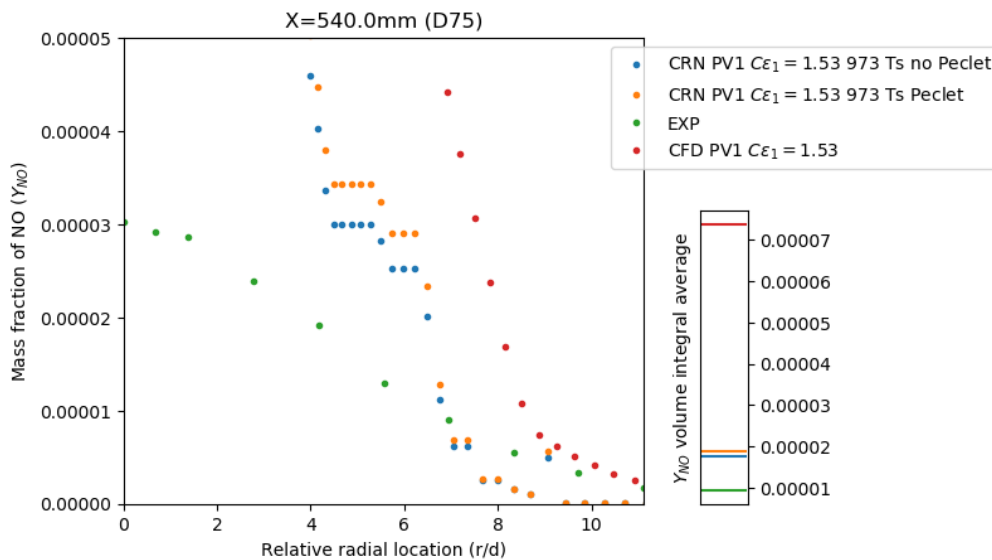


Figure 4.3: Experimental (\bullet), CFD PV1 $C\epsilon_1 = 1.53$ (\bullet) and CFD-CRN predicted profiles (left) and volume integral averages (right) of **Mass fraction of NO** in the radial direction at axial location **D75** ($x/d_{jet} = 75$) for CRNs with **973** PSRs with static temperature clustering **without** (\bullet) and **with Peclet turbulent diffusion modeling** (\bullet).

Compared to the experimental results and CFD, the radial profiles produced by the CRN still have steep trends for the major species after adding the turbulent diffusion model.

This can be explained by the shape and size of the clusters in the CRN. Due to the pilot and jet streams in the Sandia Flame D, the clusters tend to elongate in the axial direction. This together with the use of PSRs causes species travel in the axial direction to be exaggerated. This effect could potentially be reduced in future research by using PFRs.

4.2. ZONING METHOD SENSITIVITY AND EFFECTS

In Section 3.5, it was mentioned for the Sandia Flame D (SFD) that the computational domain was split according to the suggested method by Monaghan et al. in [3]. Table 4.1 shows the zoning and tolerances applied using the temperature (T), mean mixture fraction (f) and axial coordinate (x).

Table 4.1: Zone limits and reactor criteria as specified by Monaghan et al. [3].

	zone limits	reactor criteria limits
	$0 \leq f \leq 0.01$	$\Delta x = 0.2\text{m}$
	$0.01 < f \leq 0.1$	$\Delta T = 100\text{K}$
	$0.1 < f \leq 0.9, T \leq 1800\text{K}$	$\Delta T = 100\text{K}$
	$0.1 < f \leq 0.9, 1800\text{K} < T \leq 2000\text{K}$	$\Delta T = 50\text{K}$
	$0.1 < f \leq 0.9, 2000\text{K} < T$	$\Delta T = 2\text{K}$
	$0.9 < f \leq 1.0$	$\Delta f = 0.01, \Delta x = 0.01\text{m}$

The Monaghan et al. method on average resulted in better curve fitting and total quantities with respect to experimental results compared to the previous clustering attempts with the Sandia Flame D. It was hypothesized that the Monaghan et al. method could achieve this due to two reasons:

- The zoning identifies regions of special interest with e.g. mean mixture fraction near stoichiometry and higher temperatures.
- The tolerance can locally be decreased to lower values than is achievable with the previous clustering method, which only used global tolerances.

In this work, Monaghan et al. only states the zoning and tolerances used and does not specify the motivations behind the numbers provided. Therefore a sensitivity and comparative study was performed to test the effect of the tolerances and zones used.

ZONED TOLERANCE SENSITIVITY

The blue values in Table 4.1 have a lower tolerance than is desirable for the previous clustering method as it would increase the number of reactors and thereby computational time too much. Therefore the sensitivity of these values was studied by increasing the tolerance and comparing the results, which are in part shown in this section.

The first subject of the sensitivity study is $\Delta f = 0.01$, which is used in the fuel rich zone close to the jet and pilot inlet of the domain. The tolerance was doubled to see what effect that had on the CRN results.

Figure 4.4 shows one of the plots at $x/d_{jet} = 15$ used to compare the results using $\Delta f = 0.01$ and 0.02 . It can be seen that between 1.0 and 2.5 r/d the latter case shows a large number of orange dots at a constant number. This suggests that for this case this entire section of the slice is approximated by one reactor opposed to five in the original case.

When cross-referencing this observation with the reactor distribution, this revealed that the distribution of reactors is not ideal and not enough reactors are representing this region. This results

in a deterioration of curve fitting and predicted quantities of species in this region and the regions downstream.

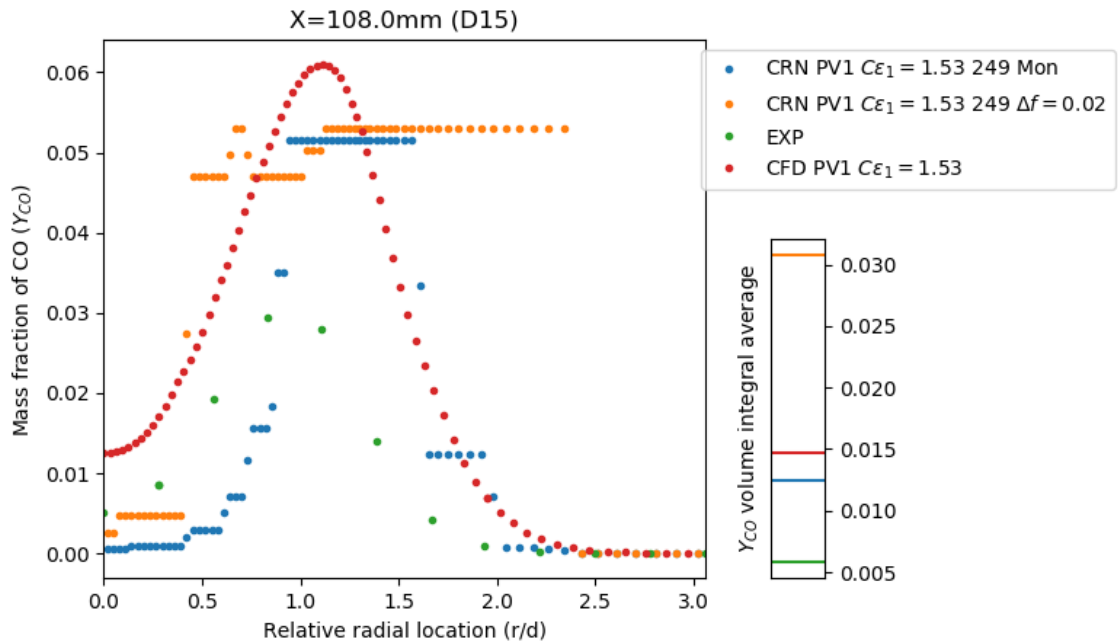


Figure 4.4: Experimental (\bullet), CFD PV1 $Ce_1 = 1.53$ (\bullet) and CFD-CRN predicted profiles (left) and volume integral averages (right) of **Mass fraction of CO** in the radial direction at axial location **D15** ($x/d_{jet} = 15$) for CRNs with **249** PSRs in the **original Monaghan clustering** (\bullet) and **249** PSRs in **Monaghan clustering with $\Delta f = 0.02K$ substituted for $\Delta f = 0.01$** (\bullet).

The next subject of the sensitivity study is $\Delta T = 2K$, which is used in the highest temperature range of the flame zone. The tolerance was again doubled to see the effect. However, it was found that the clusters did not change for the new tolerance. The tolerances $\Delta T = 4K$ and $8K$ were tried until at $\Delta T = 16K$ a change in clusters was observed.

Figure 4.5 to 4.8 show some of the plots generated to compare the use of $\Delta T = 2K$ and $16K$. Figure 4.5 shows the temperature profile at $x/d_{jet} = 45$. This profile is closest to the highest temperature range and it can be seen that the volume integral average temperature is higher in the case of $\Delta T = 16K$, due to the difference in reactor distribution. Further downstream this average actually dives below that of the original case.

Figure 4.6 is the profile of the mass fraction of CH_4 at the same axial location. Upstream the results of both cases are closely resembling each other, but at this location the mass fraction of CH_4 is significantly lower for $\Delta T = 16K$. This together with the average increase of the mass fraction of NO downstream shown in Figure 4.8 and Figure 4.7 showing a sudden drop in the mass fraction of CO , suggest the temperature is increased in this region due to the decrease in resolution.

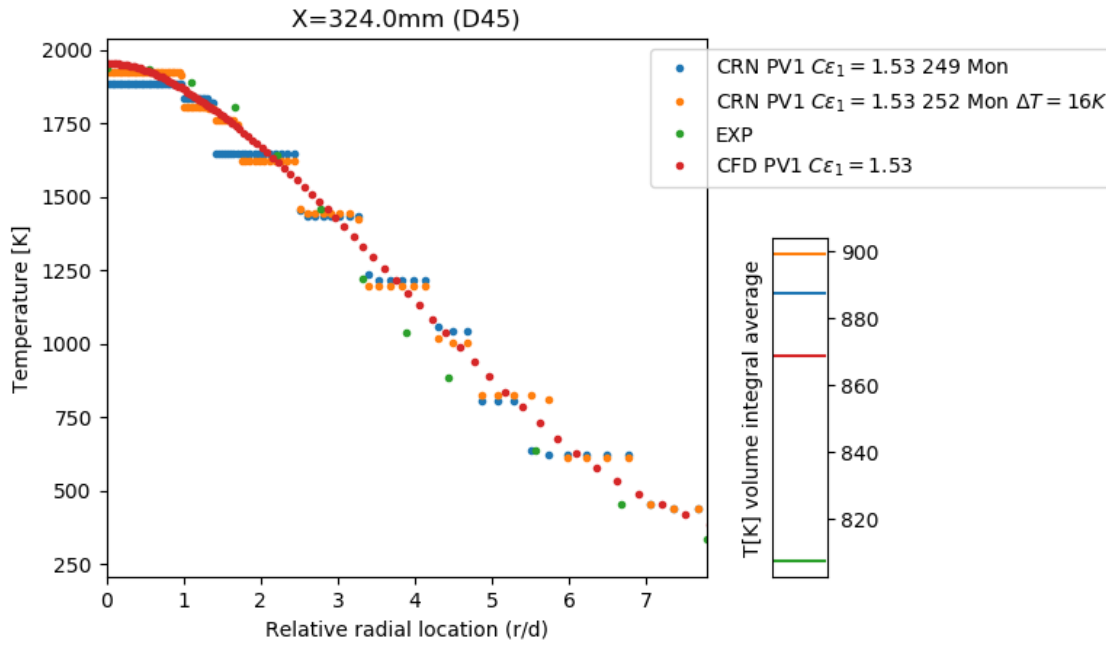


Figure 4.5: Experimental (●), CFD PV1 $C_{\epsilon_1} = 1.53$ (●) and CFD-CRN predicted profiles (left) and volume integral averages (right) of **Static Temperature** in the radial direction at axial location **D45** ($x/d_{jet} = 45$) for CRNs with **249** PSRs in the **original Monaghan clustering** (●) and **252** PSRs in **Monaghan clustering with $\Delta T = 16K$ substituted for $\Delta T = 2K$** (●).

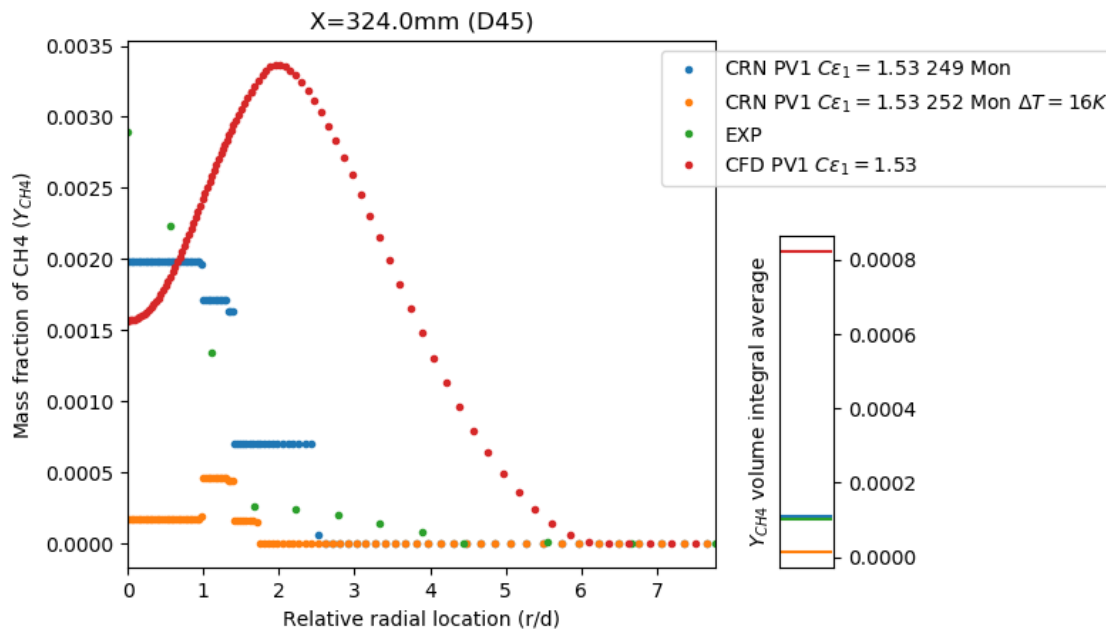


Figure 4.6: Experimental (●), CFD PV1 $C_{\epsilon_1} = 1.53$ (●) and CFD-CRN predicted profiles (left) and volume integral averages (right) of **Mass fraction of CH4** in the radial direction at axial location **D45** ($x/d_{jet} = 45$) for CRNs with **249** PSRs in the **original Monaghan clustering** (●) and **252** PSRs in **Monaghan clustering with $\Delta T = 16K$ substituted for $\Delta T = 2K$** (●).

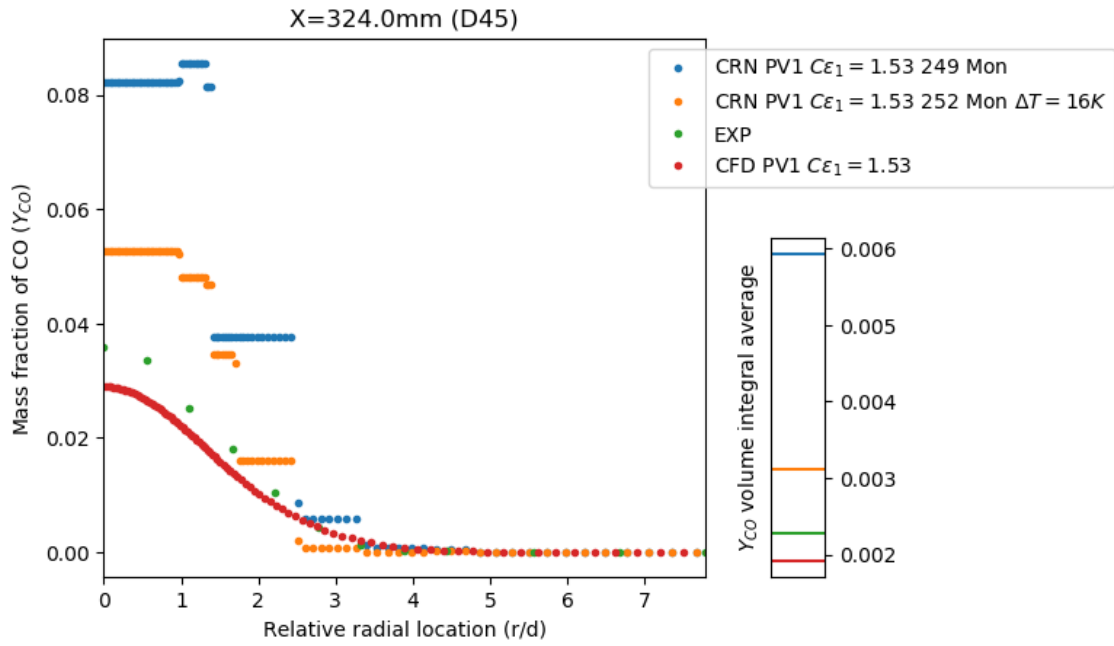


Figure 4.7: Experimental (\bullet), CFD PV1 $C\epsilon_1 = 1.53$ (\bullet) and CFD-CRN predicted profiles (left) and volume integral averages (right) of **Mass fraction of CO** in the radial direction at axial location **D45** ($x/d_{jet} = 45$) for CRNs with **249** PSRs in the **original Monaghan clustering** (\bullet) and **252** PSRs in **Monaghan clustering with $\Delta T = 16K$ substituted for $\Delta T = 2K$** (\bullet).

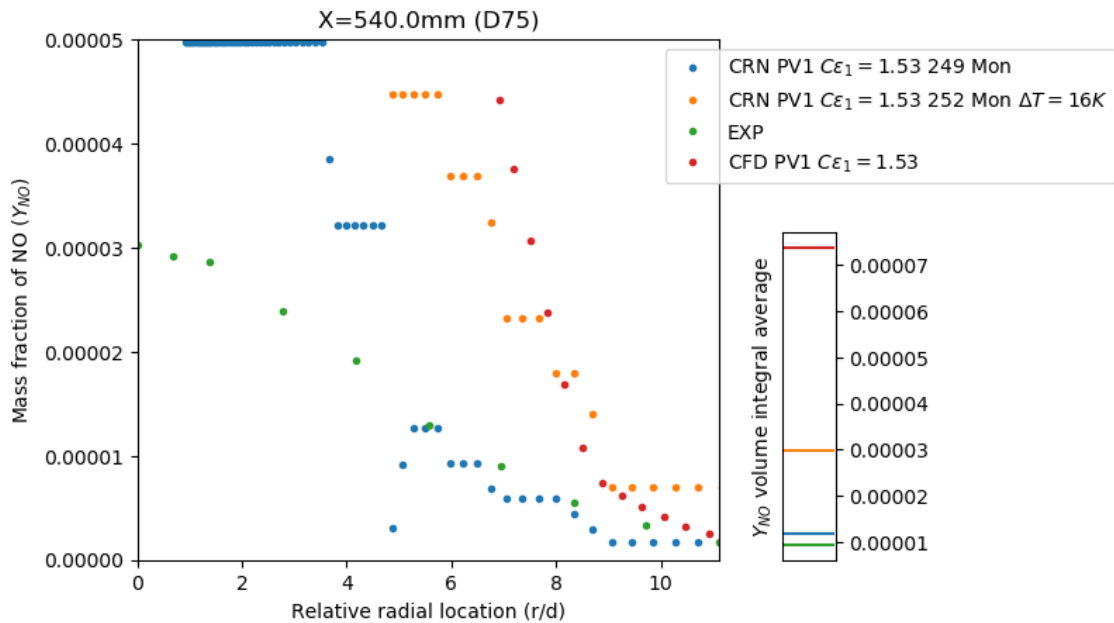


Figure 4.8: Experimental (\bullet), CFD PV1 $C\epsilon_1 = 1.53$ (\bullet) and CFD-CRN predicted profiles (left) and volume integral averages (right) of **Mass fraction of NO** in the radial direction at axial location **D75** ($x/d_{jet} = 75$) for CRNs with **249** PSRs in the **original Monaghan clustering** (\bullet) and **252** PSRs in **Monaghan clustering with $\Delta T = 16K$ substituted for $\Delta T = 2K$** (\bullet).

The last subject of the sensitivity study is $\Delta T = 50K$, which is used in the next highest temperature range in the flame zone. In this case, the tolerance was increased to $\Delta T = 75K$ to determine its effect. It was found, that there was a very similar trend visible as with $\Delta T = 2K$ vs $\Delta T = 16K$. The differences are that the onset of the behavior can sometimes already be seen at $x/d_{jet} = 30$ and the effect on the major species is relatively more pronounced, as can be seen in Figure 4.9 in the

ranges 28-35 and 52-60 x/d . The more upstream visibility makes sense as the zone of the second highest temperature range stretches further than that of the highest temperature range. Regarding the more pronounced effect on the major species is also logical, since the region of the second highest temperature range surrounds the highest temperature range and is therefore larger.

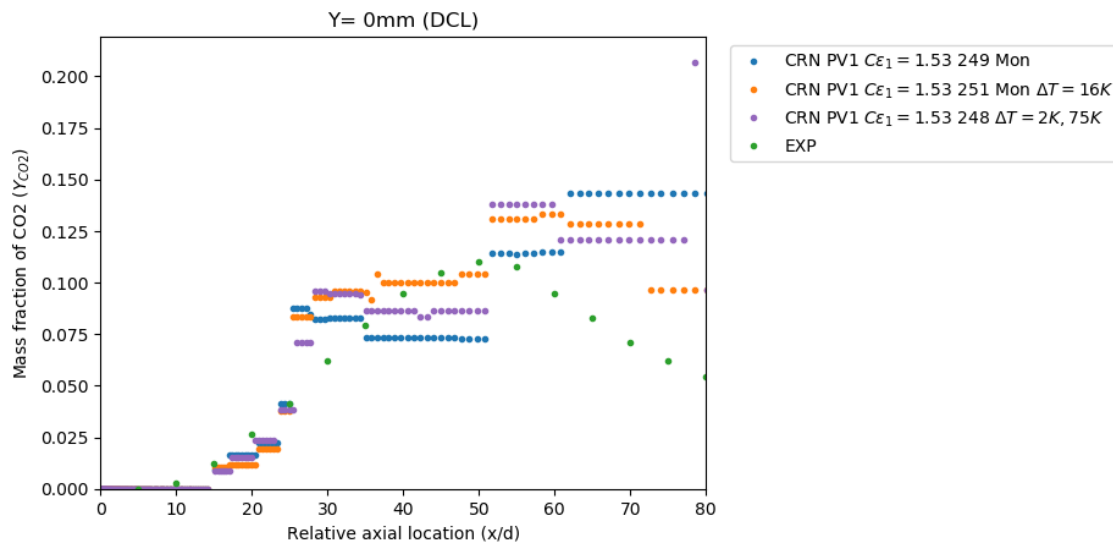


Figure 4.9: Experimental (●) and CFD-CRN predicted profiles of **Mass fraction of CO2** at the centreline **DCL** ($r/d_{jet} = 0$) for CRNs with **249** PSRs in the **original Monaghan clustering** (●), **251** PSRs in **Monaghan clustering with $\Delta T = 16K$ substituted for $\Delta T = 2K$** (●) and **248** PSRs in **Monaghan clustering with $\Delta T = 75K$ substituted for $\Delta T = 50K$** (●).

ZONING EFFECT

The Monaghan et al. method uses zoning and local tolerances. It would be interesting to know whether the improvement with respect to data fitting is only attributed to the discrete scaling of tolerances. Therefore the Monaghan et al. method was compared to a run case using the same zoning with a fixed tolerance and a run case using no zoning and a global fixed tolerance for all criteria.

Figure 4.10 to 4.13 provide some of the plots used to compare the three run cases mentioned. The run case that uses the Monaghan zoning with a fixed tolerance has a much larger number of reactors although the tolerance of 0.06 is double the tolerance of the run case without zoning.

The explanation for this is that the clustering is done through the BFS-method, which has one starting point and then looks at neighboring cells to determine whether they can be included in the cluster. This means the clustering is dependent on the starting point and the direction in which the BFS-method is searching. Zoning breaks up the domain, which makes the clustering even more dependent on the starting point and direction of searching.

It is possible that a CRN can be constructed with a tolerance of 0.03, that has a similar number of reactors as the run case without zoning, by trying other starting points or by clustering each zone separately and then combining the domain. For this part of the research, it was assumed that an effective tolerance below 0.06 was suitable for this comparison.

As a result of the larger amount of reactors, the reactor density and consequently the smoothness of the profile are higher for the run case with zoning and a fixed tolerance. This is clearly visible in Figure 4.10 and 4.11. Another thing that can be observed in both Figure 4.10 and 4.11 is that the two run cases being compared to the original Monaghan et al. method are relatively close together in terms of volume integral average and profile fitting.

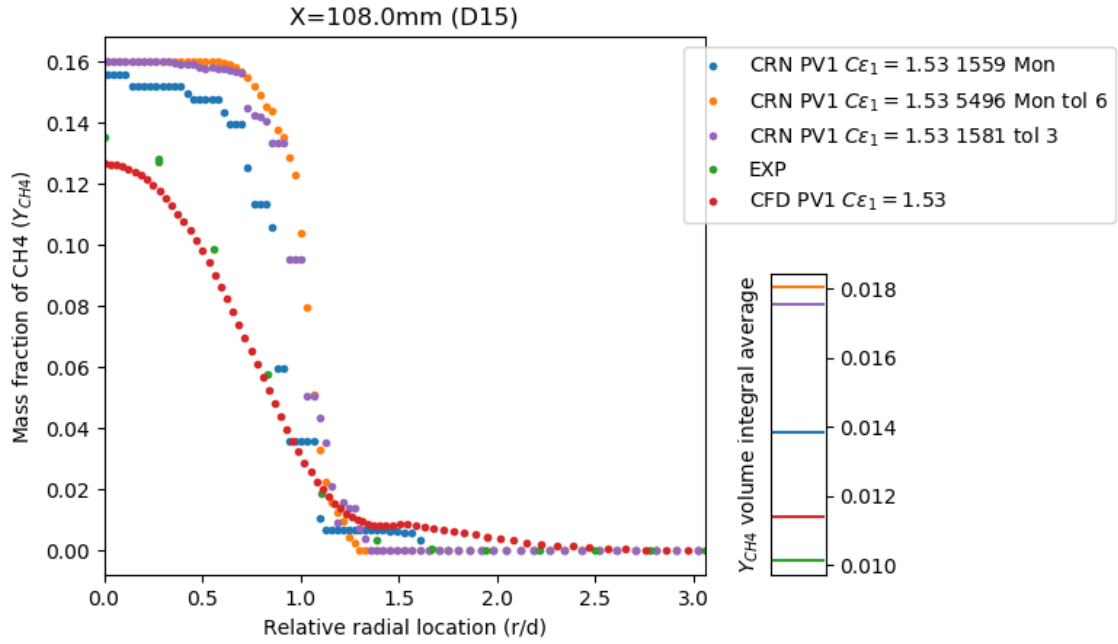


Figure 4.10: Experimental (\bullet), CFD PV1 $C\epsilon_1 = 1.53$ (\bullet) and CFD-CRN predicted profiles (left) and volume integral averages (right) of **Mass fraction of CH₄** in the radial direction at axial location **D15** ($x/d_{jet} = 15$) for CRNs with **1559** PSRs in the **original Monaghan clustering** (\bullet), **5496** PSRs in **Monaghan zoning with tolerance 0.06** (\bullet) and **1581** PSRs in **Temperature, Axial Coordinate and Mean Mixture Fraction clustering with tolerance 0.03** (\bullet).

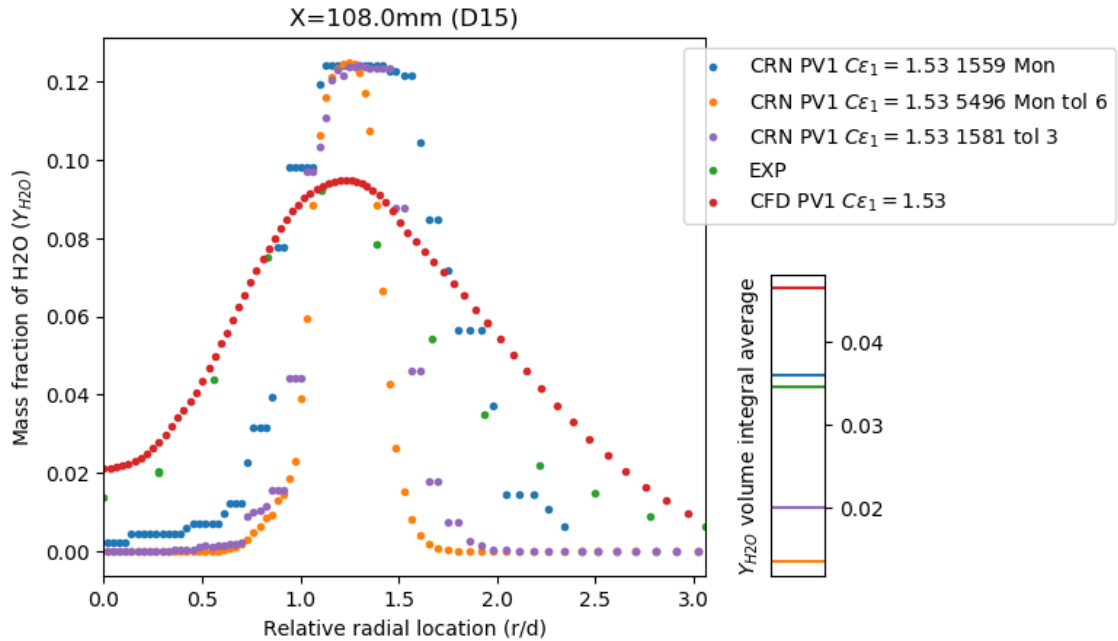


Figure 4.11: Experimental (\bullet), CFD PV1 $C\epsilon_1 = 1.53$ (\bullet) and CFD-CRN predicted profiles (left) and volume integral averages (right) of **Mass fraction of H₂O** in the radial direction at axial location **D15** ($x/d_{jet} = 15$) for CRNs with **1559** PSRs in the **original Monaghan clustering** (\bullet), **5496** PSRs in **Monaghan zoning with tolerance 0.06** (\bullet) and **1581** PSRs in **Temperature, Axial Coordinate and Mean Mixture Fraction clustering with tolerance 0.03** (\bullet).

Lastly, Figure 4.11 shows the pilot of the Sandia Flame D, which contains H₂O, is the least diffused for the zoned with fixed tolerance case and the most of the CRNs for the original Monaghan et al.

method. The same phenomena can also be seen in Figure 4.12 and 4.13, where the CH₄ from the jet remains higher and the peak from the pilot stays more pronounced, respectively.

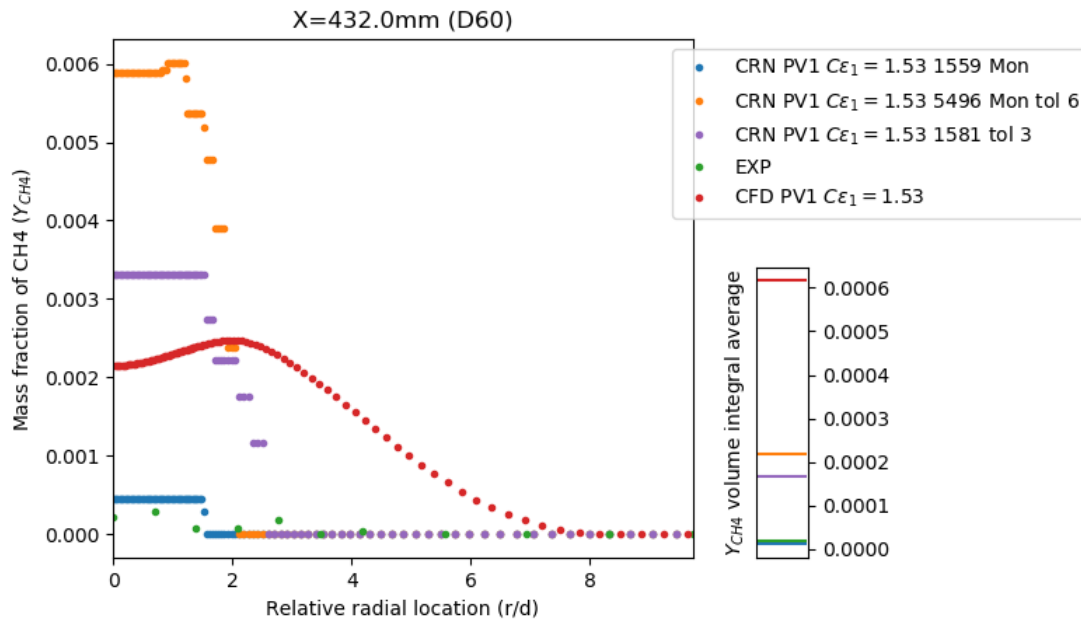


Figure 4.12: Experimental (●), CFD PV1 $C\epsilon_1 = 1.53$ (●) and CFD-CRN predicted profiles (left) and volume integral averages (right) of **Mass fraction of CH₄** in the radial direction at axial location **D60** ($x/d_{jet} = 60$) for CRNs with **1559** PSRs in the **original Monaghan clustering** (●), **5496** PSRs in **Monaghan zoning with tolerance 0.06** (●) and **1581** PSRs in **Temperature, Axial Coordinate and Mean Mixture Fraction clustering with tolerance 0.03** (●).

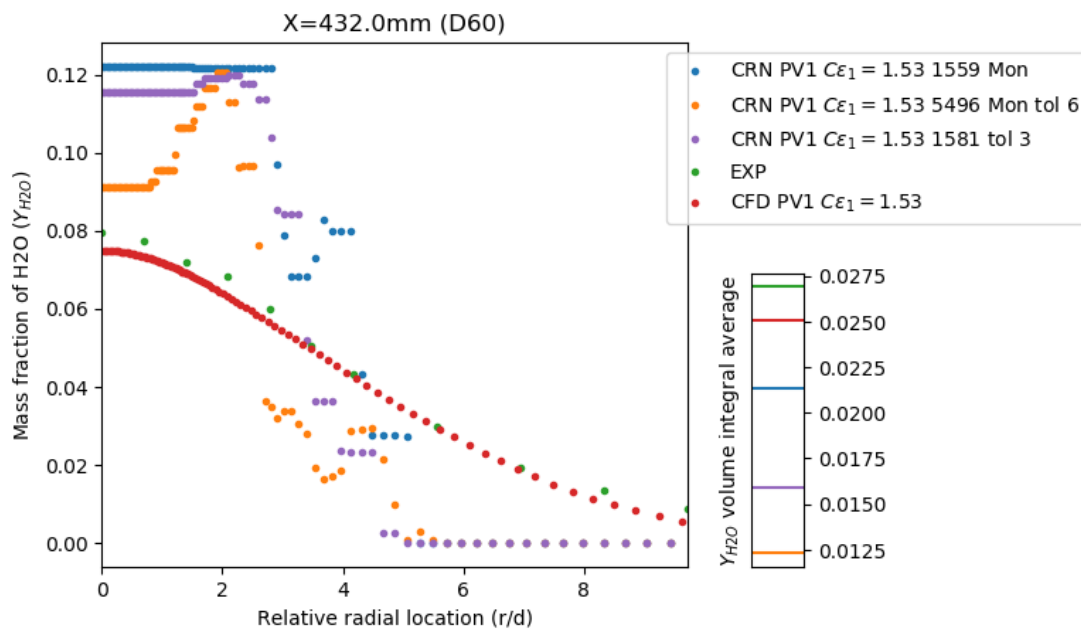


Figure 4.13: Experimental (●), CFD PV1 $C\epsilon_1 = 1.53$ (●) and CFD-CRN predicted profiles (left) and volume integral averages (right) of **Mass fraction of H₂O** in the radial direction at axial location **D60** ($x/d_{jet} = 60$) for CRNs with **1559** PSRs in the **original Monaghan clustering** (●), **5496** PSRs in **Monaghan zoning with tolerance 0.06** (●) and **1581** PSRs in **Temperature, Axial Coordinate and Mean Mixture Fraction clustering with tolerance 0.03** (●).

SCALED TOLERANCE EFFECT

Based on the results in Figure 4.10 to 4.13, it seems the zoning proposed by Monaghan et al. does not improve the data fitting by itself and actually increases the dependency of the clustering on the starting point and search direction using the BFS-method. Therefore it would be interesting to compare the discrete tolerance scaling achieved by the zoning with continuous tolerance scaling.

The continuous tolerance scaling used for this comparison uses a linear function to determine the local tolerance for each criteria in each cell to be clustered. Table 4.2 contains the tolerance ranges and functions used for each clustering criteria. The functions use normalized values (subscript n) of the clustering criteria to arrive at the tolerance. The functions used are based on the zoning and tolerances used by Monaghan et al.

Table 4.2: Scaling tolerance ranges and function for each clustering criteria.

Clustering Criteria	Symbol	Tolerance Range [\approx]	Tolerance Function
Temperature	T	2K-100K	$-0.059 \cdot T_n + 0.06$
X-Coordinate	x	0.01m-0.2m	$-0.29 \cdot f_n + 0.3$
Mean Mixture Fraction	f	0.01-1.0	$-0.99 \cdot f_n + 1$

To reduce complexity, the tolerance for temperature is only dependent on the temperature and not the mean mixture fraction. The tolerance for the x-coordinate is determined using the mean mixture fraction and the tolerance for mean mixture fraction, which is originally only used in the fuel rich zone, is dependent on mean mixture fraction and ranges from $\Delta f \approx 0.01$ to a large number, which was chosen to be 1.0.

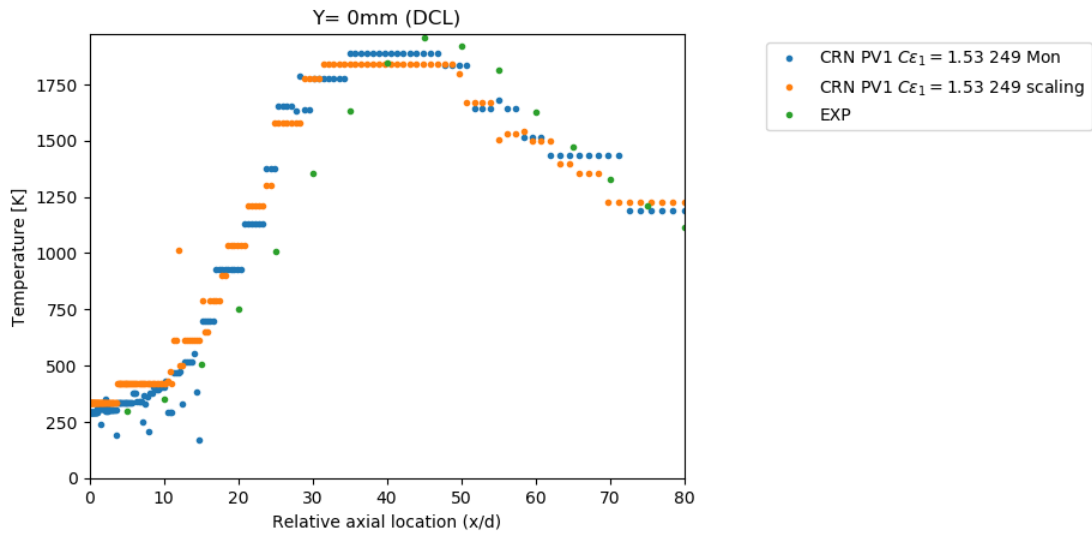


Figure 4.14: Experimental (\bullet) and CFD-CRN predicted profiles of **Static Temperature** at the centreline **DCL** ($r/d_{jet} = 0$) for CRNs with 249 PSRs in the **original Monaghan clustering** (\bullet) and 249 PSRs in **scaled tolerance clustering** (\bullet).

The scaled tolerances resulted in a CRN that has some differences in the distribution of reactors. When quantitatively tracing the reactor distribution, the region close to the inlet has fewer reactors both in the fuel rich zone near the jet and pilot and in the co-flow compared to the Monaghan et al. method. The co-flow region in general has more reactors with most in the mid to far field of the domain than the Monaghan et al. method. The scaled tolerance CRN has significantly more reactors in the far field and a similar amount in the mid field. However, there seems to be more variation in reactor density in the mid field.

These observations can in part be supported by Figure 4.14. The region close to the inlet ($x/d=0m-15m$) clearly has larger plateaus in the scaled tolerance results. In the region downstream of that ($x/d=15m-30m$), the size of the plateaus is similar, but then from $x/d=30m$ to $50m$ the region of the scaled tolerance at the centreline is represented by only one reactor.

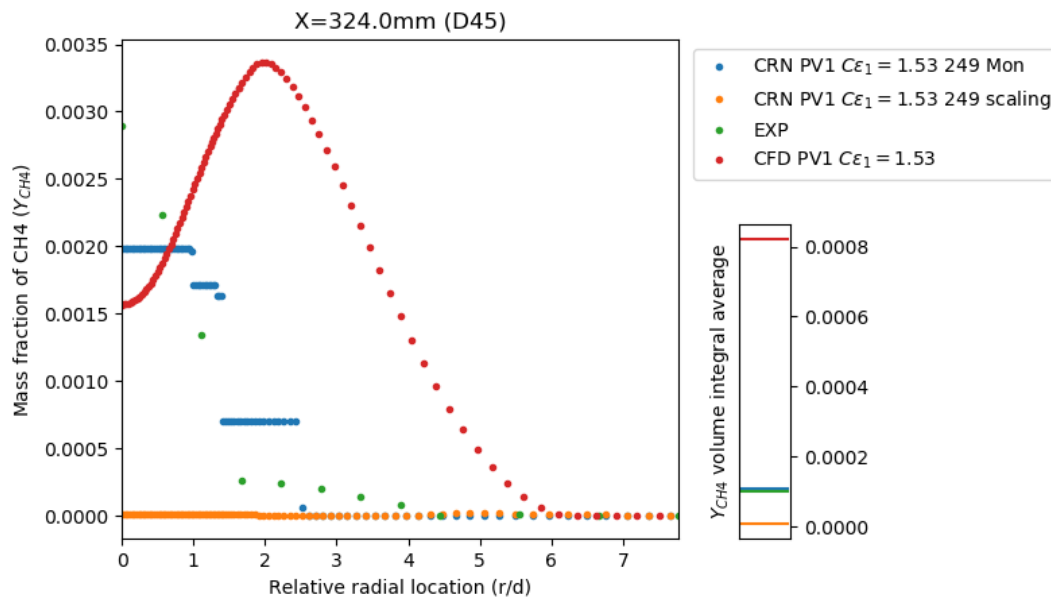


Figure 4.15: Experimental (\bullet), CFD PV1 $C\epsilon_1 = 1.53$ (\bullet) and CFD-CRN predicted profiles (left) and volume integral averages (right) of **Mass fraction of CH4** in the radial direction at axial location **D45** ($x/d_{jet} = 45$) for CRNs with **249** PSRs in the **original Monaghan clustering** (\bullet) and **249** PSRs in **scaled tolerance clustering** (\bullet).

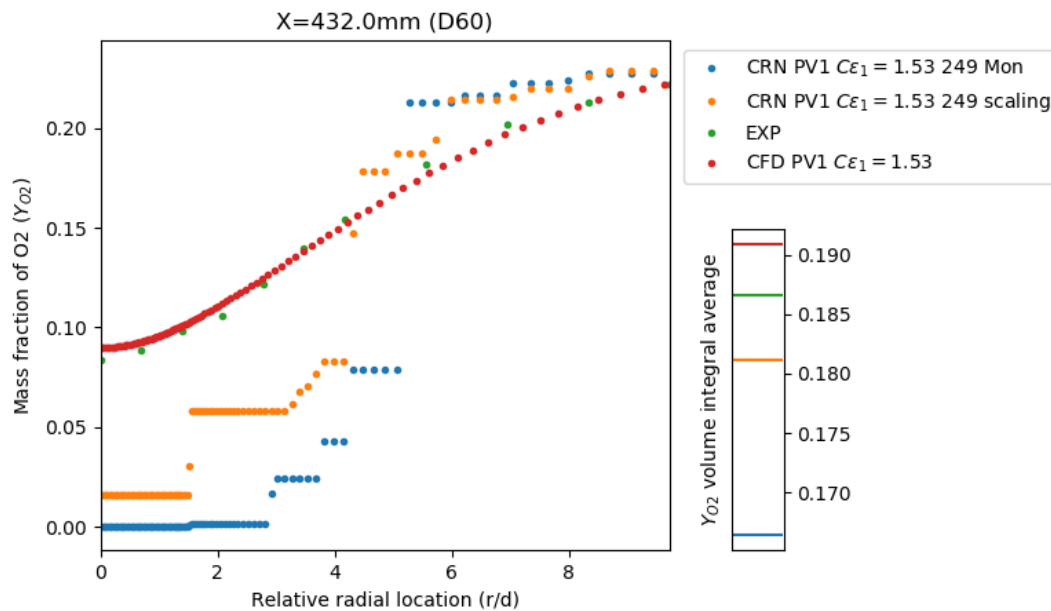


Figure 4.16: Experimental (\bullet), CFD PV1 $C\epsilon_1 = 1.53$ (\bullet) and CFD-CRN predicted profiles (left) and volume integral averages (right) of **Mass fraction of O2** in the radial direction at axial location **D60** ($x/d_{jet} = 60$) for CRNs with **249** PSRs in the **original Monaghan clustering** (\bullet) and **249** PSRs in **scaled tolerance clustering** (\bullet).

The differences in local reactor resolution lead to varying profile result fitting dependent on the species and location. For example, Figure 4.15 show that the scaled tolerance CRN resulted in a

relatively sudden drop of CH_4 , which could suggest that the higher temperature regions are not represented accurately. On the other hand, Figure 4.16 shows more accurate diffusion of O_2 which suggests a more suitable coverage for that purpose.

ZONED TOLERANCE CLUSTERING EFFECT ON A FLAMELESS COMBUSTION TEST CASE

The zoned tolerance clustering method of Monaghan et al. was specifically designed for the Sandia Flame D on which it was effective. It would be interesting to know whether the same clustering method would have a similar effect on a test case, like the Verissimo et al. test case, which is in another flame regime and has recirculation in the flow field. Therefore, in this section, the results generated with the constant tolerance clustering method previously adopted for the Verissimo et al. test case [39] are compared to those of the Monaghan et al. method.

Figure 4.17 and 4.18 are contour plots of static temperature that are based on the same temperature distribution that was output by CFD. The only difference between these figures is formed by the clustering. Figure 4.17 and 4.18 have a similar number of reactors, but due to the clustering method the contours look different. The Monaghan et al. method yields a reactor distribution with less reactors in the region near the wall (above 0.02m) and downstream in the burner (past 0.1m) compared to the constant tolerance clustering. Furthermore, the Monaghan et al. method seems to have some L-shaped clusters near the inlet (left).

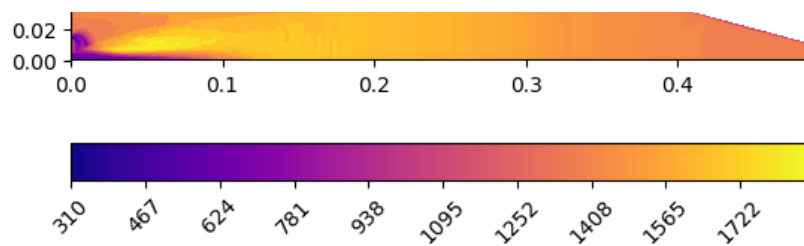


Figure 4.17: CFD-CRN predicted parallel contour of **Static Temperature** [K] for a CRN with **3137** PSRs in the **constant tolerance clustering**.

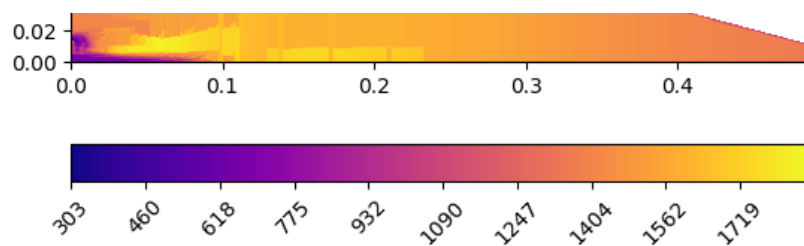


Figure 4.18: CFD-CRN predicted parallel contour of **Static Temperature** [K] for a CRN with **3210** PSRs in the **Monaghan clustering**.

The reduced reactor presence downstream of 0.1m in the burner generated by the Monaghan et al. method is clearly visible in Figure 4.19 and 4.20. The Monaghan clustering with 3210 PSRs yields almost a straight line, because almost the entire width of the burner is represented by only one reactor, whilst the constant tolerance clustering still has a clear profile that better resembles the experimental data.

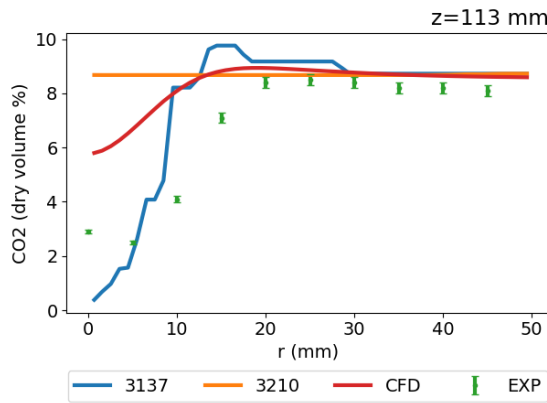


Figure 4.19: Experimental (●), CFD (●) and CFD-CRN predicted profiles of **Mass fraction of CO₂** in the radial direction at axial location **113** ($z = 113\text{mm}$) for CRNs with **3137** PSRs in the **constant tolerance clustering** (●) and **3210** PSRs in **Monaghan clustering** (●).

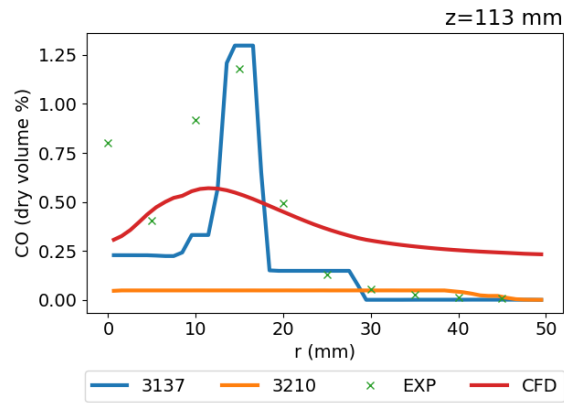


Figure 4.20: Experimental (●), CFD (●) and CFD-CRN predicted profiles of **Mass fraction of CO** in the radial direction at axial location **113** ($z = 113\text{mm}$) for CRNs with **3137** PSRs in the **constant tolerance clustering** (●) and **3210** PSRs in **Monaghan clustering** (●).

The more even distribution of reactors in the network generated by the constant tolerance method in general causes a better curve fitting to the experimental data compared to the Monaghan et al method. However, at the axial location closest to the outlet, the results for the major species of both method are almost completely overlapping.

Regarding the minor species, both the mass fraction of CO and NO_x are not overlapping. Figure 4.21 shows that the simulation results using the Monaghan et al. method underpredict CO more than using the constant tolerance method with respect to the experimental data.

Figure 4.22 shows that the complete opposite is true for the prediction of NO_x. Comparing Figure 4.21 and Figure 4.22, the relative prediction improvement is larger in case of NO_x. This shows, that eventhough the Monaghan et al. method was not specifically designed for the Verissimo et al. test case, the method can have a positive effect on the prediction of NO_x without decreasing the accuracy of the CO prediction too much. Whether having lower tolerances in e.g. high temperature regions always has this effect is still speculative.

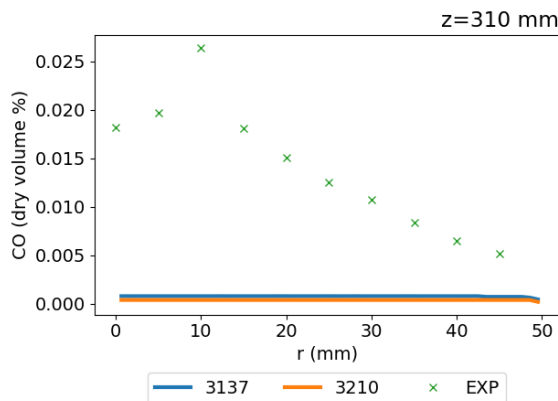


Figure 4.21: Experimental (●), CFD (●) and CFD-CRN predicted profiles of **Mass fraction of CO** in the radial direction at axial location **310** ($z = 310\text{mm}$) for CRNs with **3137** PSRs in the **constant tolerance clustering** (●) and **3210** PSRs in **Monaghan clustering** (●).

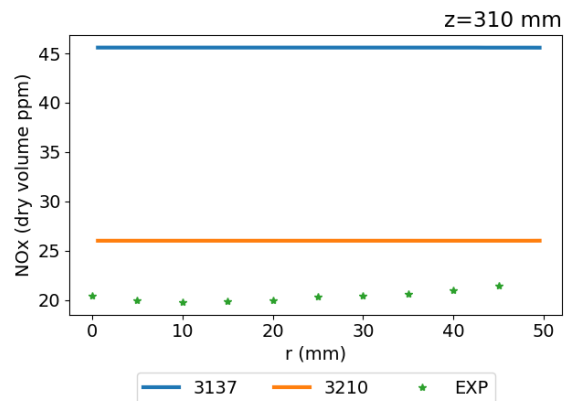


Figure 4.22: Experimental (●) and CFD-CRN predicted profiles of **Mass fraction of NO_x** in the radial direction at axial location **310** ($z = 310\text{mm}$) for CRNs with **3137** PSRs in the **constant tolerance clustering** (●) and **3210** PSRs in **Monaghan clustering** (●).

4.3. GRID INDEPENDENCE STUDY SFD

To determine if the domain is accurately represented by the CRN, a grid independence study was conducted for the Sandia Flame D (SFD). This was not necessary for the Verissimo et al. test case as this was already done for the results replicated. Such a study entails increasing the number of reactors until the results generated by the run case converge, which signifies the results becoming independent of the resolution of the CRN. Preferably, the grid independent results are also closer to the experimental results in terms of fit and quantities compared to results from smaller grids.

The grid independence study was performed using the Monaghan et al. clustering method for both CFD cases of the Sandia Flame D that are further detailed in Appendix A. Figure 4.23 to 4.25 show the profile plots of O_2 , CO and NO resulting from the CFD case with PV1 and $C\epsilon_1 = 1.53$ at the most downstream axial location available in the experimental results. Figure 4.26 to 4.28 show the same for the CFD case with PV2 and $C\epsilon_1 = 1.60$.

Figure 4.23 shows that even though the number gap between 249 and 493 PSRs is smaller than between 493 and 1035 PSRs, the volume integral average and profiles are significantly closer together. Furthermore, the average value of the larger number of reactors is closer to the experimental results in this plot. It should be noted that the difference in integral is only present in the plotted range, since the outflow of oxygen (O) is conserved.

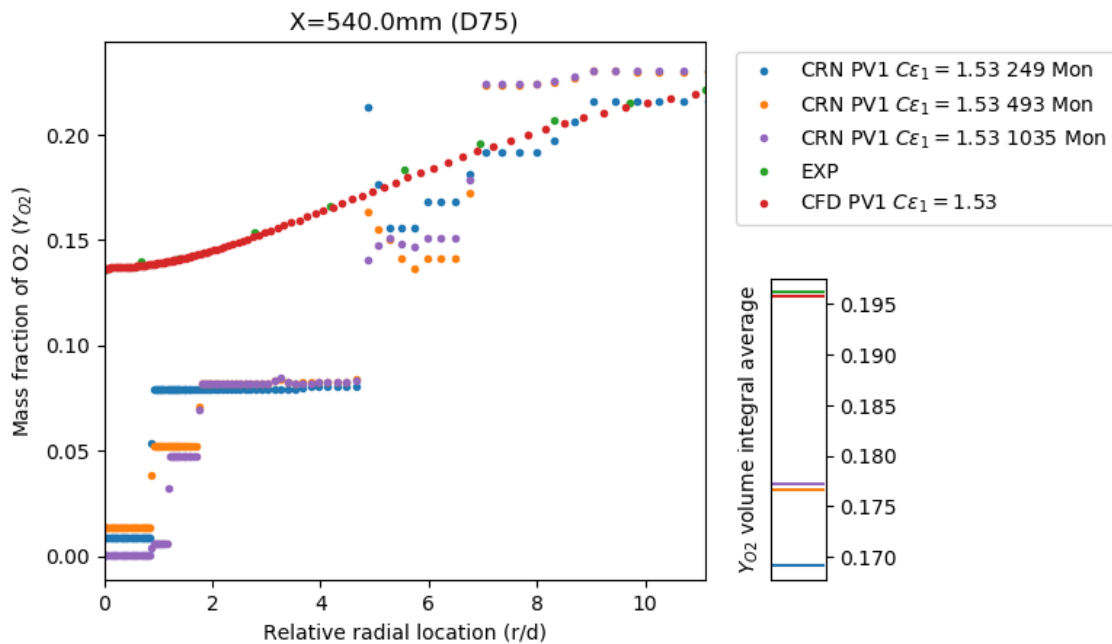


Figure 4.23: Experimental (\bullet), CFD PV1 $C\epsilon_1 = 1.53$ (\bullet) and CFD-CRN predicted profiles (left) and volume integral averages (right) of **Mass fraction of O_2** in the radial direction at axial location **D75** ($x/d_{jet} = 75$) for CRNs with **249** (\bullet), **493** (\bullet) and **1035** (\bullet) PSRs in the **original Monaghan clustering**.

In Figure 4.24, the volume integral averages again show the 493 and 1035 case are closer together and the larger the number the closer the results are to the value obtained from the experimental results. The profile with 1035 PSRs shows a peak near the center, which is not present or at least not so exaggeratedly present in the 249 and 493 cases. However, the region going outward from $r/d_{jet} = 2$ shows a very similar profile in the 1035 and 493 cases.

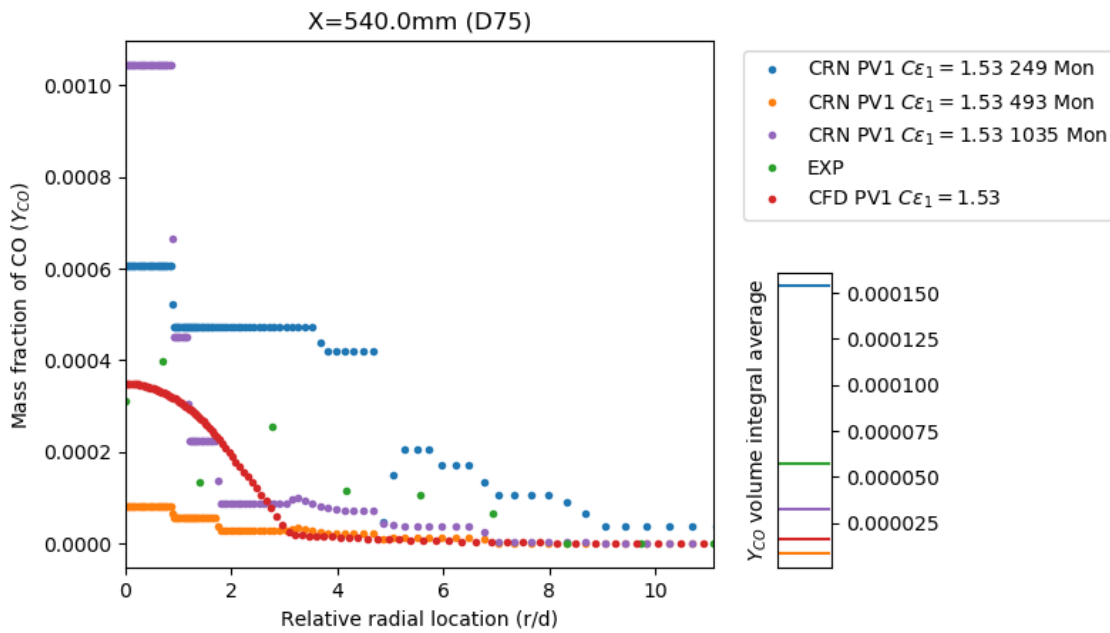


Figure 4.24: Experimental (●), CFD PV1 $C\epsilon_1 = 1.53$ (●) and CFD-CRN predicted profiles (left) and volume integral averages (right) of **Mass fraction of CO** in the radial direction at axial location **D75** ($x/d_{jet} = 75$) for CRNs with **249** (●), **493** (●) and **1035** (●) PSRs in the **original Monaghan clustering**.

Regarding the mass fraction of NO in Figure 4.25, the volume integral averages of 1035 and 493 are again closer together and the part of the profile that is in view of the experimental results in the plot are relatively more similar as well. The 249 case is closer to the experimental results in this case, but all CRN results are closer than those of the CFD, which is significantly more overpredicted.

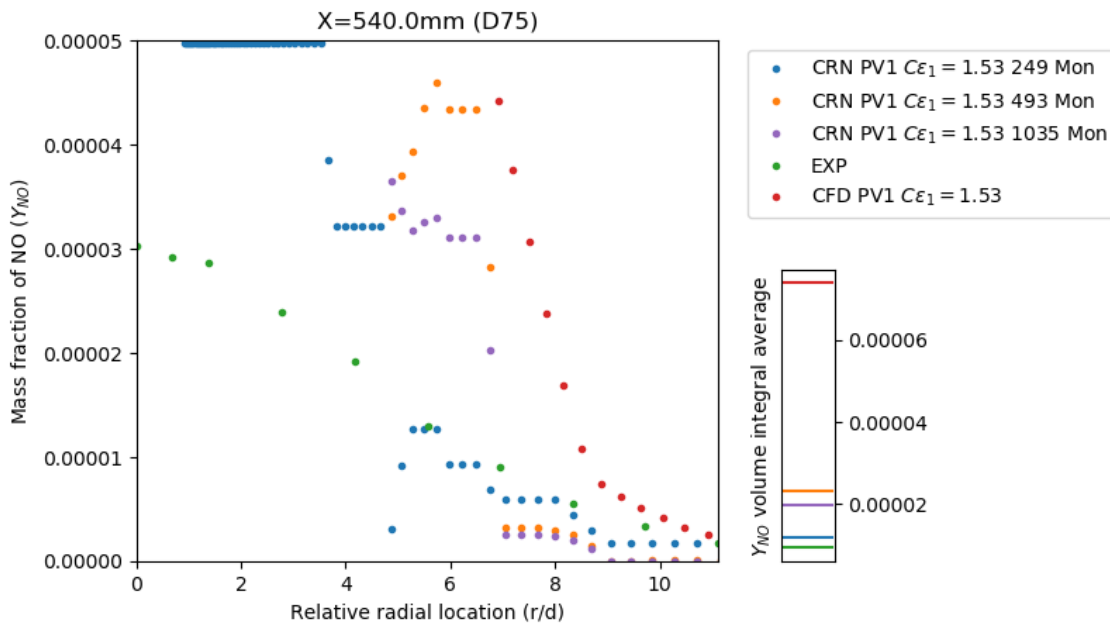


Figure 4.25: Experimental (●), CFD PV1 $C\epsilon_1 = 1.53$ (●) and CFD-CRN predicted profiles (left) and volume integral averages (right) of **Mass fraction of NO** in the radial direction at axial location **D75** ($x/d_{jet} = 75$) for CRNs with **249** (●), **493** (●) and **1035** (●) PSRs in the **original Monaghan clustering**.

In Figure 4.26 similar results to Figure 4.23 can be observed, but the results of 590 and 1006 are even

closer together in the profile and the volume integral averages are relatively closer to the experimental results.

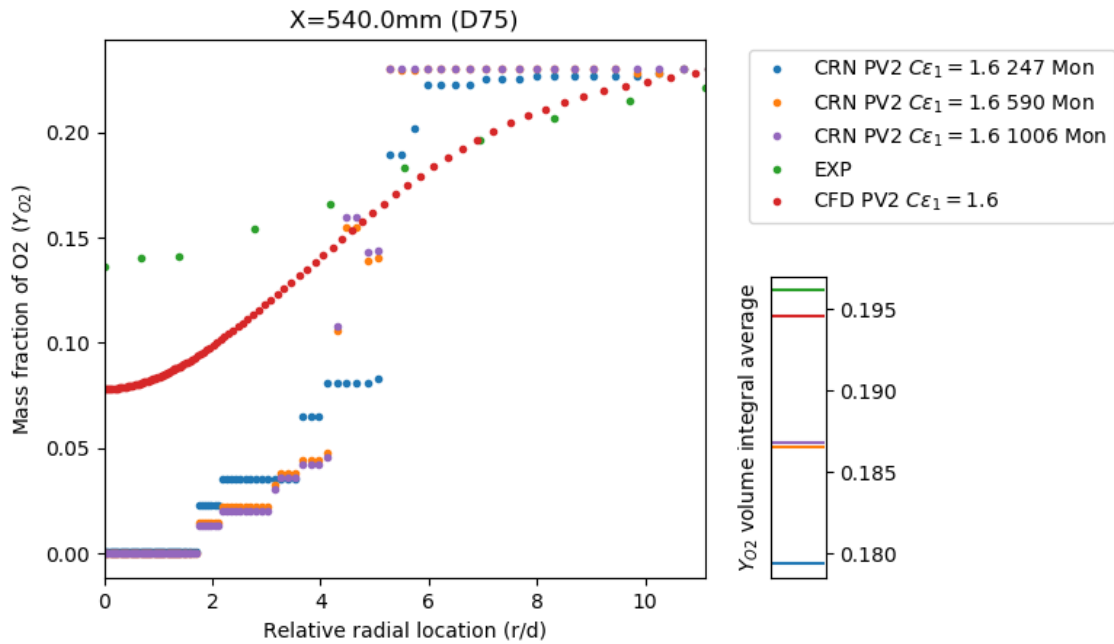


Figure 4.26: Experimental (\bullet), CFD PV2 $C\epsilon_1 = 1.60$ (\bullet) and CFD-CRN predicted profiles (left) and volume integral averages (right) of **Mass fraction of O₂** in the radial direction at axial location **D75** ($x/d_{jet} = 75$) for CRNs with **249** (\bullet), **493** (\bullet) and **1035** (\bullet) PSRs in the **original Monaghan clustering**.

The 590 and 1006 cases are again closer together in the profiles and averages of Figure 4.27, but the predictions get further away from the experimental results with increasing number of PSRs.

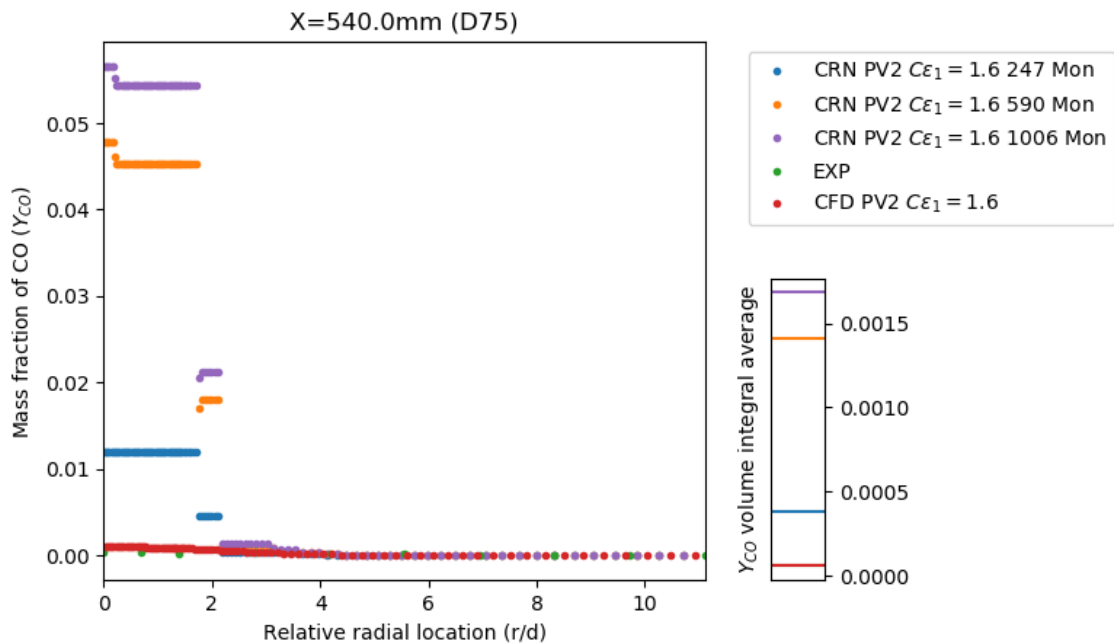


Figure 4.27: Experimental (\bullet), CFD PV2 $C\epsilon_1 = 1.60$ (\bullet) and CFD-CRN predicted profiles (left) and volume integral averages (right) of **Mass fraction of CO** in the radial direction at axial location **D75** ($x/d_{jet} = 75$) for CRNs with **249** (\bullet), **493** (\bullet) and **1035** (\bullet) PSRs in the **original Monaghan clustering**.

Finally, Figure 4.28 shows all volume integral averages of the CRNs are close together and close to the experimental results relative to the overprediction of the CFD. Consulting the profiles the results from the 590 and 1006 cases are almost fully overlapping in this plot.

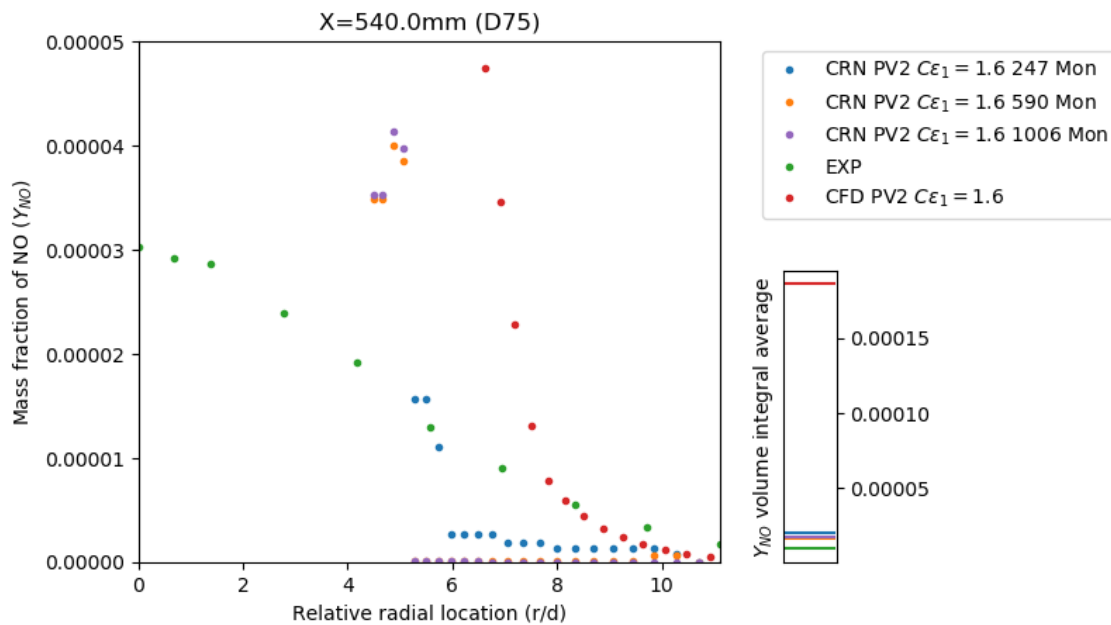


Figure 4.28: Experimental (●), CFD PV2 $C\epsilon_1 = 1.60$ (●) and CFD-CRN predicted profiles (left) and volume integral averages (right) of **Mass fraction of NO** in the radial direction at axial location **D75** ($x/d_{jet} = 75$) for CRNs with **249** (●), **493** (●) and **1035** (●) PSRs in the **original Monaghan clustering**.

4.4. COMPARISON CFD AND CRN

One of the main reasons for using the CFD-CRN method for emission prediction is, that in general compared to only using CFD, it is believed to provide more accurate quantity prediction regarding minor species in particular. Therefore the results from the AGNES are not only compared to the experimental results for the test cases, but also to the respective CFD results that serve as the starting point for the CRN.

SANDIA FLAME D

Figure 4.29 is a contour plot of the static temperature generated by CFD with the settings PV1 and $C\epsilon_1 = 1.53$. Figure 4.30 is the same plot output by AGNES. When the energy equation is not used, the temperature is kept fixed when solving the CRN. Therefore the only difference between Figure 4.29 and 4.30 is the discretization of the domain. The CRN in this case only has 1006 reactors as opposed to 24278 cells in the CFD. Therefore the stepsize and contour shape may differ, which is most evident in the far field.

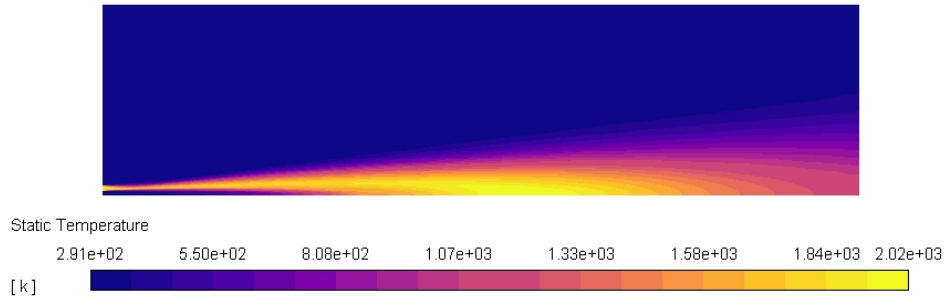


Figure 4.29: CFD PV2 $C_{\epsilon_1} = 1.6$ predicted parallel contour of **Static Temperature**.

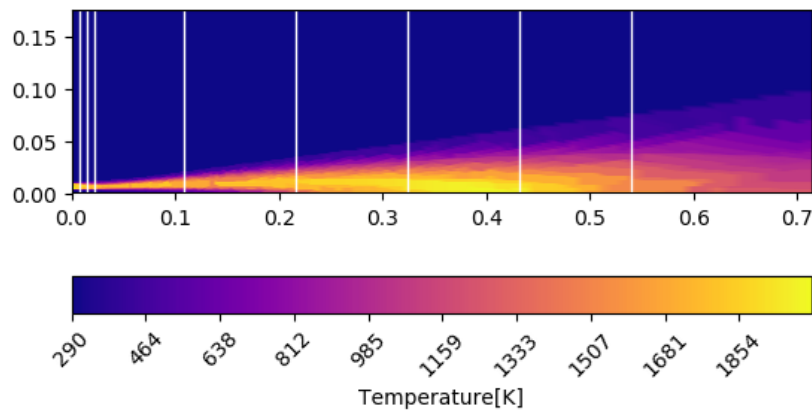


Figure 4.30: CFD-CRN predicted parallel contour of **Static Temperature** in for a CRN with **1006 PSRs** in the **Monaghan clustering** based on CFD PV2 $C_{\epsilon_1} = 1.6$. (The white lines show the axial location of the radial experimental data.)

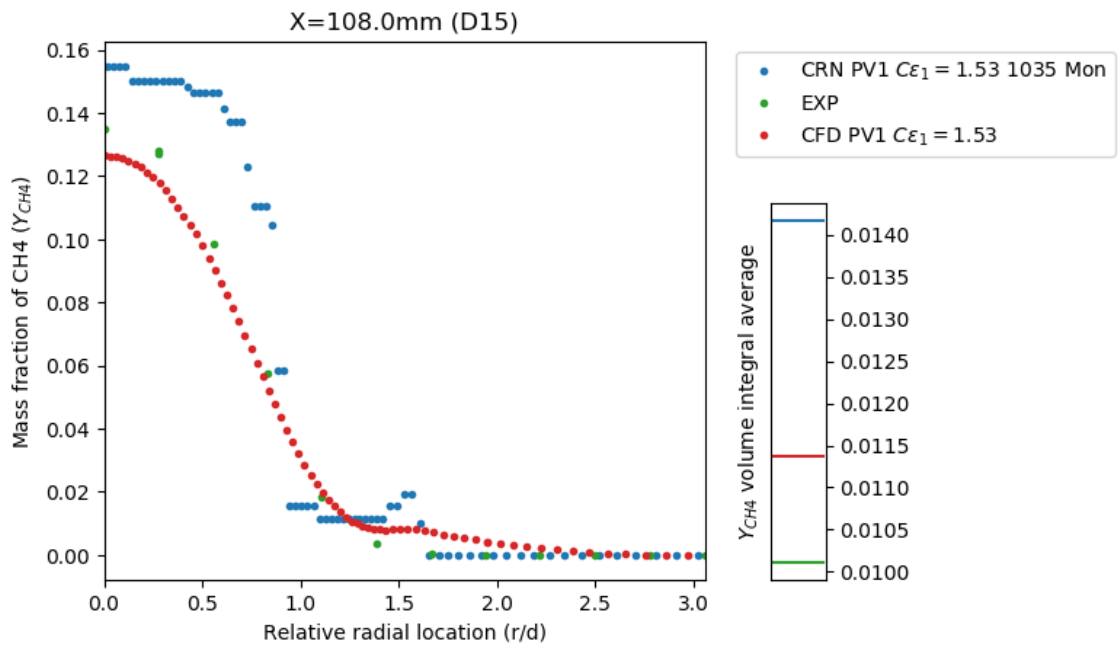


Figure 4.31: Experimental (●), CFD PV1 $C_{\epsilon_1} = 1.53$ (●) and CFD-CRN predicted profiles (left) and volume integral averages (right) of **Mass fraction of CH₄** in the radial direction at axial location **D15** ($x/d_{jet} = 15$) for a CRN with **1035 PSRs** in the **Monaghan clustering** (●).

The mass fraction of CH_4 was predicted better by CFD below $x/d=45$ in both cases. The main reason for that seems to be that the centre of the jet is not reacting as much, which is shown in Figure 4.31. This could mean there is a lack of oxygen for CH_4 to react, which in turn could indicate diffusion is not taking place fast enough in spite of the turbulent diffusion added.

Further downstream the roles reverse and the CFD prediction of the mass fraction of CH_4 does not decrease enough, whilst the CRN in both cases is much closer to the experimental results. An example of this is Figure 4.32.

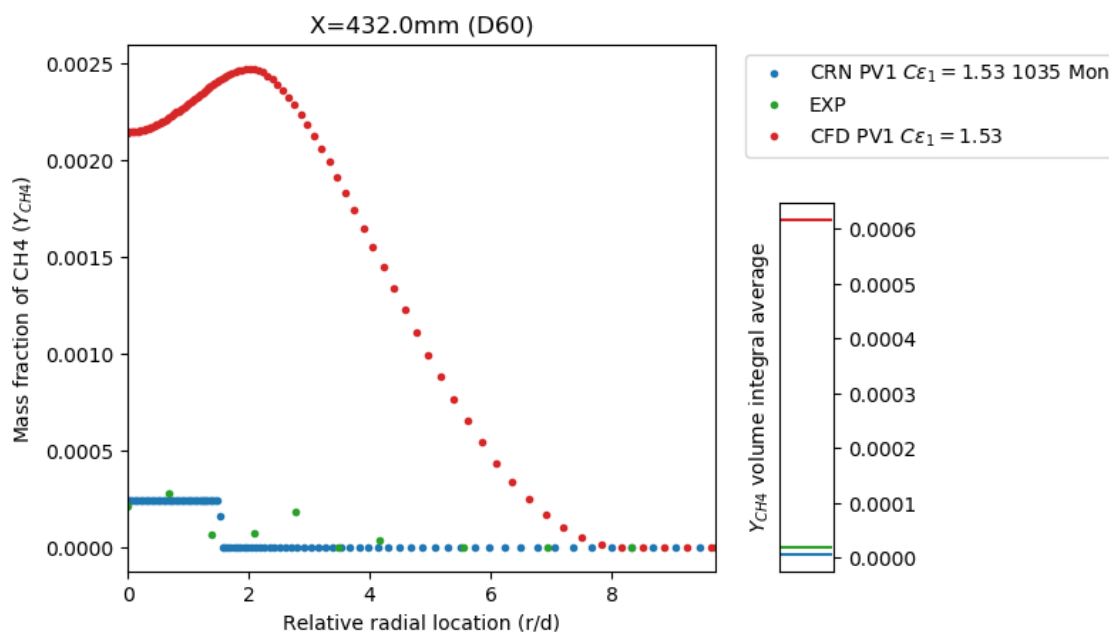


Figure 4.32: Experimental (\bullet), CFD PV1 $C\epsilon_1 = 1.53$ (\bullet) and CFD-CRN predicted profiles (left) and volume integral averages (right) of **Mass fraction of CH_4** in the radial direction at axial location **D60** ($x/d_{jet} = 60$) for a CRN with **1035** PSRs in the **Monaghan clustering** (\bullet).

In case of the mass fraction of CO , the opposite takes place w.r.t. CH_4 . Near the inlet the CFD is overpredicting the amount of CO and in both cases the CRN is closer to the experimental results, which is shown by Figure 4.33. However, around $x/d=45$ the mass fraction of CH_4 predicted by both CRNs starts increasing leading to a significant overprediction w.r.t. the CFD and experimental results downstream.

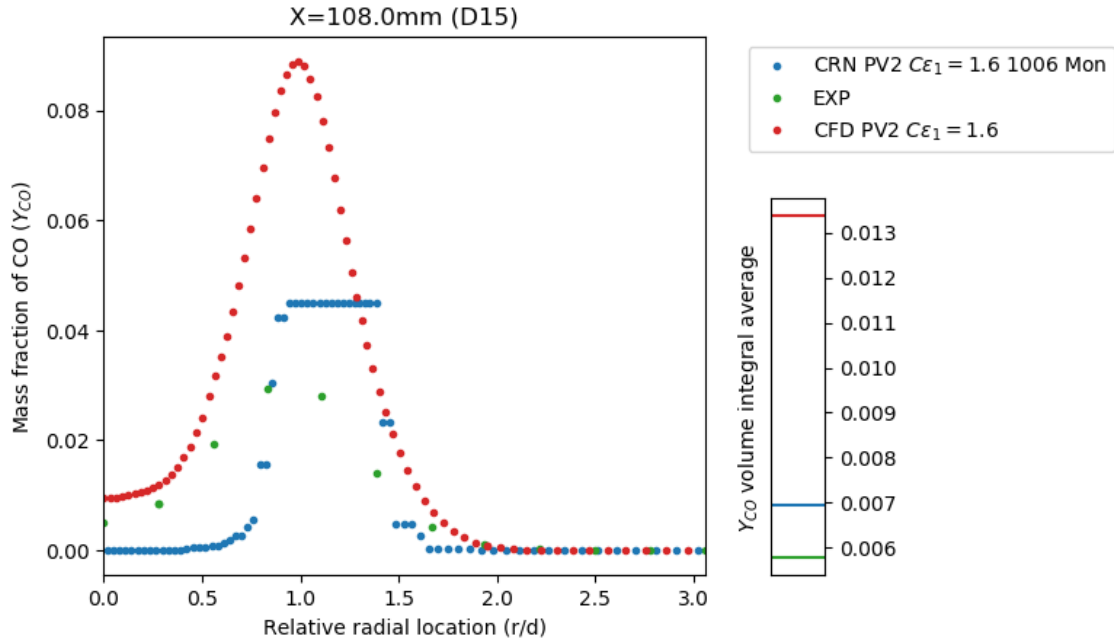


Figure 4.33: Experimental (\bullet), CFD PV2 $C\epsilon_1 = 1.6$ (\bullet) and CFD-CRN predicted profiles (left) and volume integral averages (right) of **Mass fraction of CO** in the radial direction at axial location **D15** ($x/d_{jet} = 15$) for a CRN with **1006** PSRs in the **Monaghan clustering** (\bullet).

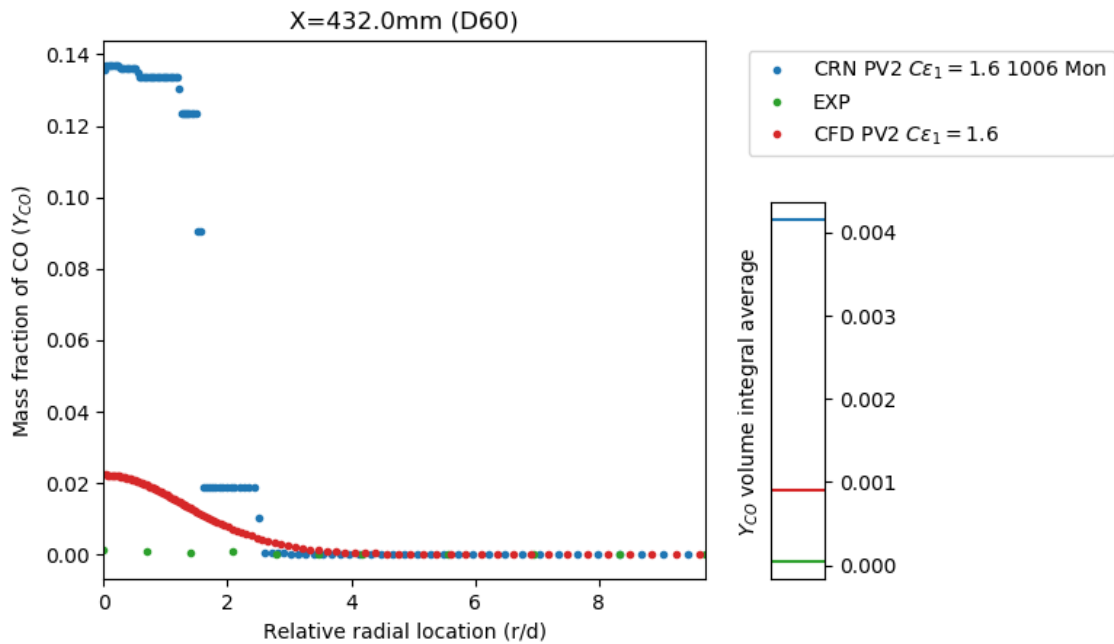


Figure 4.34: Experimental (\bullet), CFD PV2 $C\epsilon_1 = 1.6$ (\bullet) and CFD-CRN predicted profiles (left) and volume integral averages (right) of **Mass fraction of CO** in the radial direction at axial location **D60** ($x/d_{jet} = 60$) for a CRN with **1006** PSRs in the **Monaghan clustering** (\bullet).

Even though the prediction by AGNES for CO is not more accurate than the CFD prediction, this is not the case for NO, which is also a minor species. Both CFD run cases overpredict the amount of NO and both CRNs provide a significantly better prediction in terms of profile and volume integral average throughout the entire domain. Figure 4.35 is an example of that.

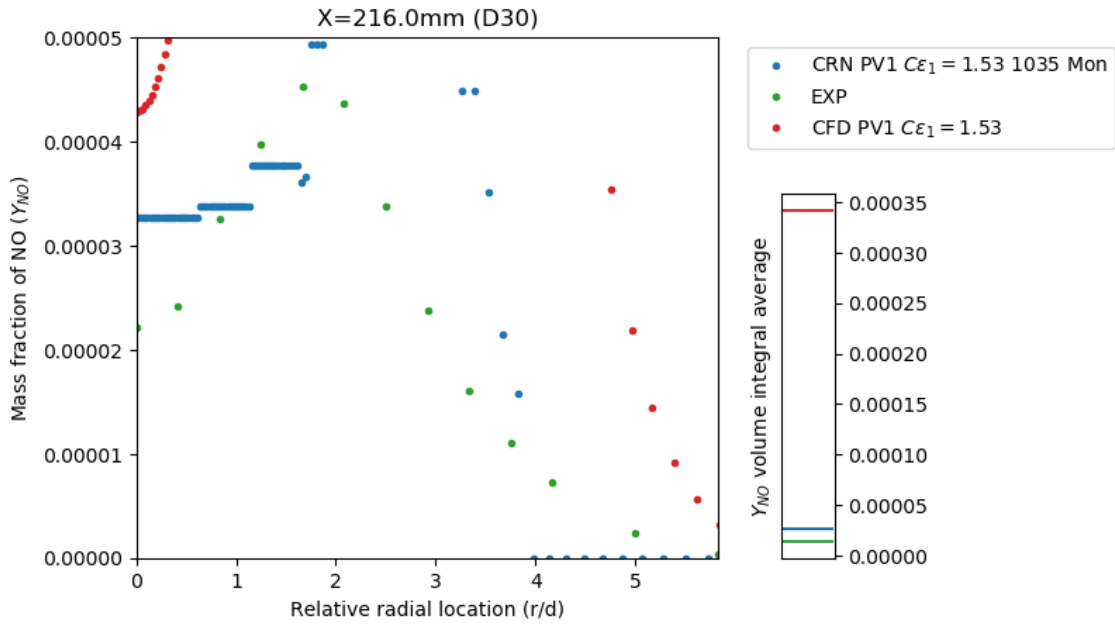


Figure 4.35: Experimental (●), CFD PV1 $C\epsilon_1 = 1.53$ (●) and CFD-CRN predicted profiles (left) and volume integral averages (right) of **Mass fraction of CH4** in the radial direction at axial location **D30** ($x/d_{jet} = 30$) for a CRN with **1035** PSRs in the **Monaghan clustering** (●).

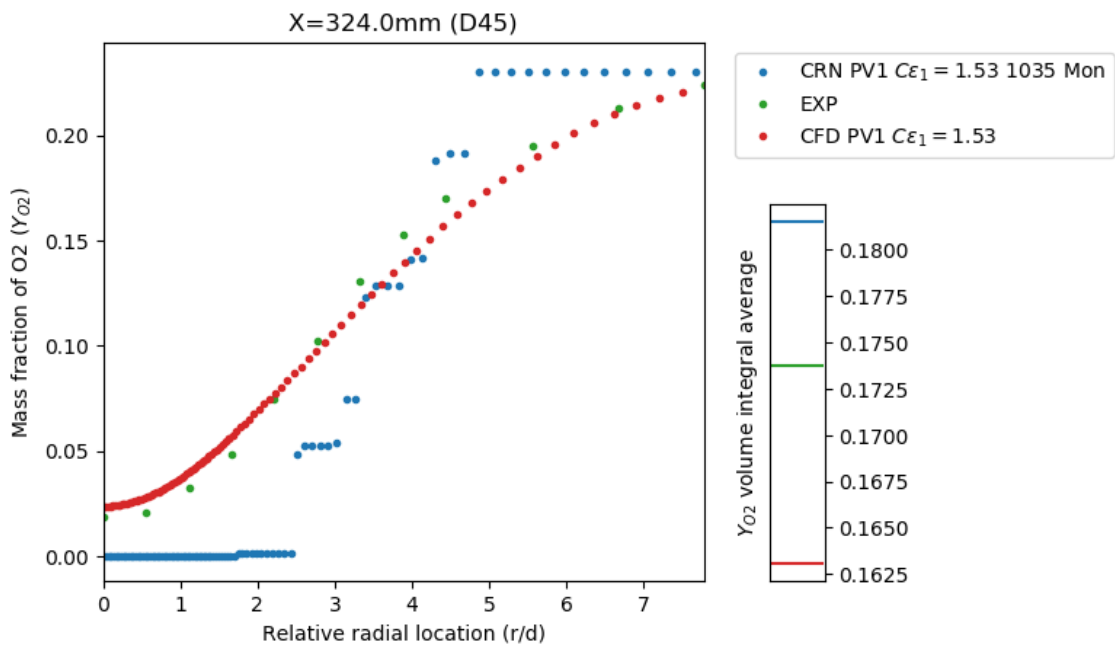


Figure 4.36: Experimental (●), CFD PV1 $C\epsilon_1 = 1.53$ (●) and CFD-CRN predicted profiles (left) and volume integral averages (right) of **Mass fraction of O2** in the radial direction at axial location **D45** ($x/d_{jet} = 45$) for a CRN with **1035** PSRs in the **Monaghan clustering** (●).

Finally, the volume integral averages vary regarding the major species. In some cases the CRNs are closer to the experimental average and sometimes the CFD run cases have a better average. One thing that is clearly visible in the profiles is that the CRNs are not as smooth as the CFD and experimental results. This phenomena is illustrated by Figure 4.36 and could again indicate a lack of diffusion, in spite of the turbulent diffusion added.

When the turbulent diffusion was multiplied with a constant factor to test its sensitivity, it was found that the steep drops were still present and only the extreme values became less extreme. In case of Figure 4.36, the mass fraction of O_2 near the center-line moved up and the sloped section moved slightly towards the center, which does not benefit the smoothness or the volume integral average in this case.

VERISSIMO ET AL. TEST CASE

Figure 4.37 shows the static temperature contour in the plane parallel to the axial direction over one of the burner fuel injectors. Figure 4.38 is based on these CFD results and therefore only the discretization of the results is altered. The CFD uses 2310062 cells to represent the burner volume, whilst the CRN in Figure 4.38 represents the same domain with 3137 reactors. This leads to a less smooth contour.

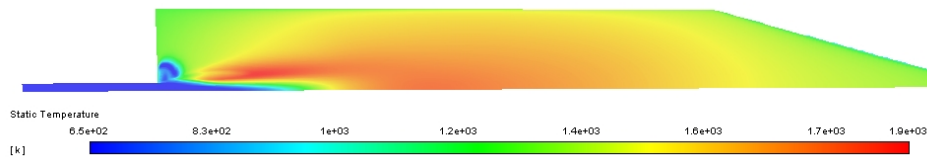


Figure 4.37: CFD predicted parallel contour of **Static Temperature** [K]

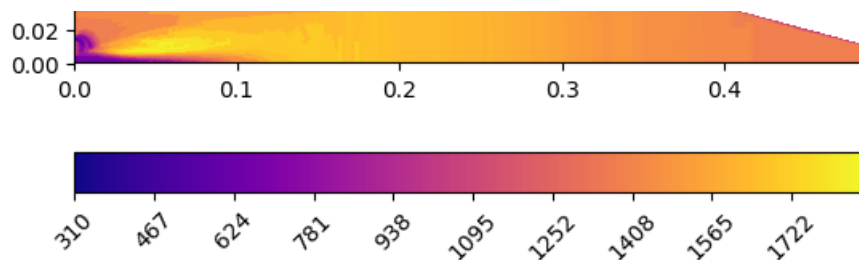


Figure 4.38: CFD-CRN predicted parallel contour of **Static Temperature** [K] for a CRN with **3137** PSRs in the **constant tolerance clustering**.

When looking at Figure 4.39 and 4.40, the difference in data point resolution is evident. The CRNs in Figure 4.39 are solved without updating the temperature, which means that if there was no difference in data point resolution the lines would all overlap exactly. However, the CRN results show clear discretized steps as opposed to the smoothness of the CFD results.

In Figure 4.40, the lines should not necessarily overlap, but the difference in resolution at this axial location is again visible. This difference, however, does not mean the CFD results always have a better curve fit, when both are compared to the experimental results. It can be argued, that the CRN represented by the blue line in Figure 4.40 has a better fit due to the peak being closer to the peak in the experimental results compared to CFD.

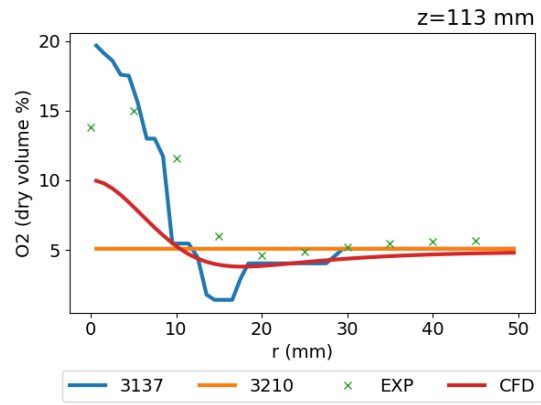
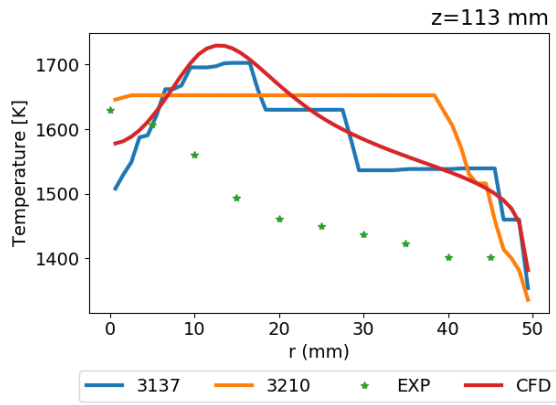


Figure 4.39: Experimental (•), CFD (•) and CFD-CRN predicted profiles of **Static Temperature** [K] in the radial direction at axial location **113** ($z = 113\text{mm}$) for CRNs with **3137** PSRs in the **constant tolerance clustering** (•) and **3210** PSRs in **Monaghan clustering** (•).

Figure 4.40: Experimental (•), CFD (•) and CFD-CRN predicted profiles of **Mass fraction of O2** in the radial direction at axial location **133** ($z = 133\text{mm}$) for CRNs with **3137** PSRs in the **constant tolerance clustering** (•) and **3210** PSRs in **Monaghan clustering** (•).

In the end, arguably the most interesting prediction region is near the exhaust, because that is where the prediction error is largest due to accumulation of error upstream and this is where emissions exit the system, which is what matters on a regulatory level. It was found in this case, that CFD overestimated the amount of CO and that AGNES was significantly better at predicting the mass fraction of CO, as shown by Figure 4.41.

For the mass fraction of NOx at the same axial location, the experimental data provides an average value of around 20.4 ppm. CFD underpredicts the amount of NOx here with only 0.15 ppm. The result of the Monaghan et al. clustered CRN with 3210 reactors slightly overpredicts the value with 26.0 ppm. The constant tolerance clustered CRN overshoots further with 45.6 ppm, which is a larger absolute distance from the experimental results than the CFD results.

CFD is better at predicting the mass fraction of CO₂, which is slightly more overpredicted by AGNES. Relative to the prediction error of CFD regarding the mass fractions of CO and NOx, the error generated by AGNES for CO₂ is significantly smaller. This is visible in Figure 4.42.

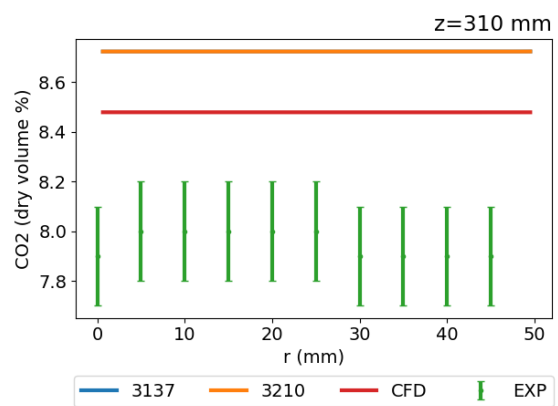
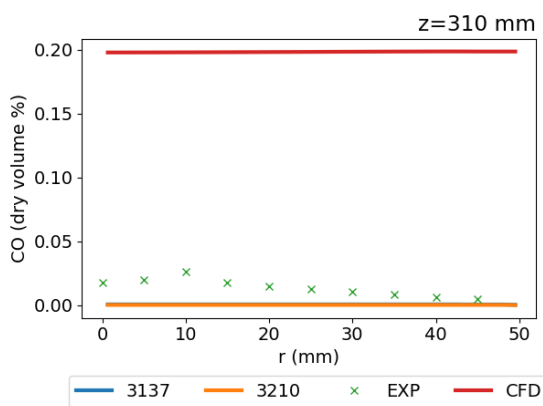


Figure 4.41: Experimental (•), CFD (•) and CFD-CRN predicted profiles of **Mass fraction of CO** in the radial direction at axial location **310** ($z = 310\text{mm}$) for CRNs with **3137** PSRs in the **constant tolerance clustering** (•) and **3210** PSRs in **Monaghan clustering** (•).

Figure 4.42: Experimental (•), CFD (•) and CFD-CRN predicted profiles of **Mass fraction of CO2** in the radial direction at axial location **310** ($z = 310\text{mm}$) for CRNs with **3137** PSRs in the **constant tolerance clustering** (•) and **3210** PSRs in **Monaghan clustering** (•).

4.5. EFFECT OF ENERGY EQUATION

The main subject of this research is to determine the effect of updating the temperature using the energy equation in stead of keeping the temperature fixed to the value determined by CFD. The results of that comparison are described in this section for the Sandia Flame D and the Verissimo et al. test case.

SANDIA FLAME D

The CFD results underpredicted the temperature near the pilot of the Sandia Flame D. It can be seen in Figure 4.43, that the run case that uses the energy equation is closer to the experimental results near the inlet.

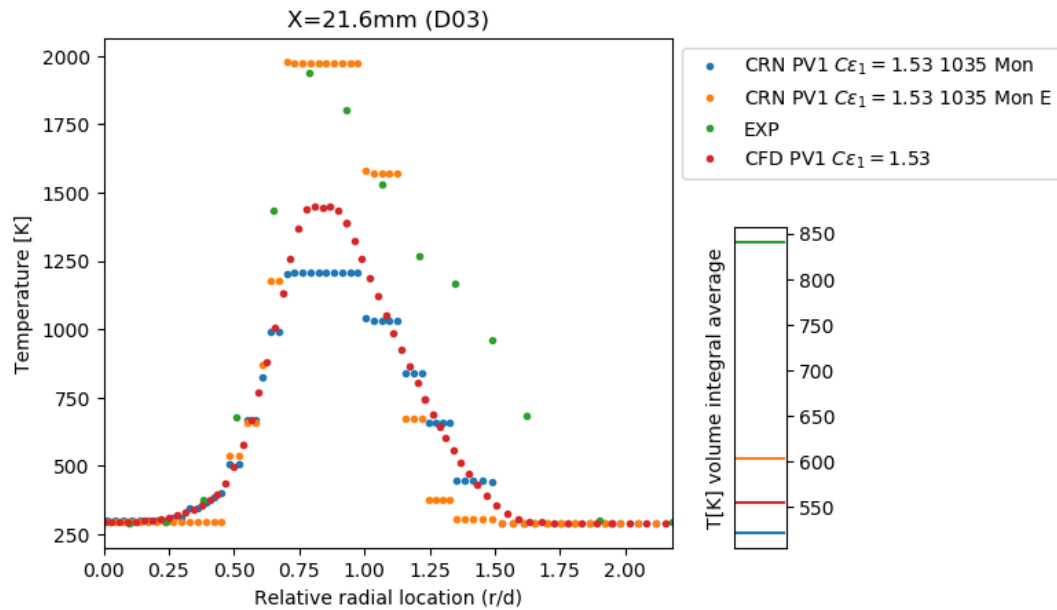


Figure 4.43: Experimental (\bullet), CFD PV1 $C\epsilon_1 = 1.53$ (\bullet) and CFD-CRN predicted profiles (left) and volume integral averages (right) of **Static Temperature** in the radial direction at axial location **D03** ($x/d_{jet} = 3$) for CRNs with **1035** PSRs in the Monaghan clustering **without** (\bullet) and **with updating temperature** (\bullet).

However, the temperature predicted by the energy equation run case keeps increasing, which leads to a large overprediction in the far field, as is shown in Figure 4.44. Figure 4.45 provides a more complete overview of the situation. Compared to Figure 4.46, which shows the temperature contour that was kept constant, the contour in Figure 4.45 is not as smooth. The relatively large areas with constant temperature suggest that no reactions are taking place in these regions. This is supported by the species mass fractions that, for example, do not show any significant change between 0.216 ($x/d_{jet} = 30$) and 0.324 ($x/d_{jet} = 45$) on the centreline. A limitation of the CRN is that advective heat transfer is modeled, but the diffusive heat transfer is not accounted for by the mass flow between reactors. CFD, on the other hand, does model diffusive heat transfer.

The increase of the maximum temperature, which is shown by the increased range of the contour level scales in Figure 4.45 compared to Figure 4.46, can potentially be explained by the fact that the current version of AGNES does not account for heat loss through radiation and conduction. Radiation is modeled in CFD with the Discrete Ordinates model and conduction is solved using the energy equation.

Furthermore, the flame zone in Figure 4.45 is more stretched out and the high temperature center

is moved further downstream, which explains the large overprediction seen in Figure 4.44.

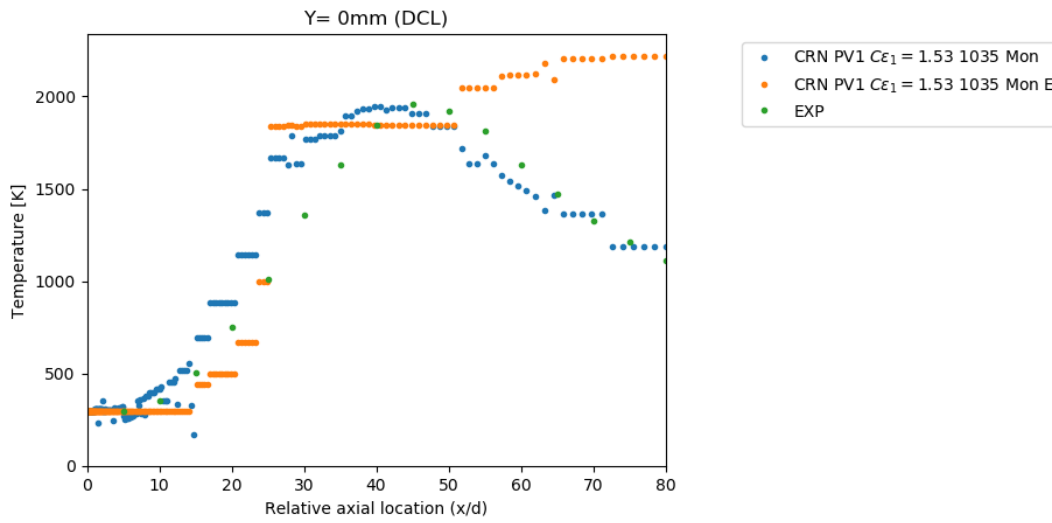


Figure 4.44: Experimental (●) and CFD-CRN predicted profiles of **Static Temperature** at the centreline **DCL** ($r/d_{jet} = 0$) for CRNs with **1035** PSRs in the Monaghan clustering **without** (●) and **with updating temperature** (●).

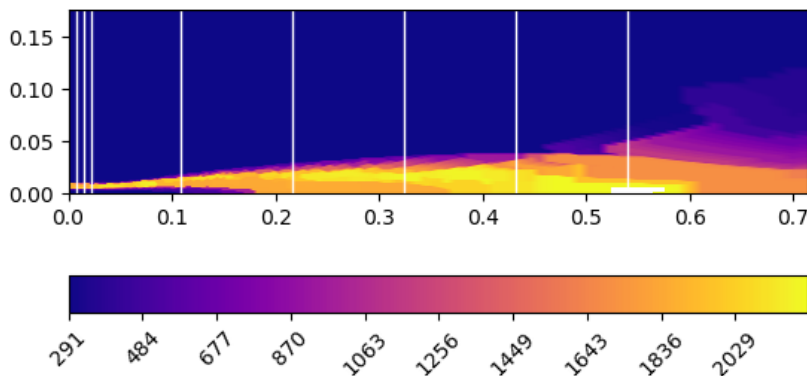


Figure 4.45: CFD-CRN predicted parallel contour of **Static Temperature** [K] for a CRN with **1035** PSRs in the **Monaghan clustering** based on CFD PV1 $C_{\epsilon_1} = 1.53$ **using the energy equation**.*

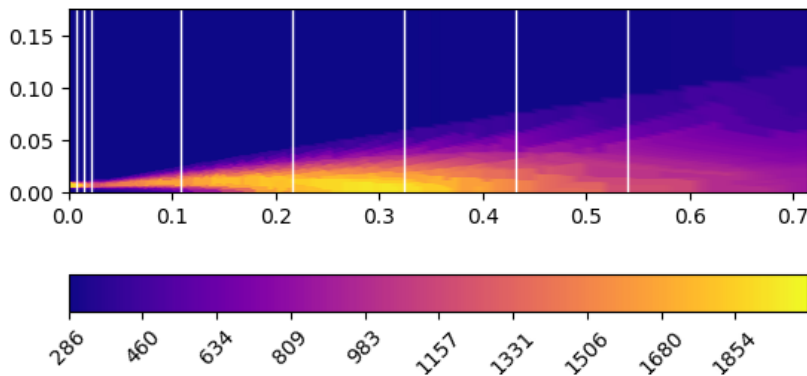


Figure 4.46: CFD-CRN predicted parallel contour of **Static Temperature** [K] for a CRN with **1035** PSRs in the **Monaghan clustering** based on CFD PV1 $C_{\epsilon_1} = 1.53$ **not using the energy equation**.*

* The white lines show the axial location of the radial experimental data.

The downstream movement can be explained by the increased temperature. The change in temperature caused a change in density, as shown in Figure 4.47 w.r.t. Figure 4.48. The density decreased in the flame zone and increased in the co-flow. The volume of each PSR in the CRN is kept constant, which means the change in density has a direct effect on the mass in each PSR. Since the mass flows between PSRs in the CRN are also kept constant, the relative amount of exchange between reactors increases in regions where the density decreases. The relative increased exchange in the flame zone could cause the stretching seen in Figure 4.45.

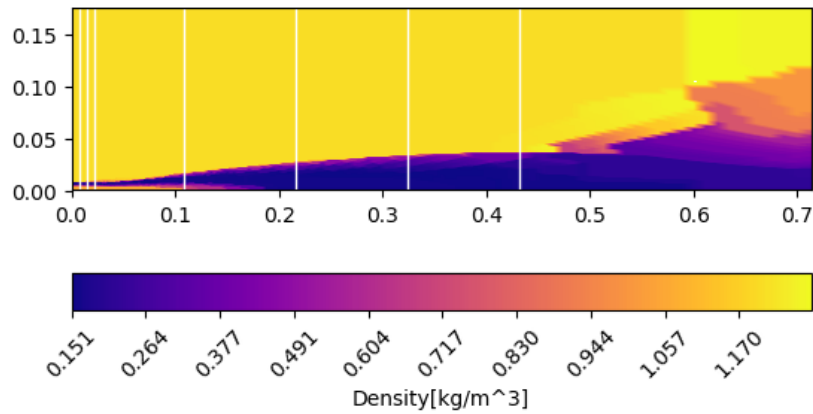


Figure 4.47: CFD-CRN predicted parallel contour of **Density** for a CRN with 1035 PSRs in the **Monaghan clustering** based on CFD PV1 $C_{e1} = 1.53$ **using the energy equation**.*

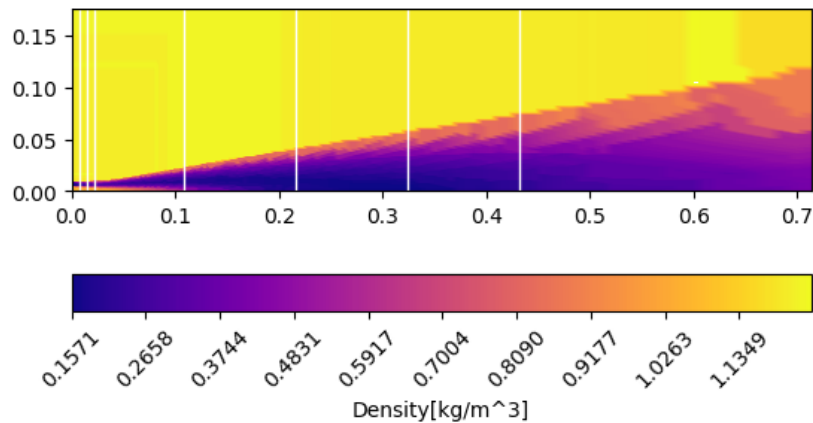


Figure 4.48: CFD-CRN predicted parallel contour of **Density** for a CRN with 1035 PSRs in the **Monaghan clustering** based on CFD PV1 $C_{e1} = 1.53$ **not using the energy equation**.*

The temperature has a clear effect on the prediction of NO. Comparing Figure 4.44 and 4.49, it is visible that the overprediction of temperature and mass fraction of NO start at the same axial location of $x/d=50$. Furthermore, in both plots, the difference between the energy equation run case and the experimental results starts increasing more and more progressing downstream.

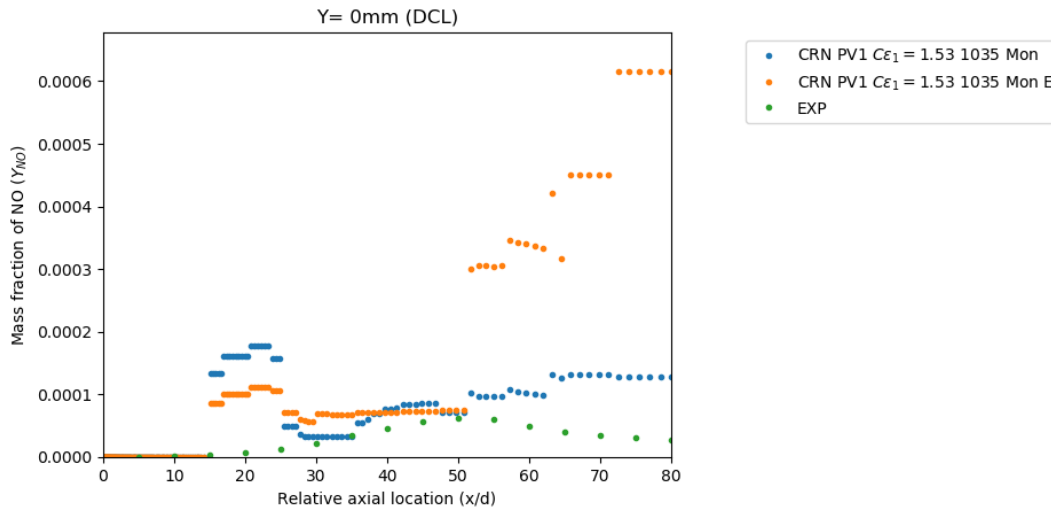


Figure 4.49: Experimental (●) and CFD-CRN predicted profiles of **Mass fraction of NO** at the centreline **DCL** ($r/d_{jet} = 0$) for CRNs with **1035** PSRs in the Monaghan clustering **without** (●) and **with updating temperature** (●).

Similar to the prediction of temperature the mass fraction of CO is more accurate near the pilot, which is shown in Figure 4.50. Unfortunately, similar to the temperature as well, the mass fraction of CO is overpredicted in the far field, which can be seen in Figure 4.51.

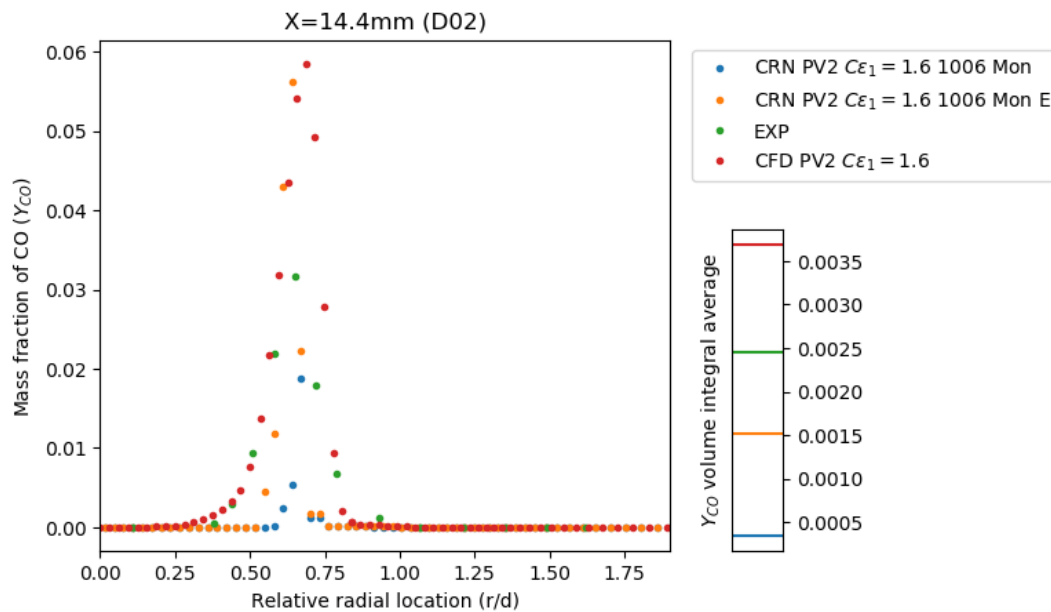


Figure 4.50: Experimental (●), CFD PV2 $C\epsilon_1 = 1.6$ (●) and CFD-CRN predicted profiles (left) and volume integral averages (right) of **Mass fraction of CO** in the radial direction at axial location **D02** ($x/d_{jet} = 2$) for CRNs with **1006** PSRs in the Monaghan clustering **without** (●) and **with updating temperature** (●).

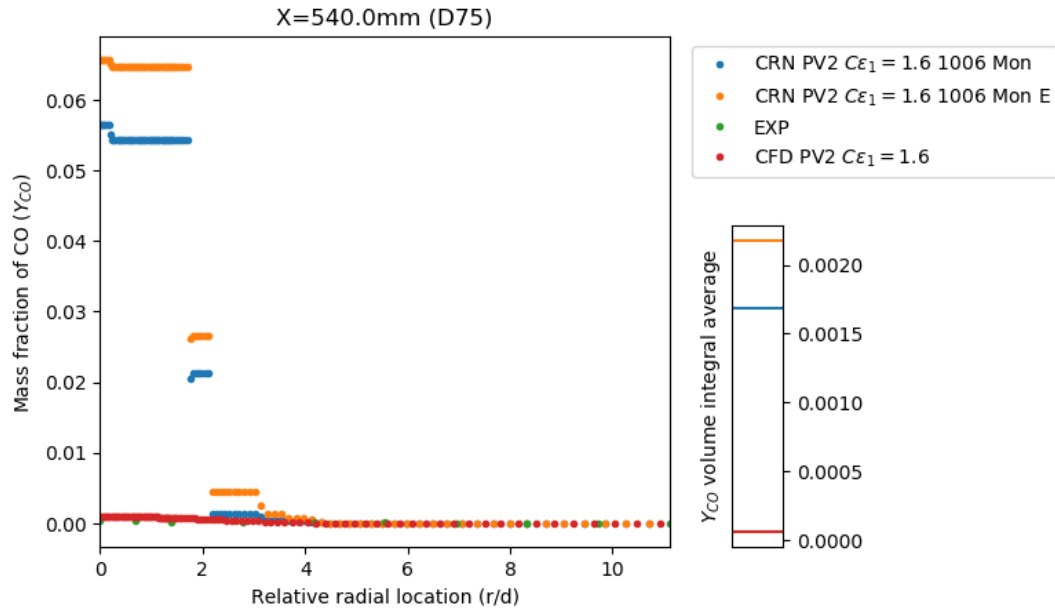


Figure 4.51: Experimental (\bullet), CFD PV2 $C\epsilon_1 = 1.6$ (\bullet) and CFD-CRN predicted profiles (left) and volume integral averages (right) of **Mass fraction of CO** in the radial direction at axial location **D75** ($x/d_{jet} = 75$) for CRNs with **1006** PSRs in the Monaghan clustering **without** (\bullet) and **with updating temperature** (\bullet).

The mass fraction of CH_4 has a different behaviour. Near the inlet the run cases are very similar, but past $x/d=30$ the energy equation run case starts to overpredict until $x/d=70$ where the prediction suddenly drops below the experimental results.

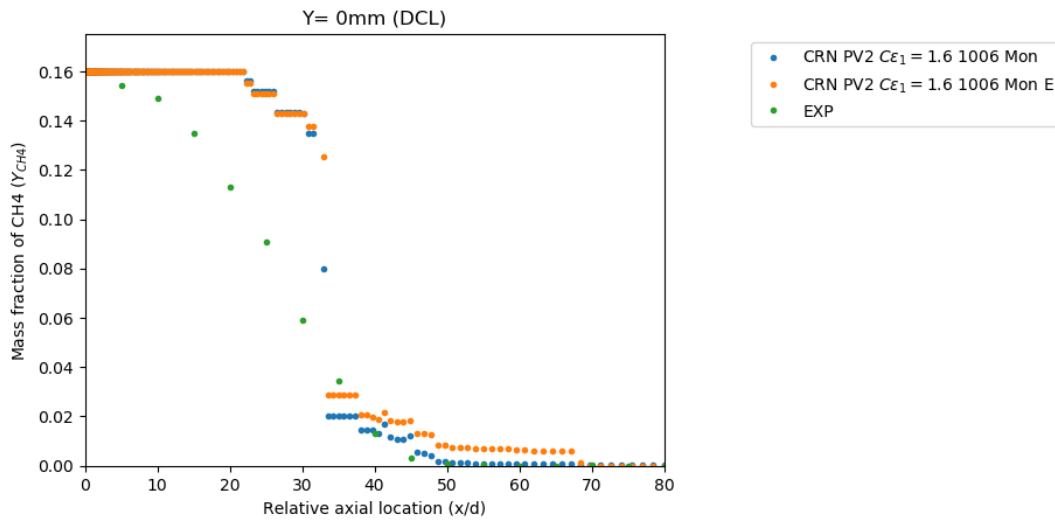


Figure 4.52: Experimental (\bullet) and CFD-CRN predicted profiles of **Mass fraction of CH_4** at the centreline **DCL** ($r/d_{jet} = 0$) for CRNs with **1035** PSRs in the Monaghan clustering **without** (\bullet) and **with updating temperature** (\bullet).

The major species are significantly less influenced by the updated temperature. Figure 4.53 and 4.54 are cross sectional contours of the mass fraction of H_2O at $x/d=45$ and 75. It can be seen that the respective CRN wedges are virtually identical.

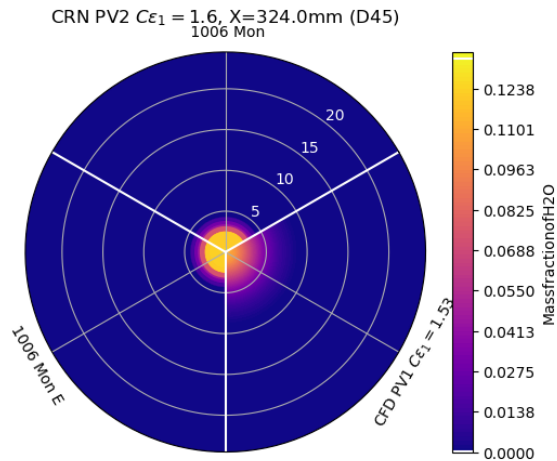


Figure 4.53: CFD PV2 $C\epsilon_1 = 1.6$ (CFD) and CFD-CRN predicted cross-sectional contours of **Mass fraction of H2O** at axial location **D45** ($x/d_{jet} = 45$) for CRNs with **1006** PSRs in the Monaghan clustering **without** (1006 Mon) and **with updating temperature** (1006 Mon E).

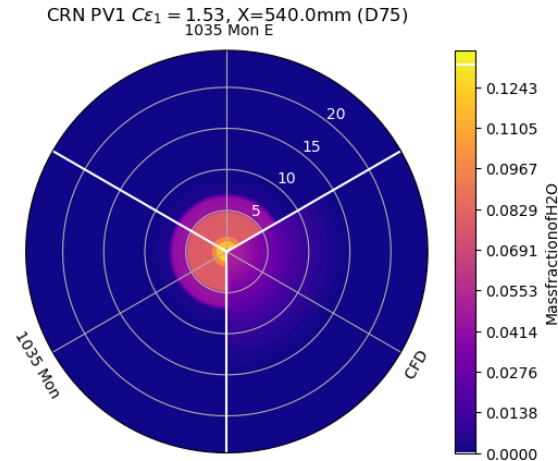


Figure 4.54: CFD PV2 $C\epsilon_1 = 1.6$ (CFD) and CFD-CRN predicted cross-sectional contours of **Mass fraction of H2O** at axial location **D75** ($x/d_{jet} = 75$) for CRNs with **1006** PSRs in the Monaghan clustering **without** (1006 Mon) and **with updating temperature** (1006 Mon E).

VERISSIMO ET AL. TEST CASE

When AGNES solved the CRN using the energy equation for the Verissimo et al. test case, the temperature was overpredicted, which was also seen in the Sandia Flame D test case. Compared to the contour without temperature updating in Figure 4.55, the temperature contour in Figure 4.56 shows that the maximum temperature region has moved slightly downstream, the temperature in the downstream region has increased overall and the temperature range now also extends to a higher temperature.

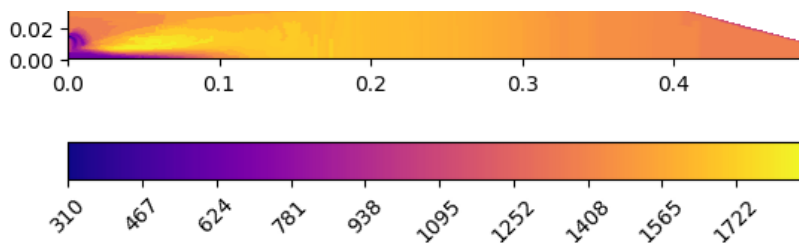


Figure 4.55: CFD-CRN predicted parallel contour of **Static Temperature** [K] for a CRN with **3137** PSRs in the **constant tolerance clustering**.

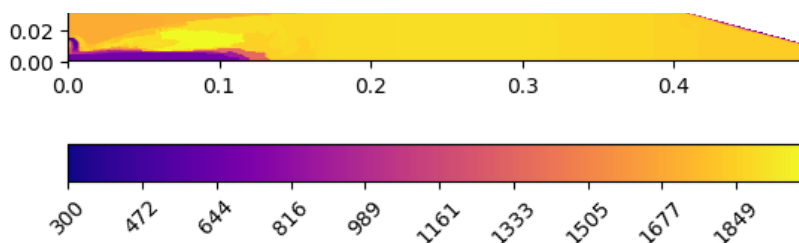


Figure 4.56: CFD-CRN predicted parallel contour of **Static Temperature** [K] for a CRN with **3137** PSRs in the **constant tolerance clustering** whilst **updating the temperature**.

Figure 4.57 shows the updated temperature contour when the Monaghan clustering was applied. It can be seen, that the downstream region also increased in temperature and the maximum temper-

ature increased more compared to Figure 4.56. The maximum temperature region, however, seems to have moved upstream instead of downstream. This has to do with the L-shape of some clusters in this region that extend upstream.

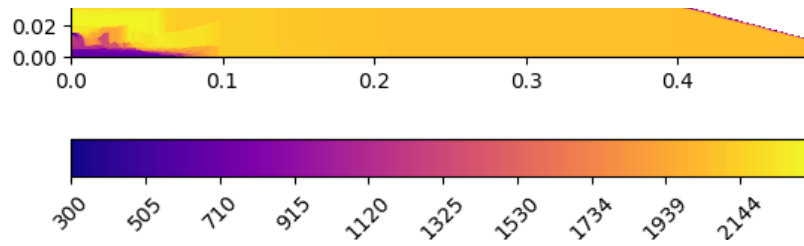


Figure 4.57: CFD-CRN predicted parallel contour of **Static Temperature** [K] for a CRN with **3210 PSRs** in the **Monaghan clustering** whilst **updating the temperature**.

The increase in predicted temperature, just like in the Sandia Flame D, causes an increase in the mass fractions predicted for CO and NOx. The changes in prediction of these minor species close to the outlet are shown in Figure 4.58 and 4.59. The prediction of the mass fraction of CO is still relatively close to the experimental data in Figure 4.58 and the same is the case for the results using the Monaghan clustering.

In Figure 4.59, the predicted mass fraction of NOx can be compared between the two clustering methods. It can be seen, that both methods overpredict when the energy equation is used, but the overprediction of the Monaghan clustered case is much larger. This can be attributed to the larger temperature overprediction and the higher temperatures upstream due to the cluster shapes.

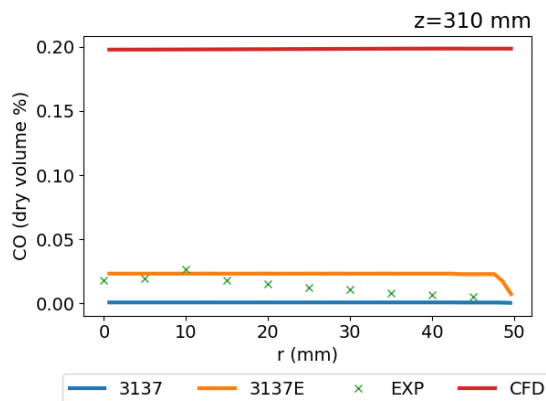


Figure 4.58: Experimental (x), CFD (red line) and CFD-CRN predicted profiles of **Mass fraction of CO** in the radial direction at axial location **310** ($z = 310\text{mm}$) for CRNs with **3137 PSRs** in the **constant tolerance clustering without** (blue line) and **with updating the temperature** (orange line).

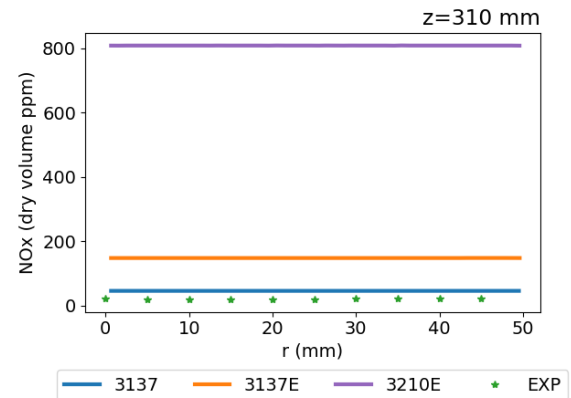


Figure 4.59: Experimental (x) and CFD-CRN predicted profiles of **Mass fraction of NOx** in the radial direction at axial location **310** ($z = 310\text{mm}$) for CRNs with **3137 PSRs** in the **constant tolerance clustering without** (blue line) and **with updating the temperature** (orange line), and **3210 PSRs** in **Monaghan clustering with updating the temperature** (purple line).

The major species, such as CO₂ and O₂, are much less affected by the updated temperature compared to the minor species. Figure 4.60 and 4.61 show that the curves are not identical, but generally close together.

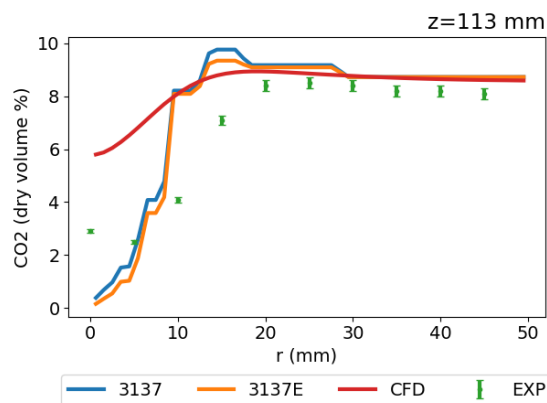


Figure 4.60: Experimental (●), CFD (●) and CFD-CRN predicted profiles of **Mass fraction of CO₂** in the radial direction at axial location **113** ($z = 113\text{mm}$) for CRNs with **3137** PSRs in the **constant tolerance clustering without** (●) and **with updating the temperature** (●).

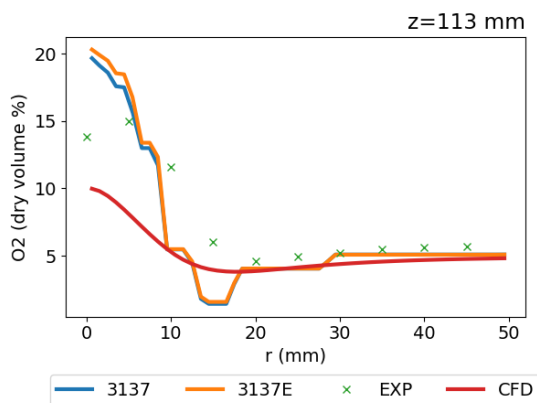


Figure 4.61: Experimental (●), CFD (●) and CFD-CRN predicted profiles of **Mass fraction of O₂** in the radial direction at axial location **113** ($z = 113\text{mm}$) for CRNs with **3137** PSRs in the **constant tolerance clustering without** (●) and **with updating the temperature** (●).

4.6. CRN SOLVING TIME

Solution accuracy and time are often balanced to determine the most suitable solution method. The solving time of AGNES is mostly dependent on size of the CRN. Furthermore, solving the energy equation increases the non-linearity and size of the system of equations, which increases the solution time. The clustering method and CFD input had a small effects on the solving time. The clustering method and CFD input can affect the convergence with averaging as a result of the reactor distribution. The clustering method can also indirectly have an effect on the solving time, because it influences the minimal required size of the CRN for desired accuracy and convergence.

Table 4.3 lists the solution time in seconds for each combination of CRN size, clustering method, energy equation setting and CFD input. For the Sandia Flame D, the solving time ranged between 12.2 hours and 5.5 minutes. The solving time for the Verissimo et al. test case ranged between just below 2 hours and almost 45 hours. The difference in range for the two test cases is in part due to the size of the reactor network, because the shortest solving time in the Sandia Flame D has only 249 reactors whilst the Verissimo et al. test case has 1008 reactors. However, when comparing CRNs of similar size with the same clustering method and use of the energy equation, the Verissimo et al. test case still has a solving time that is more than twice as long compared to the Sandia Flame D. This difference can potentially be attributed to the effect of 3D versus 2D on the CRN.

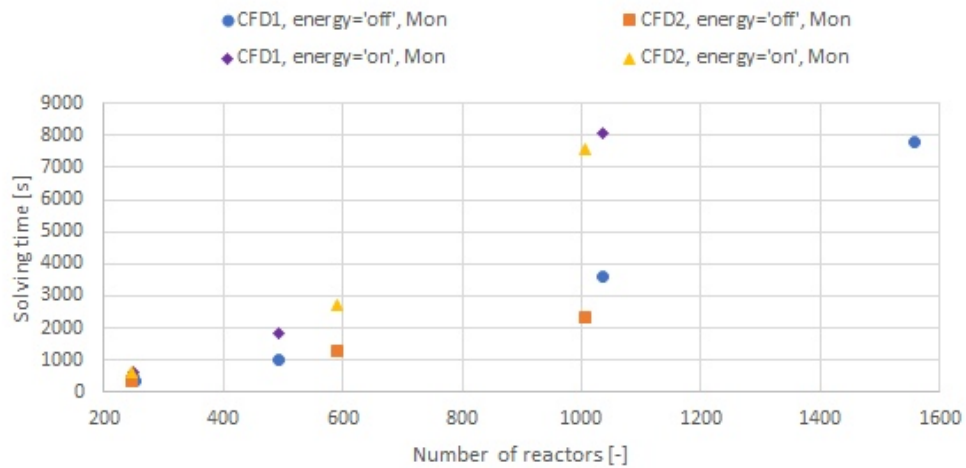
Figure 4.62 is a plot of the solving time versus the number of reactors for the Sandia Flame D. The trend with increasing reactor number is not linear and the solving time increases more for increasing numbers of reactors.

The non-linearity of the solving time corresponds with the fact that the CRN is a system of equation that grows quadratically with each additional reactor. When the same plot is generated using the number of reactors squared, the trends are all linear except for the series with 'CFD2, energy='off', Mon', due to a relatively high solving time at 590 reactors, which seems to be a small anomaly.

For the run cases that also solve the energy equation the trends are steeper with increasing number of reactors. At around a 1000 PSRs the solving time of the run cases that solve the energy equation is already more than double the amount for the run cases that do not solve it.

Table 4.3: CRN solving times

Number of reactors	Clustering method	Energy equation	CFD	Solving time [s]
249	Mon	off	PV1 $C\epsilon_1 = 1.53$	467.902359
249	Mon, $\Delta f = 0.02$	off	PV1 $C\epsilon_1 = 1.53$	340.515189
252	Mon, $\Delta T = 16K$	off	PV1 $C\epsilon_1 = 1.53$	331.872032
248	Mon, $\Delta T = 75K$	off	PV1 $C\epsilon_1 = 1.53$	346.354404
1559	Mon	off	PV1 $C\epsilon_1 = 1.53$	7796.934096
493	Mon	off	PV1 $C\epsilon_1 = 1.53$	1032.167115
1035	Mon	off	PV1 $C\epsilon_1 = 1.53$	3625.837703
247	Mon	off	PV2 $C\epsilon_1 = 1.6$	362.202244
590	Mon	off	PV2 $C\epsilon_1 = 1.6$	1265.588677
1006	Mon	off	PV2 $C\epsilon_1 = 1.6$	2340.212984
1035	Mon	on	PV1 $C\epsilon_1 = 1.53$	8075.29223
1006	Mon	on	PV2 $C\epsilon_1 = 1.6$	7575.321116
249	Mon	on	PV1 $C\epsilon_1 = 1.53$	641.716191
247	Mon	on	PV2 $C\epsilon_1 = 1.6$	642.497808
493	Mon	on	PV1 $C\epsilon_1 = 1.53$	1851.071156
590	Mon	on	PV2 $C\epsilon_1 = 1.6$	2700.98292
5496	Mon (tol 6)	off	PV1 $C\epsilon_1 = 1.53$	43949.326
1581	Ts, X, f (tol 3)	off	PV1 $C\epsilon_1 = 1.53$	7444.954951
249	Scaling	off	PV1 $C\epsilon_1 = 1.53$	369.132978
3137	Con	off	Run 2	17671.944023
3137	Con	on	Run 2	64042.862452
1008	Mon	off	Run 2	6571.910287
1008	Mon	on	Run 2	17215.924117
3210	Mon	off	Run 2	32478.349307
3210	Mon	on	Run 2	161350.067126

Figure 4.62: CRN solving time. (CFD1: PV1 $C\epsilon_1 = 1.53$, CFD2: PV2 $C\epsilon_1 = 1.6$)

5. CONCLUSION

Based on the results described in Chapter 4, conclusions can be drawn regarding the research topic of this thesis. These conclusions are detailed in Section 5.1. Furthermore, Section 5.2 describes some additional conclusions regarding the method and test case.

5.1. RESEARCH CONCLUSIONS

The main objective of this research is the progression of knowledge in the field of the promising hybrid CFD-CRN method. CFD-CRN is a method used to predict emissions produced by combustion systems. This particular approach splits up the emission prediction problem by first computing the flow field using CFD with reduced chemical kinetics and then solving for detailed chemistry via a chemical reactor network (CRN) that is constructed with the results from the CFD computation.

In literature, it was found that most researchers have assumed that the temperature determined by CFD can be kept fixed. This assumption is based on the reasoning that the reduced chemistry including the major species is sufficiently accurate, because the concentrations of minor species computed with the CRN are present in too small quantities to significantly influence the temperature with their low heat release. There was a lack of scientific results supporting this common assumption and it can be argued that this assumption might not be valid for the prediction of minor species, because the formation rates are very sensitive to minor temperature changes.

The following research question was opted with the goal to determine the impact of the assumption to keep the temperature fixed on the prediction of minor species and what influences this impact:

How are the results and run performance affected by applying the energy equation to recompute the temperature in a CRN for the CFD-CRN method?

It was hypothesized that applying the energy equation would increase the accuracy of the emission prediction and increase the simulation time. It was expected that the extent of this increase in both is dependent on the test case and run settings analyzed, but that it would always be present.

In this research, a computational tool developed at the Delft University of Technology, called AGNES, was adjusted to create the option of updating the temperature in the CRN with the energy equation and multiple runs were performed for different settings to determine differences between the two options to test the hypothesis.

As hypothesized, the solving time increases when the temperature is updated by solving the energy equation compared to keeping the temperature fixed at the value computed by CFD. It was also found that the relative solving time increases more with increasing number of reactors. Therefore the effect of increased solving time is more significant when considering the use of the energy equation in larger CRNs.

Solving the energy equation had a significantly larger impact on the mass fractions of minor species compared to those of major species predicted by the CRN for both test cases. This was in line with expectations, which is why the validity of the assumption was only questioned in this thesis for the minor species.

Regarding the accuracy of the predictions compared to the experimental data, it was found, that applying the energy equation to update the temperature caused an overprediction in temperature.

This temperature overprediction was in general more pronounced in the downstream region of the test domain.

This overprediction of temperature is probably caused by a lack of heat transfer modelling in the CFD-CRN solver. The only mode of heat transfer that is taken into account is convection, which is modeled by the mass flow exchange between reactors. However, conduction and radiation are both neglected, which is suspected to reduce the diffusion of heat from the flame zone, which essentially keeps it trapped in the system instead of leaving through the domain sides.

Furthermore, the highest temperature region, which is an important factor in minor species production, not only increased beyond the original and experimental values, but also moved downstream in most cases. This can be attributed to the interaction between temperature, density and mass flow. The increase in temperature was found to cause a decrease in density. Taking into account the mass flows and volume of reactors that are kept constant, the relative mass exchange has to increase, which leads to a downstream shift.

The increase in temperature in certain regions where the minor species were underpredicted could lead to an increase in accuracy compared to the experimental results. Unfortunately, in general, the overprediction in temperature led to a significant overprediction in CO and NOx.

In conclusion, the application of the energy equation does have a significant effect, but it is not recommended to apply the energy equation to update the temperature in the current set up, because it causes overprediction of important minor species mass fractions and increases solving times. If the heat transfer is accurately modeled in AGNES, this recommendation might change.

5.2. METHOD AND TEST CASE CONCLUDING REMARKS

During the execution of this research there were a few unexpected developments, that do not directly answer part of the research question, but deserve to be mentioned as relevant conclusions to progress the field of CFD-CRN, which is the main objective of this research.

The first conclusion is related to the relatively uniform bulk flow moving upward in the Sandia Flames. Due to this set up, the advective mass flow does not contribute much to radial mixing of species. Therefore in this case, which doesn't include any recirculation, turbulent diffusion is a significant part in mixing of species in the radial direction and was modeled to improve the accuracy. Fortunately, this was not found to be necessary for the Verissimo et al. test case, since it has more radial mixing due to the recirculation.

The second concluding point concerns the clustering method. In the pre-research version of AGNES multiple clustering criteria could be selected and combined with a global tolerance. These criteria were used to determine which cells could be grouped. Using this method on the Sandia Flame D grid convergence was not reached within a reasonable solving time.

It was found that using zones with discrete variations of the clustering criteria and tolerances according to the method used by Monaghan et al. [3] for the Sandia Flame D, grid convergence could be improved significantly. This was attributed to the ability to control the resolution and increase reactor density in the necessary regions. It was found, that the same clustering method worked somewhat for the Verissimo et al. test case and although it decreased curve fitting downstream, resulted in similar or improved accuracy of species prediction when the temperature was not updated.

The zoning method can be seen as a discrete scaling of the tolerances in the domain. The results of the zoned domain can be approximated by continuously scaled tolerances. Further research into this type of scaling and standardization for combustion systems has great potential.

6. RECOMMENDATIONS

In this chapter, recommendations are made based on the research and programming performed through this thesis. These recommendations include recommended improvements of AGNES in Section 6.1, recommendations for users of AGNES in Section 6.2 and suggestions for future research with AGNES in Section 6.3.

6.1. RECOMMENDED IMPROVEMENTS OF AGNES

In Section 1.3, five recommendations were made for improvements of the pre-research version of AGNES. Two of these recommendations were implemented in the current version of AGNES. This leaves the following three recommendations:

Turbulence: Currently temperature fluctuations due to turbulence present in the PSR is not modeled in AGNES [20]. However, the effect of turbulence on temperature fluctuations was found to be important by Cuoci et al. (2013), who saw a significant improvement in the results when temperature fluctuations due to turbulence were accounted for in the model [12]. It is recommended to further study the effect that the modeling of these temperatures fluctuations has on the accuracy of the emission predictions for different test cases to determine when modeling these fluctuations is useful.

Liquid Fuels: AGNES has only been used for gaseous fuels [20]. To allow research of test cases with liquid fuels, like gasoline and kerosene, some adjustments will have to be made. To ensure proper modeling of the liquid fuel spray a simulation for spray combustion of ANSYS Fluent can be used [20]. This would require some changes to the processing of the CFD results to ensure the simulation results are read correctly. For the chemistry modeling it is possible to neglect the liquid phase chemistry and just consider the gas phase. This method is based on the assumption that CFD correctly predicts droplet evaporation of the liquid fuel and the associated changes in heat release and temperature [20]. This method would require the gases formed by the droplet evaporation to enter the respective reactor as boundary inlet mass flow by including it in the source term [20].

An expected issue for running simulations for liquid fuels is the increased computational power and time associated with the larger kinetic mechanism required to model liquid fuels, like gasoline and kerosene [20]. Therefore it might be useful to also focus on the computational efficiency of AGNES to reduce the computational time for dealing with liquid fuels.

Complex geometries: AGNES was not tried on complex geometries yet [20]. The program has some hard coded zone IDs incorporated that have to be adjusted for the respective simulation [20]. Furthermore, AGNES is currently only able to handle one Fluent fluid zone [20]. In the future, it might be useful to enable multiple zones to allow the modeling of combustion systems with more complex geometries.

In addition to the continued recommendations listed above, two recommended implementation were identified during this research. AGNES is meant to be a generic tool that can be applied to virtually any test case. However, it was found that the pre-research clustering method, that uses one tolerance value for the entire domain, results in too high resolution in less relevant regions, too low resolution in essential regions or a combination of both. In this research, this problem was remedied by using the zoning as proposed by Monaghan et al. [3]:

Zoned/Scaled clustering: To improve AGNES and make sure it can be used in a more generic way, the principle of zoning and/or scaling tolerances should be explored further and a more generic/s-standardized zoning/scaling function should be added to the clustering method of AGNES.

Diffusion proved to be a significant issue for the Sandia Flame D test case, due to the predominantly axial bulkflow and lack of recirculation. Therefore a turbulent diffusion model was added. However, although the model improve the results somewhat, the results clearly still show a lack of diffusion. This lack could be caused by size and shape of the clusters combined with the use of PSRs in the CRN:

Plug Flow Reactors: To decrease the effect of the axial elongation of clusters, on the species diffusion in axial bulk flows, the option of using PFRs in the CRN instead of PSRs should be added to AGNES.

6.2. USER RECOMMENDATIONS FOR AGNES

Future users of AGNES are advised to consult the readme.txt file when starting a project with AGNES. EmissionsCalculator_Batch.py is the main run file of AGNES. To perform a simulation on a selected test case the non-binary case and data file of ANSYS Fluent have to be included in the same folder as EmissionsCalculator_Batch.py. Test case specific inputs have to be supplied to the Main() function in EmissionsCalculator_Batch.py as well as the desired clustering criteria and number of reactors. The plotting functions present are specific to the Sandia Flame D and Verissimo et al. test case and will have to be adjusted for other test cases.

When generating a CRN from CFD results the correct choice of clustering criteria and the number of reactors is crucial. It is recommended to chose clustering criteria that directly influence the emission production. This is the main reason why temperature and mixture fraction are often used, in literature, as a clustering criteria. However, most researchers have used manually applied zones to further control the reactor distribution. In case of AGNES, it is advised to look at the distribution of reactors and their shape and size to determine if other criteria or zones need to be used/added to ensure the desired accuracy.

6.3. SUGGESTED RESEARCH WITH AGNES

It is suggested to attempt modeling heat transfer in the form of conduction and radiation in AGNES and rerun simulations for the test cases described to determine, whether that improves the accuracy of the temperature prediction using the energy equation. If there is significant improvement, the use of the energy equation could prove to be beneficial for future test cases.

Furthermore, it was recommended in Section 6.1 to develop a more standardized way of applying tolerance zones or tolerance scaling. To start this development, it is recommended to perform an optimization/sensitivity study on the tolerance scaling method attempted in this research with the Sandia Flame D. Once the best method of zoning/scaling is found, the same method can be applied on similar test case, e.g. the other Sandia Flames, to develop a standardized automatic method of clustering for piloted flames.

CFD-CRN is a promising method from fast and accurate emission prediction. To further mature the method more research has to be performed on several more test cases. Preferably, these test cases include combustion from different regimes, such as flameless combustion, and different types of flow phenomena, like recirculation. In this way, the best approach for setting up the CFD-CRN method and its effectiveness can be determined for the different regimes and flow phenomena.

AGNES can be used by researchers at the Delft University of Technology to perform research on the CFD-CRN method. Once more is known about simulating certain combustion systems, AGNES could be used for emission prediction of combustion system concepts and set-ups in the lab.

BIBLIOGRAPHY

- [1] Sandia National Laboratories, *Sandia / TUD piloted CH₄ / air jet flames*, [http://www.sandia.gov / TNF / DataArch / FlameD.html](http://www.sandia.gov/TNF/DataArch/FlameD.html) (2003).
- [2] A. Verissimo, A. Rocha, and M. Costa, *Operational, combustion, and emission characteristics of a small-scale combustor*, *Energy & Fuels* **25**, 2469 (2011).
- [3] R. Monaghan *et al.*, *Detailed multi-dimensional study of pollutant formation in a methane diffusion flame*, *Energy & Fuels* **26** (2012).
- [4] J. Warnatz *et al.*, *Combustion Physical and Chemical Fundamentals, Modeling and Simulation, Experiments, Pollutant Formation*, 4th ed. (Springer, Berlin Heidelberg New York, 2006).
- [5] D. Winterbone and A. Turan, *Advanced Thermodynamics for Engineers*, 2nd ed. (Butterworth-Heinemann, Boston, 2015).
- [6] A. Rao and Y. Levy, *A new combustion methodology for low emission gas turbine engines*, Proceedings of 8th international symposium on high temperature air combustion and gasification **Poland** (2010).
- [7] R. Barlow and J. Frank, *Piloted CH₄/air flames C, D, E, and F (release 2.1)*, [https://www.sandia.gov / TNF / DataArch / FlameD / SandiaPilotDoc21.pdf](https://www.sandia.gov/TNF/DataArch/FlameD/SandiaPilotDoc21.pdf) (2007).
- [8] G. Ren *et al.*, *Review of electrical energy storage system for vehicular applications*, *Renewable and Sustainable Energy Reviews* **41** (2015).
- [9] R. Rezvani, *A Conceptual Methodology for the Prediction of Engine Emissions*, PhD thesis, Georgia Institute of Technology (2010).
- [10] S. Yousefian *et al.*, *Review of hybrid emissions prediction tools and uncertainty quantification methods for gas turbine combustion systems*, Turbomachinery Technical Conference and Exposition **2017** (2017).
- [11] T. Faravelli *et al.*, *A new procedure for predicting NO_x emissions from furnaces*, *Computers & Chemical Engineering* **25** (2001).
- [12] A. Cuoci *et al.*, *Numerical modeling of NO_x formation in turbulent flames using a kinetic post-processing technique*, *Energy & Fuels* **27** (2013).
- [13] D. Benedetto *et al.*, *NO_x emission prediction from 3-D complete modelling to reactor network analysis*, *Combustion Science and Technology* **153** (2000).
- [14] F. Lipfert, *Correlation of gas turbine emission data*, ASME 1972 International Gas Turbine and Fluids Engineering Conference and Products Show **1975** (1972).
- [15] W. Hung, *An experimentally verified NO_x emission model for gas turbine combustors*, ASME 1972 International Gas Turbine and Fluids Engineering Conference and Products Show **1975** (1975).
- [16] G. Touchton, *An experimentally verified NO_x prediction algorithm incorporating the effects of steam injection*, *Journal of Engineering for Gas Turbines and Power-Transactions of the ASME* **106** (1984).

- [17] E. Fuller and C. Smith, *Integrated CFD modeling of gas turbine combustors*, AIAA / SAE / ASME / ASEE 29th Joint Propulsion Conference and Exhibit **1993** (1993).
- [18] M. Lai, *CFD analysis of liquid spray combustion in a gas turbine combustor*, ASME 1997 International Gas Turbine and Aeroengine Congress and Exhibition **2: Coal, Biomass and Alternative Fuels; Combustion and Fuels; Oil and Gas** (1997).
- [19] D. Crocker *et al.*, *CFD modeling of a gas turbine combustor from compressor exit to turbine inlet*, Journal of Engineering for Gas Turbines and Power **121** (1999).
- [20] R. Sampat, *Automatic generation of Chemical Reactor Networks for Combustion Simulations*, Msc thesis, TU Delft (2018).
- [21] A. Stagni *et al.*, *A fully coupled, parallel approach for the post-processing of CFD data through reactor network analysis*, Computers and Chemical Engineering **60** (2013).
- [22] K. Ehrhardt *et al.*, *Modeling of NO_x reburning in a pilot scale furnace using detailed reaction kinetics*, Combustion Science and Technology **131** (1998).
- [23] M. Falcitelli *et al.*, *An algorithm for extracting chemical reactor network models from CFD simulation of industrial combustion systems*, Computers & Chemical Engineering **174** (2002).
- [24] M. Mancini *et al.*, *On mathematical modelling of flameless combustion*, Combustion and Flame **150** (2007).
- [25] M. Skjoth-Rasmussen *et al.*, *Post-processing of detailed chemical kinetic mechanisms onto CFD simulations*, Computers & Chemical Engineering **28** (2004).
- [26] A. Frassoldati *et al.*, *Determination of NO_x emissions from strong swirling confined flames with an integrated CFD-based procedure*, Chemical Engineering Science **60** (2005).
- [27] I. Novosselov *et al.*, *Chemical reactor network application to emissions prediction for industrial gas turbine*, ASME Turbo Expo 2006: Power for Land, Sea, and Air **1: Combustion and Fuels, Education** (2006).
- [28] A. Cuoci *et al.*, *The ignition, combustion and flame structure of carbon monoxide/hydrogen mixtures. note 2: Fluid dynamics and kinetic aspects of syngas combustion*, International journal of hydrogen energy **32** (2007).
- [29] V. Fichet *et al.*, *A reactor network model for predicting NO_x emissions in gas turbines*, Fuel **89** (2010).
- [30] R. Monaghan *et al.*, *Detailed emissions prediction for a turbulent swirling nonpremixed flame*, Energy & Fuels **28** (2013).
- [31] T. Nilsson, *Development of a Simulation Methodology for Gas Turbine Combustion*, Msc thesis, Lund University (2014).
- [32] I. Stanton and G. Kliot, *Streaming graph partitioning for large distributed graphs*, ACM SIGKDD Conference **18** (2012).
- [33] S. Liviu-Constantin and M. Daniela-Elena, *Simplified mechanisms used to estimate the NO_x emission of diesel engine*, Proceedings of the 2nd International Conference on Manufacturing Engineering, Quality and Production Systems **Romania**, 61 (2010).

- [34] A. R. A.A.V. Perpignan and D. Roekaerts, *Flameless combustion and its potential towards gas turbines*, Progress in Energy and Combustion Science **69**, 28 (2018).
- [35] A. Cavaliere and M. D. Joannon, *Mild combustion*, Progress in Energy and Combustion Science **30**, 329 (2004).
- [36] A. Boguslawski and A. Tyliczszak, *Sandia flame D*, http://qnet-ercoftac.cfms.org.uk/w/index.php/Abstr:Sandia_Flame_D (2011).
- [37] A. Habibi *et al.*, *Turbulence radiation interaction in Reynolds-averaged Navier-Stokes simulations of nonpremixed piloted turbulent laboratory-scale flames*, Combustion and Flame **151**, 303 (2007).
- [38] B. Merci *et al.*, *Application of a new cubic turbulence model to piloted and bluff-body diffusion flames*, Combustion and Flame **126**, 1533 (2001).
- [39] A. Perpignan, R. Sampat, and A. Rao, *Modelling pollutant emissions of flameless combustion with a joint cfd and chemical reactor network approach*, (2019), [Accepted, doi: 10.3389/fmech.2019.00063].
- [40] J. van Oijen and L. de Goeij, *Modelling of premixed laminar flames using flamelet-generated manifolds*, Combustion Science and Technology **161**, 113 (2000).
- [41] Lawrence Livermore National Laboratory, *Sundials: Suite of Nonlinear and Differential/Algebraic equation Solvers*, <https://computation.llnl.gov/projects/sundials> (2018).
- [42] SciPy community, *scipy.integrate.bdf()*, <https://docs.scipy.org/doc/scipy/reference/generated/scipy.integrate.BDF.html> (2019).
- [43] A. Perpignan *et al.*, *Emission modeling of an interturbine burner based on flameless combustion*, Energy Fuels **32**, 822 (2018).

A. CFD SET-UP

The exact CFD set-up of both test cases is described below:

SANDIA FLAME D

MESH:

- Dimension: 2D
- Cell shape: Hexahedral
- Spacing: Increasing with distance from origin
- Number of cells: 24278

SOLVER:

- Type: Pressure-Based
- Velocity Formulation: Absolute
- Time: Steady
- 2D Space: Axisymmetric

VISCOUS MODEL:

- Model: Reynolds Stress Model
- Submodel: Linear Pressure-Strain
- Near-Wall Treatment: Standard Wall Functions

- Model constants:

C_μ	$C_{\epsilon,1}$	$C_{\epsilon,2}$	C_1	C_2	C'_1	C'_2	TKE Pr	TDR Pr	Energy Pr	Wall Pr	PDF Sc
0.09	1.53*	1.92	1.8	0.6	0.5	0.3	1	1.3	0.85	0.85	0.85

RADIATION MODEL:

- Model: Discrete Ordinates
- Iteration Parameters: 1 iteration per 10 energy iterations

- Angular Discretization:

θ Div.	ϕ Div.	θ px	ϕ px
5	5	3	3

*both 1.53 and 1.6 were selected for this parameter based on result agreement with experimental data.

SPECIES MODEL:

- Turbulent Chemistry Interaction: Flamelet Generated Manifold
- Operating Pressure: 101325
- Flamelets: Non-premixed flamelets
- Chemical kinetic reaction mechanism: GRI-3.0
- Post-processing model: NOx
- Progress Variable: CO₂, CO[†]

The progress variable (PV) is computed with Equation (A.1), which uses the sums of mass fractions associated with species considered for the progress variables (Y_{s_i}). It relates the equilibrium mass fractions to the current disregarding the mass fraction already present in the unburnt mixture [43].

$$PV = \frac{\sum_{i=1}^n (Y_{s_i} - Y_{s_i}^u)}{\sum_{i=1}^n (Y_{s_i}^{eq} - Y_{s_i}^u)} \quad (\text{A.1})$$

INLET CONDITIONS:

- Type: Velocity
- Jet: Mean Mixture Fraction = 1, Progress Variable = 0
- Pilot: Mean Mixture Fraction = 0.268, Progress Variable = 1
- Co-flow: Mean Mixture Fraction = 0, Progress Variable = 0

SOLUTION METHODS:

- Pressure Velocity Coupling: SIMPLE
- Spatial Discretization Gradient: Green-Gauss Cell Based
- Spatial Discretization: Second Order Upwind

VERISSIMO ET AL. BURNER**MESH:**

- Dimension: 3D (45° cut-out)
- Cell shape: Hexahedron (trapezoidal)
- Spacing: Increasing with distance from origin
- Number of cells: 2310062

SOLVER:

- Type: Pressure-Based
- Velocity Formulation: Absolute
- Time: Steady

[†]In combination with $C_{c,1} = 1.6$, H₂O and H₂ were added to the usual progress variable.

VISCOUS MODEL:

- Model: k- ϵ
- Submodel: Standard
- Near-Wall Treatment: Standard Wall Functions

- Model constants:

C_μ	$C_{1,\epsilon}$	$C_{2,\epsilon}$	TKE Pr	TDR Pr	Energy Pr	Wall Pr	PDF Sc
0.09	1.44	1.92	1	1.3	0.85	0.85	0.85

RADIATION MODEL:

- Model: Discrete Ordinates
- Iteration Parameters: 1 iteration per 10 energy iterations

- Angular Discretization:

θ Div.	ϕ Div.	θ px	ϕ px
3	3	2	2

SPECIES MODEL:

- Turbulent Chemistry Interaction: Flamelet Generated Manifold
- Operating Pressure: 101325
- Flamelets: Non-premixed flamelets
- Chemical kinetic reaction mechanism: GRI-3.0
- Post-processing model: NOx
- Progress Variable: CO₂, CO

SOLUTION METHODS:

- Pressure Velocity Coupling: SIMPLE
- Spatial Discretization Gradient: Green-Gauss Cell Based
- Spatial Discretization: Second Order Upwind

B. CRN SET-UP

The exact CRN set-up of both test cases is described below:

SANDIA FLAME D

CFD INPUT:

- Inlet:
Air (O₂: 0.23, N₂: 0.77 | T[K]: 291)
Fuel (CH₄: 0.16, O₂: 0.19, N₂: 0.65 | T[K]: 294)
Pilot (O₂: 0.059, N₂: 0.735, H₂O: 0.091, CO₂: 0.111, OH: 0.001, NO: 0.003 | T[K]: 1880)
- CFD:
CFD PV1 (CO₂, CO) C ϵ_1 = 1.53
CFD PV2 (CO₂, CO, H₂O, OH) C ϵ_1 = 1.6

CLUSTERING:

- Criteria: Static Temperature (T), X-Coordinate (x), Mean Mixture Fraction (f)
- Reactor numbers: 249, 493, 1035 | 247, 590, 1006
- Reactor zoning [3]:

	zone limits	reactor criteria limits
	$0 \leq f \leq 0.01$	$\Delta x = 0.2\text{m}$
	$0.01 < f \leq 0.1$	$\Delta T = 100\text{K}$
	$0.1 < f \leq 0.9, T \leq 1800\text{K}$	$\Delta T = 100\text{K}$
	$0.1 < f \leq 0.9, 1800\text{K} < T \leq 2000\text{K}$	$\Delta T = 50\text{K}$
	$0.1 < f \leq 0.9, 2000\text{K} < T$	$\Delta T = 2\text{K}$
	$0.9 < f \leq 1.0$	$\Delta f = 0.01, \Delta x = 0.01\text{m}$

SPECIES MODEL:

- Chemical kinetic reaction mechanism: GRI-3.0
-

VERISSIMO ET AL. BURNER

CFD INPUT:

- Inlet:
Air (O₂: 0.23, N₂: 0.77 | T[K]: 673.15)
Fuel (CH₄: 1.0 | T[K]: 300.0)
- CFD: Run 2

CLUSTERING:

- Criteria: Static Temperature (T), Mass fraction of H₂O ($Y_{\text{H}_2\text{O}}$), Mass fraction of O₂ (Y_{O_2}) and Mass fraction of CH₄ (Y_{CH_4})
| Static Temperature (T), X-Coordinate (x), Mean Mixture Fraction (f)
- Reactor numbers: 3137 | 1008, 3210
- Clustering method: tolerance 0.05 [20] | Monaghan [3]

SPECIES MODEL:

- Chemical kinetic reaction mechanism: GRI-3.0

C. CHANGELOG AGNES

Changelog

All notable changes to this project will be documented in this file.

The format is based on [Keep a Changelog](<https://keepachangelog.com/en/1.0.0/>),

and this project adheres to [Semantic Versioning](<https://semver.org/spec/v2.0.0.html>).

[Unreleased]

Added

- *energy='on'* Temperature terms to 'Js' and 'Jw_add' in '
↳ ReactorGen_min_internalmfc_outletvalve_newton_odeint.Jacobian_sparse'
- *energy='on'* Temperature terms to 'Jw' in '
↳ ReactorGen_min_internalmfc_outletvalve_newton_odeint.source_analytic'
- *energy='on'* Temperature terms to 'Cw' and 'RatesofProduction' in '
↳ ReactorGen_min_internalmfc_outletvalve_newton_odeint.function'
- *energy='on'* Temperature terms to 'fvect' in '
↳ ReactorGen_min_internalmfc_outletvalve_newton_odeint.Gen'
- Diction with zones and tolerances, called 'avg_dict', (see in code comment
↳ for further details) in 'EmissionsCalculator_Batch.py'
- Copied 'BFS_pchanged' function as 'BFS_pchanged_monaghan' with the option
↳ of adding zones and zone specific tolerances
- Function checking the zone of graph data called 'check_zone' in '
↳ BFS_pchanged_monaghan'
- Included dictionary with zones and tolerances in 'EmissionCalculator_Batch'

Changed

- *energy='on'* Model heat flux at the cantera walls using constant heat
↳ transfer coefficient 'U' instead of constant heat flux 'Q' in '
↳ ReactorGen_min_internalmfc_outletvalve_newton_odeint.py'
- *energy='on'* Increase 'vectsize' by 1 in '
↳ ReactorGen_min_internalmfc_outletvalve_newton_odeint.py'

Removed

- Unused list in 'ReactorGen_min_internalmfc_outletvalve_newton_odeint.'
↳ function'

[1.3.0] - 2019-07-01

Added

- Added 'Turbulent Viscosity' from the standard data 'data_std' to the '
↳ header' and 'Data' files in 'datfilepy.py'
- *2D cases* *case specific* appended surface area of respective faces

- ↳ between cells to the 'facearea.pkl' in 'casefilepy.py'
- Mass averaging function 'mass_average' that calculates the mass average of
 - ↳ a specified value of two reactors in '
 - ↳ ReactorGen_min_internalmfc_outletvalve_newton_odeint.py'
- Include turbulent diffusive mass flow rate in 'coeffmat' based on Peclet
 - ↳ number with equal opposite size for each face between reactors in '
 - ↳ ReactorGen_min_internalmfc_outletvalve_newton_odeint.Gen'
- Include 'Turbulent Viscosity' in the ParaView plots in 'SaveReactors.py'

[1.2.0] - 2019-06-24

Added

- Copied 'ReactorGen_min_internalmfc_outletvalve_newton' as '
 - ↳ ReactorGen_min_internalmfc_outletvalve_newton_odeint' to act as CRN
 - ↳ solver with global time integration
- Divergence check for entering the Newton Solver, called 'globalsolver', in
 - ↳ stead of global time integration, called 'globalsolver_odeint', in '
 - ↳ ReactorGen_min_internalmfc_outletvalve_newton_odeint.Gen'

Changed

- Replace 'ode' with 'BDF' method of 'Scipy.integrate' in
 - ↳ ReactorGen_min_internalmfc_outletvalve_newton_odeint.
 - ↳ globalsolver_odeint'
- Adjusted while-loop to accommodate for 'Scipy.integrate.BDF' method in '
 - ↳ ReactorGen_min_internalmfc_outletvalve_newton_odeint.
 - ↳ globalsolver_odeint'
- Account for 'rate_error' not output by 'Scipy.integrate.BDF' method in '
 - ↳ globalsolver_odeint' in '
 - ↳ ReactorGen_min_internalmfc_outletvalve_newton_odeint.Gen'

[1.1.0] - 2019-05-06

Added

- *case specific* Reading and plotting functions for the experimental and CFD
 - ↳ results of the Sandia Flame D (Read_Plot_all.py)
- Plotting function in 'PostProc.py' called 'axial_plot0' that generates
 - ↳ plots along a radial line at a predefined axial location.
- *case specific* Plotting function in 'PostProc.py' called 'axial_plot' that
 - ↳ generates comparative plots of the CRN, CFD and experimental results
 - ↳ of the Sandia Flame D
- Include new variables {'id_dict': [dictionary] with zone labels, ids, inlet
 - ↳ composition and temperature, 'data_num': [integer] case specific cell
 - ↳ id, 'symm_axis': [string] coordinate name of symmetry axis ('X-
 - ↳ Coordinate', etc.), 'variables': [list] variables to be plotted, '
 - ↳ axial_locations': [list] axial locations to be plotted} in '
 - ↳ EmissionsCalculator_Batch.py' to centralize changes for new cases
 - 'DataFileQuantities.txt' listing the necessary Data File Quantities to be
 - ↳ switched on in CFD to allow AGNES to function
 - *case specific* 'pmD.stat' folder with the experimental data of the Sandia

- ↳ Flame D
- *case specific* 'SFD_RSM_FGM_DO_Ceps1_153_PV1_NOx_MeshV7' folder with the
 - ↳ case relevant CFD results of the Sandia Flame D
- Include key 'Cell Volume[m³]' in diction using 'Cell Volume' from header
 - ↳ in 'PostProc.Post'
- Key 'Axial Velocity[m/s]' to diction from 'Velocity Magnitude' and 'Radial
 - ↳ Velocity' from header in 'PostProc.Post'
- *case specific* Key 'Cell Height[m]' to diction in 'PostProc.Post' for '
 - ↳ Cell Volume[m³]' and radial location
- Integral function in 'PostProc.py' called 'integral' that computes the
 - ↳ surface integral of a revolved curve
- atomic mass calculation function in 'PostProc.py' called 'mass_of' that
 - ↳ computes the mass of a certain atom in each cell
- Plotting function in 'PostProc.py' called 'integral_plot' that generates
 - ↳ plots of the surface integrated average over the axial locations
- *case specific* Plotting function in 'PostProc.py' called 'parallel_contour
 - ↳ ' that generates a contour plot parallel to the axial axis
- *case specific* Plotting function in 'PostProc.py' called 'cross_contour'
 - ↳ that generates radial contour plots of selected run cases as pie-
 - ↳ sections of the same plot

Changed

- *2D cases* Add the missing coordinate as a list of zeros in 'datfile.py' if
 - ↳ necessary
- *2D cases* Use 'Cell Volume' times 2pi 'Cell Volume' in 'datfilepy.py' if
 - ↳ necessary
- Automatically generate 'startlist' from 'id_dict' in 'CRN_Gen.py'
- Determine starting point by checking if 'start_ratio' is included in '
 - ↳ id_dict' in 'BFS_pchanged.py'
- *2D cases* Let the missing velocity direction be zero in 'BFS_pchanged.py'
 - ↳ if necessary
- Determine 'vel_dir' in 'BFS_pchanged.py' based on the predefined symmetry
 - ↳ axis 'symm_axis' in stead of a default axis
- Only proceed with generating inlet boundary cell if 'mflux' is not 0 in '
 - ↳ ReactorGen_min_internalmfc_outletvalve_newton.py' (related to issue of
 - ↳ many reactors near the wall of the inlet, causing a 0 inlet mass flux)
- Compressed boundary inlet definition and removed hard coding by using '
 - ↳ id_dict' in 'ReactorGen_min_internalmfc_outletvalve_newton.py'
- Use 'symm_axis' in stead of a default axis in 'SaveReactors.py'

Removed

- (Forgotten) commented out sections
- Unused (valued) local variables (except checks inside try-except set ups)
- Unused function parameters in all occurrences
- Unused imports

Fixed

- General PEP-8 compliance